Spring 5-15-2016

Translational Photoacoustic Tomography

Yong Zhou
Washington University in St. Louis

WASHINGTON UNIVERSITY IN ST. LOUIS

School of Engineering and Applied Science

Department of Biomedical Engineering

Dissertation Examination Committee:
Lihong V. Wang, Chair
Mark A. Anastasio
Jianmin Cui
Gregory Lanza
Baranidharan Raman
Jung-Tsung Shen

Translational Photoacoustic Tomography

by

Yong Zhou

A dissertation presented to the
Graduate School of Arts & Sciences
of Washington University in
partial fulfillment of the
requirements for the degree
of Doctor of Philosophy

May 2016
St. Louis, Missouri

Table of Contents

List of Figures

List of Tables

Acknowledgments

I gratefully thank my mentor, Dr. Lihong V. Wang, for his inspiring guidance, generous support, and constant encouragement. I also acknowledge him for helping me establish a high ethical standard in research.

I thank all my collaborators, Dr. Mark Anastasio, Dr. Lynn Cornelius, and Dr. Xiaobin Yi, for their work and my committee members for their support of my work.

I thank all the lab colleagues, especially Dr. Konstantin Maslov, for their contributions and useful suggestions to this work. I also thank Prof. James Ballard for his careful editing of this dissertation and his years of help.

Yong Zhou

Washington University in St. Louis

May 2016

Dedicated to my family.

ABSTRACT OF THE DISSERTATION

Translational Photoacoustic Tomography

by

Yong Zhou

Doctor of Philosophy in Biomedical Engineering

Washington University in St. Louis, 2016

Professor Lihong V. Wang, Chair

Combining optical excitation and ultrasonic detection, photoacoustic tomography (PAT) offers deep imaging with high resolution. With optical excitation, PAT maintains the high contrast of optical imaging. Because of the low scattering of ultrasonic waves in tissue, PAT achieves high spatial resolution at depths. Several advantages make PAT suitable for clinical application, including its scalable penetration and resolution, high optical absorption contrast, fast imaging speed, and ability to perform spectral decomposition. Based on different image reconstruction mechanisms, PAT can be further divided into two embodiments: raster-scanning-based photoacoustic microscopy (PAM) and reconstruction-algorism-based photoacoustic computed tomography (PACT). This dissertation aims to advance the direction of translational PAT, including both PAM and PACT.

In Chapter 1, I first explain the basic principles of PAM and PACT and then discuss in detail why they are suitable for translational studies. The chapter concludes with the motivation of my dissertation.

Chapter 2 introduces my translational studies in PAM. I first improved the system's lateral resolution and imaging penetration depth by applying an optical clearing technique. With glycerol as an optical clearing agent, the imaging performance of optical resolution PAM (OR-PAM) was greatly enhanced both *in vitro* and *in vivo*. Then I applied PAM in quantifying concentrations of blood substances, including red blood cells (RBCs) and bilirubin, and studied related diseases, such as RBC aggregation and jaundice. After building a model to statistically analyze photoacoustic signals for absolute measurement of red blood cell count, I developed multi-wavelength decomposition algorithms and implemented multi-wavelength PA imaging to map bilirubin concentration.

Chapter 3 describes studies of complex regional pain syndrome (CRPS) in patients with both OR-PAM and acoustic resolution PAM (AR-PAM). Blood vasculature and oxygen saturation (sO_2) were imaged in eight adult patients with CRPS. Patients' hands and cuticles were imaged both before and after stellate ganglion block (SGB) for comparison. For all patients, both vascular structure and sO_2 could be assessed by PAM. In addition, more vessels and stronger signals were observed after SGB. The results show that PAM can help diagnose and monitor CRPS.

Chapter 4 introduces my work on flow measurement both in mice and humans. It first discusses improving the flow measurement accuracy by a new technique – cross-correlation-based flowmetry. This technique is based on OR-PAM and can effectively remove the particle size induced measurement error. I demonstrated this technique both in phantom and *in vivo* experiments in mice. To achieve flow measurement in the optical diffusive regime, I further developed two methods: saline-injection-based and cuffing-based flowmetries. The saline-

injection-based method is especially pertinent to monitoring blood flow velocity in patients undergoing intravenous infusion, while the cuffing-based one is suitable for both patients and healthy people.

Chapter 5 presents my work on brain imaging, including both mouse and human brains *in vivo*. To achieve deep mouse brain imaging, I first used a ring transducer array (5 MHz center frequency) with an acoustic reflector. Blood vessels from the bottom of the mouse brain could be imaged, and many key features were detected, such as diving vessels, the superior sagittal sinus, and the posterior cerebral artery. However, the image contrast was not high due to the poor spatial resolutions of the system. To improve the image quality, I later used a linear array system with a 21 MHz center frequency. By rotating the linear array, more striking images were acquired. For the human imaging project, I successfully imaged blood vessel phantoms through an adult human skull.

Chapter 6 describes my work on melanoma imaging and depth measurement in patients. Two different systems were used in this project: a handheld AR-PAM system and a handheld linear array system. While the former is cheaper, the latter provides much faster imaging and a larger acceptance angle. With the array system, we successfully imaged melanomas in patients and achieved more accurate depth measurement than incisional biopsy in clinics.

Chapter 1 Introduction

1.1 Photoacoustic Tomography

Photoacoustic tomography (PAT), also called optoacoustic tomography, is a three-dimensional (3D) imaging modality based on the photoacoustic (PA) effect [1-4]. Although the PA effect was discovered more than a century ago by Alexander Graham Bell, it has found applications in biomedical imaging only in the last decade or so. Nowadays, PAT is one of the largest research areas in biomedical optics, and is still growing rapidly [5].

Harnessing both rich optical absorption contrast and high ultrasonic resolution, PAT is a hybrid imaging modality that can image deep tissues. While pure optical imaging modalities can also detect optical absorption by monitoring intensity variations in transmitted or reflected light, their sensitivities are usually two orders of magnitude lower than that of PAT [6]. In addition, because acoustic waves scatter much more weakly than light in biological tissues, they can propagate a greater distance than photons without losing their original propagation directions, providing PAT with high spatial resolution at depths. While pure ultrasonic imaging can also achieve high spatial resolution in deep tissues, its mechanical contrast is incapable of providing certain physiological parameters, such as the oxygen saturation of hemoglobin and the metabolic rate of oxygen [7, 8].

Based on different image reconstruction mechanisms, PAT can be further divided into two embodiments: reconstruction-algorism-based photoacoustic computed tomography (PACT) [9] and raster-scanning-based photoacoustic microscopy (PAM) [10, 11]. For PACT, the light is expanded to illuminate the whole object to be imaged. PA signals are acquired at multiple locations around the object, either by using a transducer array or by scanning a single-element transducer to simulate an array. Next, back-projecting all the PA data, similar to traditional CT or PET imaging,

generates PA images of the object. Different from reconstruction-based methods, the focused-scanning scheme of PAM usually focuses both the optical excitation and acoustic detection. If the optical focus is tighter than the acoustic focus, the technique is called optical resolution photoacoustic microscopy (OR-PAM); otherwise, it is called acoustic resolution photoacoustic microscopy (AR-PAM). In both cases, each laser pulse generates a one dimensional photoacoustic image (A-line) along the axial direction. Raster-scanning laterally and then piecing together all the A-lines provides a 3D PA image.

Several advantages make PAT suitable for clinical application. First, it can image deep: up to 7 cm deep images have been reported with a spatial resolution of a few hundred micrometers [1]. Second, it detects a rich variety of optical absorbers, both exogenous (e.g., methylene blue) and endogenous. So far, many endogenous contrasts have been imaged with high sensitivity, such as hemoglobin [12], myoglobin [13], DNA and RNA [14, 15], water [16, 17], lipid [18], cytochrome c [19], bilirubin [20], and melanin [21]. Third, similar to ultrasound imaging, PAT has scalable resolution. Thus, both fine structures (such as organelles) and global features (such as organs) can be detected with the same contrast [22-25]. Fourth, because different chemical compositions have different absorptions, features can be distinguished by multi-wavelength imaging. For example, *in vivo* human nevi and their surrounding vasculature have been successfully differentiated by PAT [25]. Fifth, because hemoglobin is confined within blood vessels, vasculature can be imaged with high contrast-to-noise ratio.

1.2 Motivation

This work aims to advance PAT to translational studies and applications. First, we want to refine the technology in order to achieve high spatial resolution and deep penetration (Chapter 2), which

can be realized by optical clearing technique. We then applied PAT to study blood vasculature diseases by measuring absolute red blood cell count and in mapping bilirubin (Chapter 2). Second, we want to study the complex regional pain syndrome (CRPS) in patients (Chapter 3). Due to a lack of proper diagnostic tools, the prognosis of CRPS is primarily based on clinical observation. The objective of this work is to evaluate PAM for assisting diagnoses and monitoring the progress and treatment outcome of CRPS. Third, we want to improve current blood flow measuring techniques and push them to humans (Chapter 4). Fourth, we want to push the direction of brain imaging both in mice and humans, because brain imaging is the key to study neuro activities (Chapter 5). Fifth, we want to achieve deep melanoma imaging and accurately measure melanoma depth in patients (Chapter 6). Melanoma depth is a key parameter in its diagnosis and treatment, but current incisional biopsy usually cannot provide accurate depth information. Because the deep penetration of PAT and strong absorption from melanin, PAT should be able to image melanoma with high contrast and accurately measure melanoma depth.

Chapter 2 Photoacoustic Microscopy of Blood Diseases

This chapter describes the technique improvement in PAM, which was achieved by using optical clearing technique. Then we applied PAM in studying two types of blood diseases: red blood cell aggregation and jaundice. Work in this chapter has been published in Optics Letters and Journal of Biomedical Optics [20, 26, 27].

2.1 Optical Clearing-aided Photoacoustic Microscopy with Enhanced Resolution and Imaging Depth in Mouse *in Vivo*

Background Photoacoustic microscopy (PAM) is a recently developed imaging modality that can provide structural [1], molecular [20], functional [28-31], and metabolic information [7]. Based on its focusing mechanism, PAM can be divided into two different implementations: acoustic-resolution PAM and optical-resolution PAM (OR-PAM). In OR-PAM, the lateral resolution is determined by the diffraction-limited optical focusing. As photons travel in tissue, the focusing capability degrades due to optical scattering. In addition, the maximum penetration depth of OR-PAM in biological tissue is mainly limited by the optical transport mean free path, affected by both absorption and scattering. Since the tissue scattering is typically an order of magnitude larger than the absorption, it is the scattering that predominantly limits the penetration depth of OR-PAM [32].

To reduce the scattering, tissue optical clearing (TOC) techniques have been widely used in many high resolution optical imaging modalities, such as laser speckle contrast imaging and optical coherence tomography. The basic mechanism of TOC is to diffuse a high-refractive-index optical clearing agent (OCA) into the tissue, which reduces the refractive index mismatch between intracellular components and extracellular fluids and thus decreases the scattering. In addition,

tissue dehydration caused by OCAs has also been used to explain TOC [33]: on one hand, it increases refractive index matching due to decreased volume fraction of free water in the interstitial fluid; on the other hand, it increases packing of scatters, which may engender spatial correlations between scatterings, both of which reduce scattering further. In this Letter, for the first time, we demonstrate that both the imaging depth and lateral resolution of OR-PAM can be enhanced by using a glycerol–water solution (88% vol./vol.), which is a commonly used OCA in TOC.

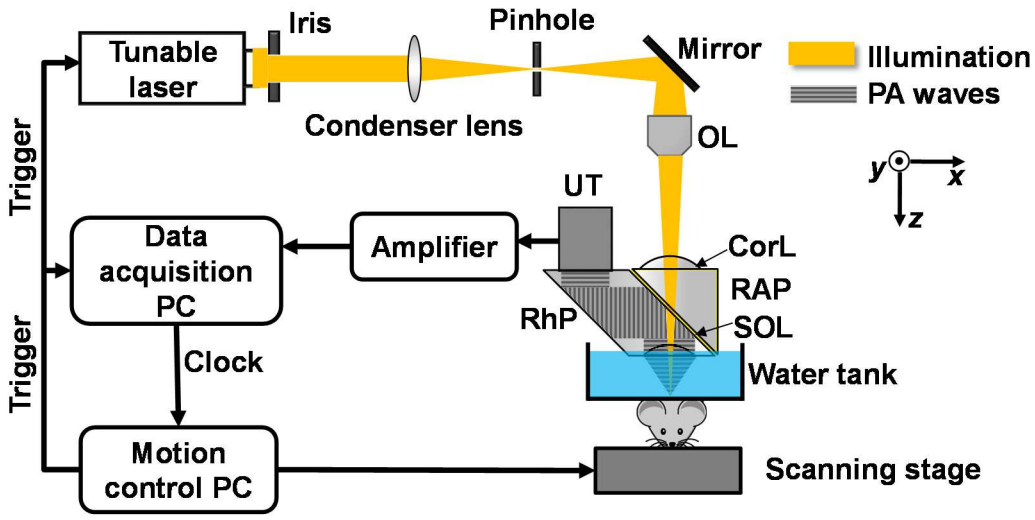

Figure 2.1 System schematic used in the optical clearing-aided optical resolution photoacoustic microscopy (OR-PAM). CorL, correction lens; OL, objective lens; RAP, right-angle prism; RhP, rhomboid prism; SOL, silicone oil layer; UT, ultrasonic transducer.

Methods We implemented this idea on a previously reported OR-PAM system (Figure 2.1). Briefly, a tunable dye laser (CBR-D, Sirah, GmbH) pumped by a Nd:YLF laser (INNOSAB, Edgewave, GmbH) was the light source. After being focused by a condenser lens, filtered by a pinhole, and reflected by a mirror, the laser beam was finally focused by an objective lens into the sample. Ultrasonic detection was achieved by a wideband ultrasonic transducer (V214-BC, Panametrics-NDT Inc.), which was placed confocally with the optical objective lens. Each laser pulse yielded a one-dimensional depth resolved PA image (A-line) by recording the time course

of PA signals. A three-dimensional (3D) image was obtained by raster scanning the sample and piecing together A-lines.

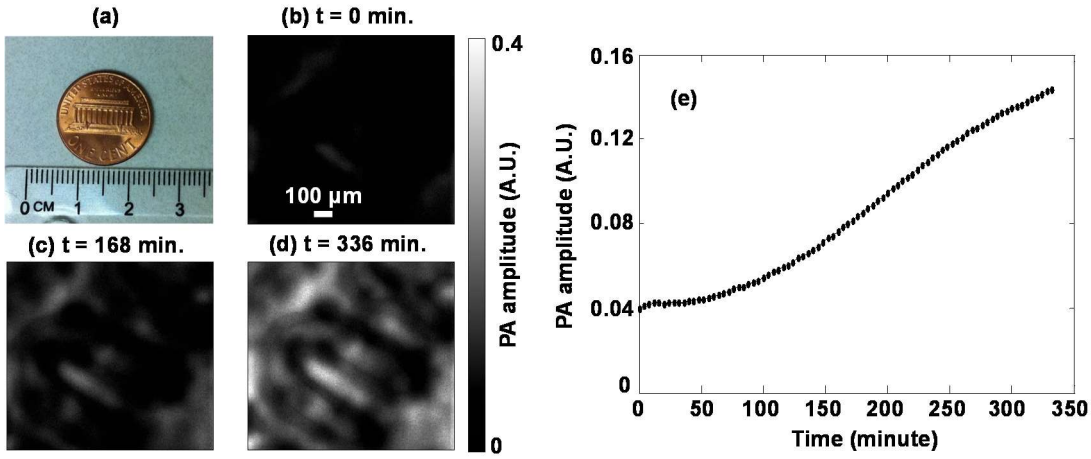

Figure 2.2 Optical clearing-aided PAM of a coin covered by mouse skin. (a) Photograph of the one cent coin used in the experiment. (b)–(d) PA images of the coin at different times during optical clearing. (e) Time course of the PA amplitude averaged over the whole image during optical clearing. The higher PA amplitude indicates that the optical clearing increased penetration depth.

Phantom results First, in a phantom experiment, a U.S. penny [Figure 2.2(a)] covered by a piece of freshly harvested mouse skin was imaged at 570 nm. The phantom was immersed in the glycerol–water solution. As shown in the baseline image [Figure 2.2(b)], there were almost no PA signals from the coin because of the strong scattering of the mouse tissue. During optical clearing, the PA signals from the coin became stronger and stronger, and more features became resolvable, as shown from Figures 2.2(c) and 2.2(d). Figure 2(e) shows the average total PA signal amplitude from the coin versus time; after 250 min, the amplitude increased more than threefold over the baseline value. Note that the PA signals were still increasing at the point when we stopped the experiment. This phantom experiment clearly illustrates that the scattering of the tissue was reduced by optical clearing, and thus the penetration depth was enhanced.

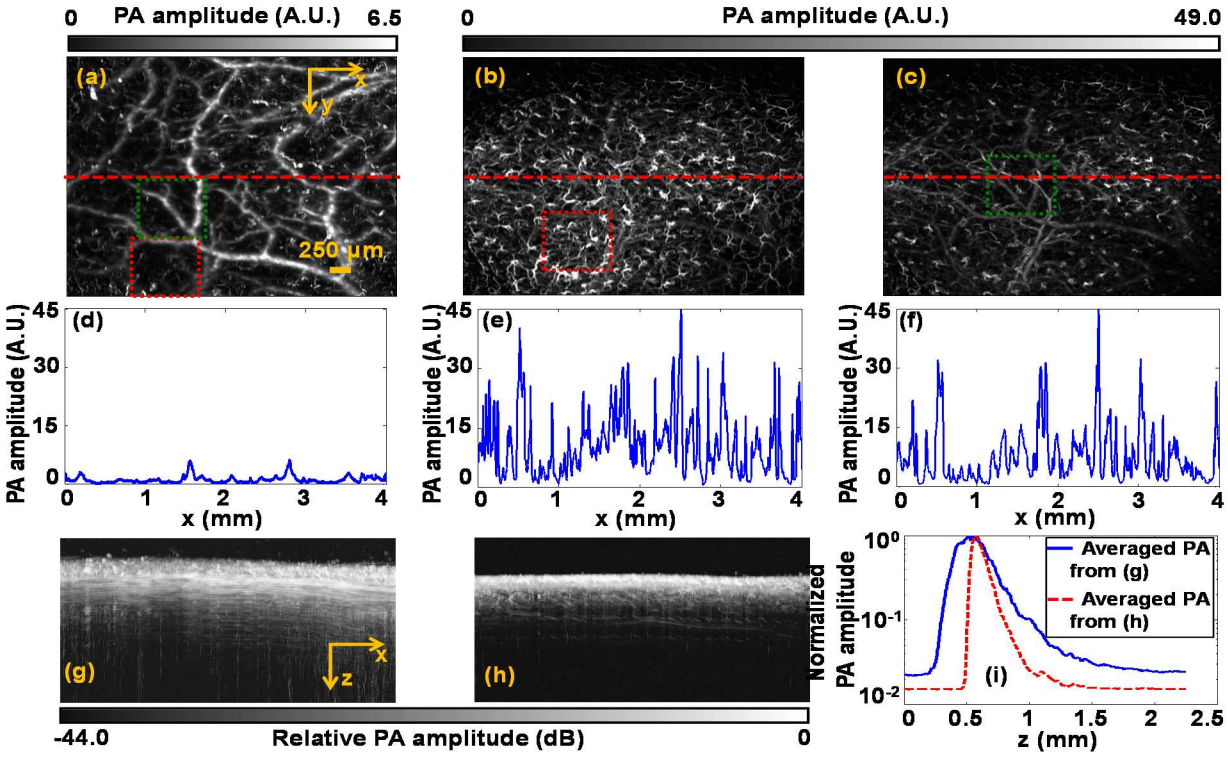

Figure 2.3 *In vivo* PAM of mouse scalp facilitated by optical clearing. (a) PAM image before optical clearing. (b) PAM image with capillaries after optical clearing. (c) PAM image with parts of capillary layer digitally removed after optical clearing. (d)–(f) PA amplitude along the red dashed line in (a)–(c). MAP image along the y axis (g) before and (h) after optical clearing. (i) PA amplitude averaged along the x direction of (g) (blue line) and (h) (red dashed line).

Results Next, we used a nude mouse in an *in vivo* experiment. All experimental animal procedures were carried out in conformance with the laboratory animal protocol approved by the Animal Studies Committee of Washington University in St. Louis. Because the diffusion of glycerol across the epidermal layer is very slow, we directly injected the glycerol–water solution into the mouse scalp to create a local optical clearing window. Figures 2.3(a) and 2.3(b) show the maximum-amplitude-projection (MAP) of the PA images of blood vessels in the mouse scalp before and after optical clearing, respectively. For a better visualization of the deeper vessels in the scalp, we digitally removed most of the superficial capillaries seen in Figure 2.3(b), with the result shown in Figure 2.3(c). From Figures 2.3(a)–2.3(c), we can see a clear PA signal amplitude enhancement

after optical clearing. Three representative lines were taken from Figures 3(a)–3(c) for further comparison, as shown in Figures 2.3(d)–2.3(f). The averaged PA amplitude had increased by about eight times after optical clearing.

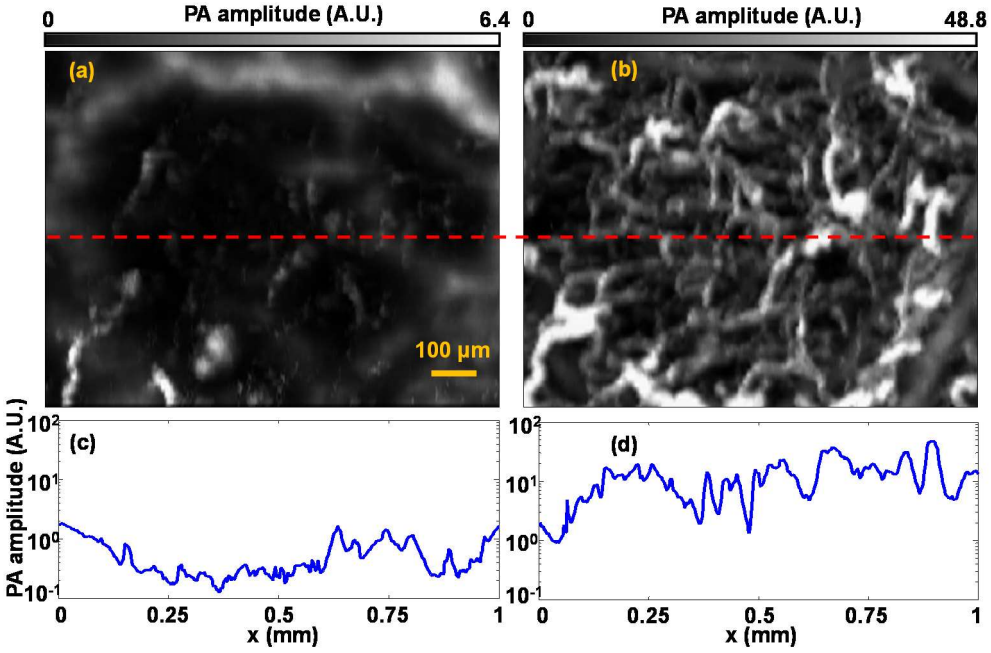

Figure 2.4 Optical clearing reveals more capillaries. (a) and (b) Close-ups of PAM images in the red dashed boxes in Figs. 3(a) and 3(b). (c) and (d) PA amplitudes along the red dashed lines in (a) and (b).

We also quantified the optical clearing effect along the depth direction, as shown in Figures 2.3(g) and 2.3(h). To quantify the total signal enhancement after optical clearing, the averaged PA signal amplitude along the depth was calculated and is shown in Figure 2.3(i). Based on Beer's law, the fitted attenuation coefficients before and after optical clearing were 57.4 and 103.1 cm^{-1}, respectively. At first glance, the attenuation appears to have increased after optical clearing. However, since dehydration due to optical clearing caused the total thickness of the tissue to decrease by about 2.57 times [Figures 2.3(g) and 2.3(h)], the scatter and absorber number density should increase by about 2.57 times. If both the scattering and absorption cross section had

remained constant after optical clearing, the attenuation coefficient should have increased by 2.57 times rather than the 1.80 times observed in the experiment. Thus, the scattering or absorption cross section was reduced after optical clearing. Because optical clearing did not affect the absorption cross section, we concluded that the 0.77 times less increase in the attenuation coefficient resulted from the decrease in the scattering cross section.

The enhanced PA detection sensitivity after optical clearing enabled better capillary imaging [Figure 2.3(b)]. Figures 2.4(a) and 2.4(b) are close-up images of the red dashed-square areas in Figures 2.3(a) and 2.3(b), respectively. The large vessels in the periphery of both images indicate that they are from the same area in the mouse scalp. As shown in Figure 2.4(a), very few capillaries can be detected before optical clearing. However, after optical clearing, more capillaries can be distinctly observed, as shown in Figure 2.4(b). As shown in Figures 2.4(c) and 2.4(d), the vessel density increased by about 10 times after clearing, and the averaged PA signal amplitude from individual capillaries increased by a factor of 22. The much denser capillaries and stronger PA amplitudes in Figure 2.4(d) indicate that, after optical clearing, the local laser fluence at the capillaries was increased. There were two possible reasons for the increased local laser fluence: (1) enhanced focusing on these capillaries due to the dehydration-induced shrinkage of the tissue and (2) reduced scattering loss. As shown in Figure 2.3(i), because of dehydration, the averaged thickness of the tissue decreased from about 0.88 to 0.37 mm. Assuming the light beam intensity had a Gaussian shape, we estimated that the average fluence increase caused by shrinkage was about 5 times. Therefore, we can conclude that the remaining 4.4-fold increase of the PA signal amplitude was due to the decreased scattering coefficient. Because the background noise remained constant during the experiment, the noise-equivalent sensitivity depended only on the PA signal

amplitude. Therefore, sensitivity should also increase 4.4 times due to the decreased scattering coefficient.

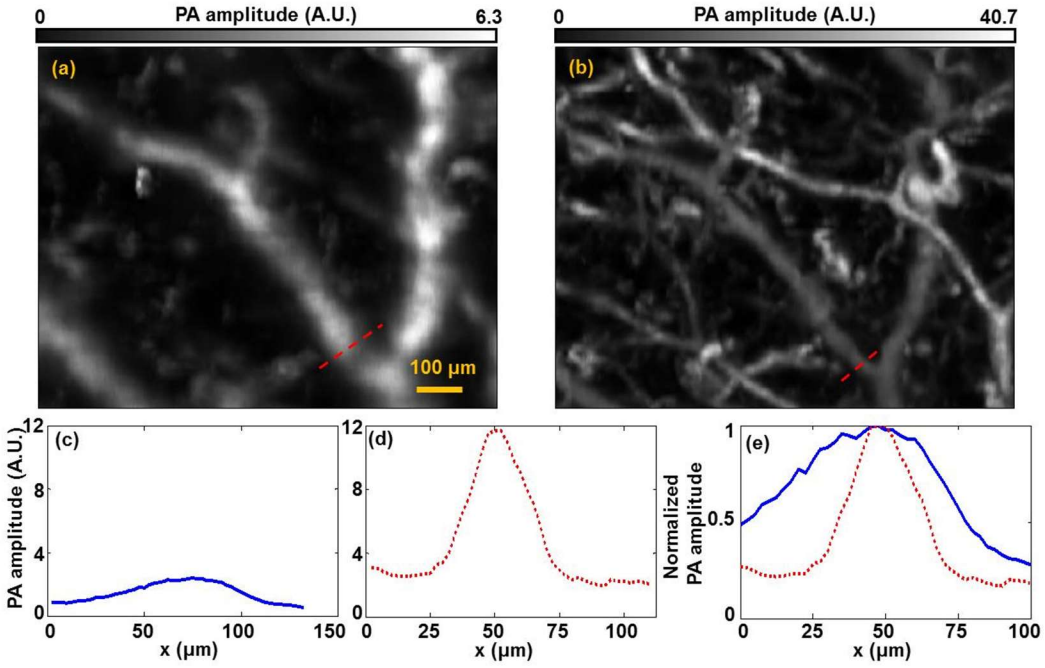

Figure 2.5 Optical clearing improves the lateral resolution for deep vessels. (a) Close-up of PAM image in the green dashed box in Figure 2.3(a). (b) Close-up of PAM image in the green dashed box in Figure 2.3(c). (c) and (d) PA amplitudes along the red dashed lines in (a) and (b). (e) Combined curves in (c) and (d) after normalization.

We further analyzed the lateral resolution enhancement after optical clearing. By zooming in on the deeper vessels in Figures 2.3(a) and 2.3(b), we found that the vessels before optical clearing were much more blurred than those after optical clearing, as shown in Figures 2.5(a) and 2.5(b). Again, the averaged PA amplitude was increased by about 5 times [Figures 2.5(c) and 2.5(d)]. More importantly, we also estimated the lateral resolution improvement by comparing the vessel diameters. As shown in Figure 2.5(e), a representative vessel had nominal diameters of 75 and 30 μm before and after clearing, respectively. We can see that measured vessel diameter decreased at least by 2.5 times after optical clearing. Because the measured vessel diameter was the convolution

of the actual lateral resolution with the true vessel diameter, the actual resolution improvement should be better than 2.5 times.

Discussion There are several widely used OCAs, such as glycerol [33], glucose [34], and propylene glycol. Among these agents, glycerol has both good clearing efficiency and a long effective time. In addition, because glycerol has also been widely used in the medical, pharmaceutical, and chemical fields, it can be easily accessed. Thus, in all experiments, we elected to use glycerol as the OCA to reduce tissue scattering. To achieve a relatively good clearing result and to reduce the potential tissue damage caused by dehydration, a diluted glycerol–water solution (88% vol./vol.) was used. A higher glycerol concentration may enhance the clearing effect with a higher risk of tissue damage [35].

Because glycerol penetrates very slowly through epidermal tissue, we directly injected the glycerol solution into the tissue to accelerate optical clearing. However, injection may lead to side effects, such as bleeding and edema [35]. To use glycerol without injection, we can explore either physical or chemical approaches, such as using a microneedle array or a dimethyl sulfoxide (DMSO) admixture, respectively. Because high-concentration glycerol may block blood flow [36, 37], other safer optical clearing media, such as PEG-400 mixed with thiazone [38, 39], should be explored in the future.

2.2 Photoacoustic Microscopy of Jaundice

Background Bilirubin is a yellow-orange breakdown product of red blood cells. Elevated bilirubin levels (>2.5–3.0 mg/dL) in blood streams and tissues are always associated with physiological disorders, such as jaundice and hyperbilirubinemia [40, 41]. A high bilirubin concentration may cause kernicterus [42], a kind of irreversible brain damage in newborn babies.

Thus, measuring the bilirubin level plays an important role in the diagnosis of jaundice and other diseases. Besides quantifying the average bilirubin level, determination of its spatial distribution provides additional information for such diagnoses. It has been suggested that measuring both the serum and the transcutaneous bilirubin levels concurrently will enable a more accurate identification of jaundice [43, 44]. In addition, measuring the bilirubin distribution may provide opportunities to study kernicterus (by analyzing the movement of bilirubin across the blood-brain barrier and its deposition into the brain tissue) [43, 45, 46], to estimate the age of bruises in forensic medicine [47], and to reveal the bilirubin photochemistry interaction during phototherapy [48, 49].

Current techniques for bilirubin measurement have various limitations. The conventional approach to measuring bilirubin concentration involves extracting blood, which is invasive, and only the total serum bilirubin level can be monitored, without any spatial information. Noninvasive monitoring methods include diffuse reflectance [50-52] and hyperspectral imaging [47, 53]. The former senses the overall concentration of bilirubin in the skin without spatial resolution, whereas the latter maps the relative bilirubin distribution without quantification. Therefore, we still lack a technique for quantitative imaging of bilirubin.

Since it was first introduced in 2005, photoacoustic microscopy (PAM) has been proven to be a promising modality for both structural and functional imaging. In PAM, the object is irradiated by a short-pulsed laser. Following the absorption of light, a temperature rise generates an initial pressure rise, which is propagated as a photoacoustic wave. This photoacoustic wave is then detected by a focused ultrasonic transducer. Because the initial pressure is proportional to the local energy absorbed, photoacoustic measurements with multiple optical wavelengths can provide spectral information of optical absorption. Based on the different absorption spectra of oxyhemoglobin and deoxyhemoglobin, the oxygen saturation of hemoglobin (sO_2) has been

successfully quantified by PAM with high accuracy and spatial resolution. In addition, PAM has shown its feasibility to detect other intrinsic contrasts in biological tissue, such as DNA and RNA in nuclei, water, lipid, cytochrome c, and melanin.

The motivation of this work is to image bilirubin distribution quantitatively by using PAM. We first demonstrated that our PAM system was capable of measuring the absorption spectra of bilirubin and blood (including oxyhemoglobin and deoxyhemoglobin). Based on the absorption spectra, proper wavelengths were chosen to measure pure bilirubin samples and mixed bilirubin-blood samples. Then the root-mean-square error of prediction (RMSEP) in both the pure and mixed samples was measured. Last, the bilirubin distributions in tissue-mimicking samples were imaged both without and with underlaid mouse skins. We showed for the first time that bilirubin, both inside and outside the blood vessels, can be imaged quantitatively by PAM with relatively high accuracy.

Methods and Materials A free-space transmission-mode PAM system was utilized for bilirubin detection, as shown in Figure 2.6. The laser pulse (5 ns pulse width, 1 KHz pulse repetition rate), with a wavelength tunable from 210 nm to 2600 nm, was generated by an integrated diode-pumped Q-switched laser and optical parametric oscillator system (NT242-SH, Ekspla). The pulse was then filtered by 2 mm iris (ID25SS, Thorlabs) to remove the nonuniform rim. After being reflected by a mirror (PF10-03-G01, Thorlabs), focused by a condenser lens (LA4380, Thorlabs), and filtered by a 50 μm pinhole (P50C, Thorlabs), the light beam was focused by an optical objective with 0.3 numerical aperture (NA). The excited photoacoustic waves were detected by a focused ultrasonic transducer (40 MHz central frequency, 80% bandwidth, and 0.5 NA). The ultrasonic transducer and optical objective were aligned coaxially and confocally to achieve high sensitivity. Each laser pulse yielded a one-dimensional depth-resolved image (A-line) by recording the arrival

times of photoacoustic signals. A two-dimensional (2D) scanning stage (PLS-85, MICOS) held the sample and provided lateral scanning. We rendered our result in the form of a 2D maximum amplitude projection (MAP) image, which was produced by projecting the maximum amplitude of the 3D image along the axial direction.

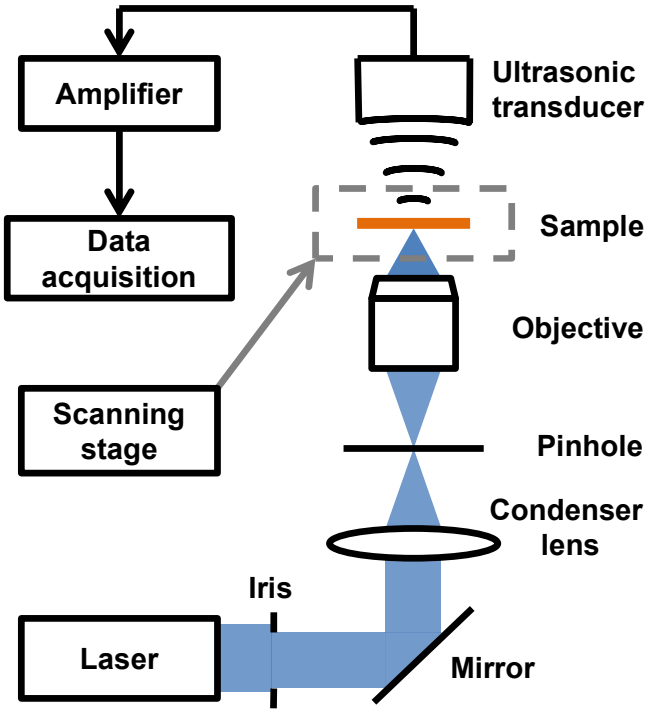

Figure 2.6 Schematic of the PAM system.

In the experiments, bilirubin powder (B4126, Sigma-Aldrich) was dissolved in dimethyl sulfoxide solution (Fisher Scientific) and further diluted by water. To prepare the pure tissue-mimicking sample, the bilirubin solution was mixed with 5% gelatin (G1890, Sigma-Aldrich) and 1% intralipid (Fresenius Kabi). The congealed sample had a thickness of 0.5 mm and an optical scattering coefficient of approximately 100 cm^{-1}. To prepare the mixed sample (to mimic blood vessels), the bilirubin solution was mixed with lysed bovine blood with a 75% sO_2 (905-250, Quad Five). Oxygenated hemoglobin was prepared by mixing oxygen with lysed bovine blood (905-

250, Quad Five) for 2 h. Deoxygenated hemoglobin was prepared by adding 33 mg of sodium hydrosulfite (71699-50, Sigma-Aldrich) to 10 ml of lysed bovine blood (905-250, Quad Five). The 75% sO_2 blood was prepared by mixing oxyhemoglobin and deoxyhemoglobin at a ratio of 1:3 and measured by an oximeter for validation. To mimic a blood vessel, the mixture was then contained in a microtube (made of platinum-cured silicone) with an inner diameter of 300 μm and an outer diameter of 600 μm (60985-700, VWR). To mimic the varied physiological levels in real patients, phantoms were prepared with different concentrations of bilirubin.

The PAM system was calibrated with pure samples with preset bilirubin concentrations of 2, 4, 6, and 8 mg/dL, and with a preset blood concentration of 148 g/L for quantification. The sO_2 was set to be ~75%. The A-lines from each sample (prepared as described previously) were averaged 10,000 times at each optical wavelength. The peak PA signal amplitude versus the wavelength was used to separately calculate the concentration by weighted least squares fit with the photoacoustic spectra of bilirubin and blood. We repeated this calibration procedure for the samples overlaid with mouse skins of different thicknesses (200 μm, 400 μm, and 600 μm) in order to obtain quantitative results at these depths.

Both the calibration and concentration measurements can be described by the following equations:

$$\varphi_{bi}(\lambda) = k_{bi} \cdot \varepsilon_{bi}(\lambda) C_{bi} \tag{2.1}$$

$$\varphi_{ox}(\lambda) = k_{ox} \cdot \varepsilon_{ox}(\lambda) C_{ox} \tag{2.2}$$

$$\varphi_{de}(\lambda) = k_{de} \cdot \varepsilon_{de}(\lambda) C_{de}, \tag{2.3}$$

where $\varphi_{bi}(\lambda)$, $\varphi_{ox}(\lambda)$, and $\varphi_{de}(\lambda)$ are the wavelength-dependent photoacoustic signal amplitudes normalized with the laser pulse energy (recorded in mV/nJ) of bilirubin, oxyhemoglobin, and deoxyhemoglobin, respectively; $\varepsilon_{bi}(\lambda)$, $\varepsilon_{ox}(\lambda)$, and $\varepsilon_{de}(\lambda)$ are the wavelength dependent molar

absorption coefficients of bilirubin, oxyhemoglobin, and deoxyhemoglobin, respectively; C_{bi}, C_{ox}, and C_{de} are the concentrations of bilirubin, oxyhemoglobin, and deoxyhemoglobin, respectively; and k_{bi}, k_{ox}, *and* k_{de} are the calibration factors for bilirubin, oxyhemoglobin, and deoxyhemoglobin, respectively. For calibration, C_{bi}, C_{ox}, and C_{de} were known, while k_{bi}, k_{ox}, and k_{de} were calculated by weighted least squares fitting. k_{bi}, k_{ox}, and k_{de} were slightly different due to differences among the samples. For concentration measurement, k_{bi}, k_{ox}, and k_{de} were from the calibration, while C_{bi}, C_{ox}, and C_{de} were calculated by weighted least squares fitting. Here the variances of the photoacoustic signals are used in the least squares fits as weighting terms.

For the mixture of bilirubin and blood, we can calculate all bilirubin, oxyhemoglobin, and deoxyhemoglobin concentrations by fitting the bilirubin and blood absorption spectra to the photoacoustic signals:

$$\varphi(\lambda) = k_{bi} \cdot \varepsilon_{bi}(\lambda) C_{bi} + k_{ox} \cdot \varepsilon_{ox}(\lambda) C_{ox} + k_{de} \cdot \varepsilon_{de}(\lambda) C_{de}, \tag{2.4}$$

where $\varphi(\lambda)$ is the wavelength-dependent photoacoustic signal amplitude.

To describe the measurement precision, the RMSEP of the concentration can be defined as

$$\mathrm{RMSEP}(C) = \sqrt{e_s^2 + e_r^2}\,. \tag{2.5}$$

where systematic error e_s and random error e_r are defined as

$$e_s = \sqrt{\sum_{i=1}^{n} (M_i - C_i)^2 / n}\,, \tag{2.6}$$

and

$$e_r = \sqrt{\sum_{i=1}^{n} \delta M_i^{\,2} / n}\,, \tag{2.7}$$

respectively. Here, C_i, M_i, and δM_i are the preset concentration, mean measured concentration, and measurement standard deviation of the ith sample, respectively; and n is the total number of samples. RMSEP denotes the measurement error by combining in quadrature both the systematic error and random error. The systematic error describes the root-mean-squared difference between

the measurement and the actual value, mostly likely originating from instrument calibration errors. The random error describes the measurement fluctuation without averaging, most likely originating from noise.

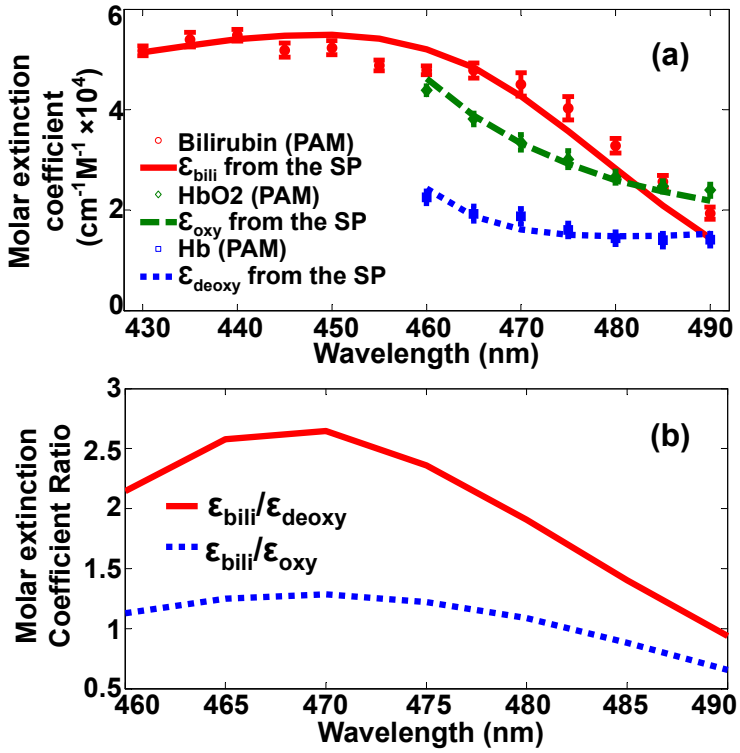

Figure 2.7 Absorption spectra of bilirubin, oxyhemoglobin, and deoxyhemoglobin. (a) Relative absorption spectra of bilirubin, oxyhemoglobin, and deoxyhemoglobin measured by PAM scaled by fitting to the spectrophotometer measurement. (b) The molar extinction coefficient ratio between bilirubin, oxyhemoglobin, and deoxyhemoglobin in the wavelength range from 460 nm to 490 nm. μ_{bili}: relative absorption coefficient of bilirubin. ε_{bili}: molar extinction coefficient of bilirubin. μ_{oxy}: relative absorption coefficient of oxyhemoglobin. ε_{oxy}: molar extinction coefficient of oxyhemoglobin. μ_{deoxy}: relative absorption coefficient of deoxyhemoglobin. ε_{deoxy}: molar extinction coefficient of deoxyhemoglobin. SP: spectrophotometer.

To quantitatively map the concentration distribution of bilirubin in various samples, the samples were imaged at multiple wavelengths, and each pixel of the co-registered multi-wavelength images was analyzed by the above method as described by Equation 2.4. To obtain the statistical 'volume-averaged' data, we set a threshold of five times the noise level to separate the sample and the

background, and then averaged the signals within each sample to get our final mean concentration value.

Results We used PAM to measure the absorption spectra of bilirubin, oxyhemoglobin, and deoxyhemoglobin by using pure bilirubin (2 mg/dL) and blood (37 g/L) solutions, respectively. The relative optical absorption at each wavelength was calculated from the average PA signal amplitude normalized by the laser pulse energy. Figure 2.7(a) shows the absorption spectra of bilirubin, oxyhemoglobin, and deoxyhemoglobin measured by the PAM system, all fitting well to the absorption spectra measured with a spectrophotometer (Cary 50 Bio UV/ Visible, VARIAN). The residual systematic difference between the bilirubin spectra may have resulted from instrument errors. Because bilirubin has a relatively high absorption in the wavelength range from 430 nm to 490 nm, we chose this range for the bilirubin measurement. Likewise, because the absorption ratio between bilirubin and blood is relatively high in the wavelength range from 460 nm to 490 nm [Figure 2.7(b)], which enables an easier differentiation of bilirubin from blood, we chose this range for the blood absorption spectrum detection. Also, the wavelength range from 540 nm to 545 nm was chosen, where blood has high absorption [Figure 2.7(a)], but bilirubin has almost no absorption. We used theses component spectra measured by PAM as the standard to decompose spectra of mixtures for the concentrations of bilirubin, oxyhemoglobin, and deoxyhemoglobin.

We quantified the accuracy of bilirubin concentration measurements by PAM in both pure and mixed samples. The tissue-mimicking samples for the pure bilirubin measurements were the same as those used in the calibration (bilirubin concentrations of 2, 4, 6, and 8 mg/dL; thickness of 200 μm). The optical wavelength was varied from 430 nm to 460 nm. The bilirubin concentration could be calculated simply from the PA signal amplitudes after calibration, as shown in Figure 2.8(a).

The RMSEP of the concentration was calculated by Eq. (5) to be 0.52 mg/dL for the pure bilirubin samples, where the systematic error is 0.17 mg/dL and the random error is 0.49 mg/dL.

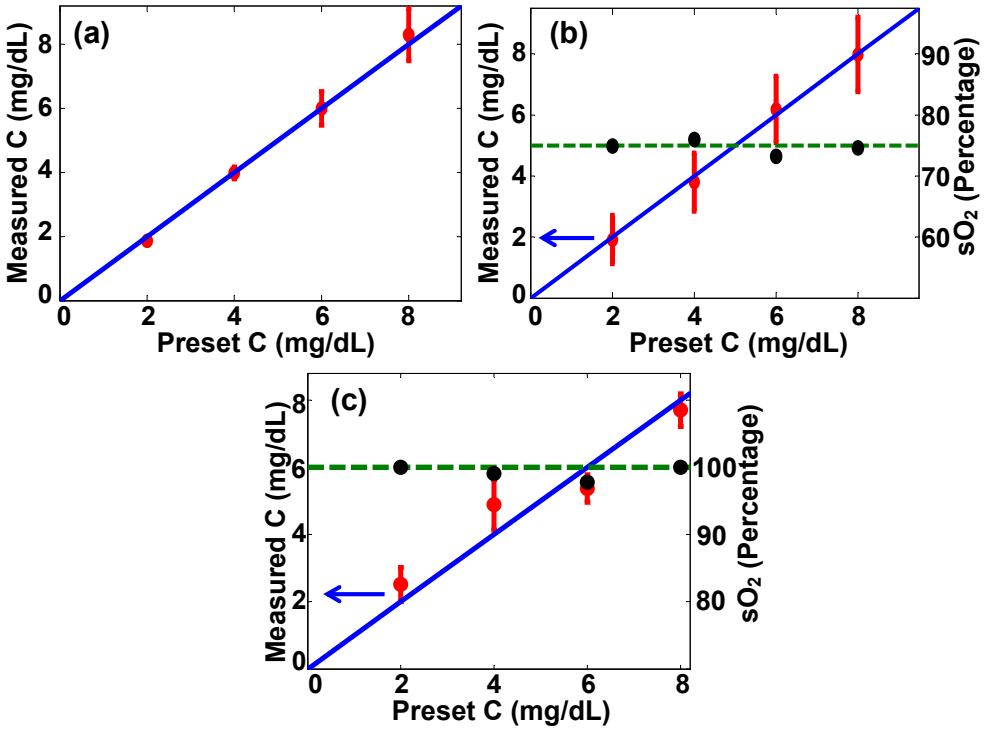

Figure 2.8 The measured bilirubin concentration (C) of each sample versus the preset concentration. (a) Pure bilirubin phantom. Bilirubin solution mixed with (b) 75% sO_2 blood and (c) 100% sO_2 blood. Red circle: experimental measurement of C. Blue solid line: ideal fit if the measured and preset concentrations are identical. Black circle: experimental measurement of sO_2. Green dashed line: preset sO_2. For the bilirubin blood mixture sample with 75% sO_2 and 100% sO_2, the RMSEP of the concentration for bilirubin is calculated to be 1.04 mg/dL and 0.83 mg/dL, respectively.

For the mixed-sample measurement, we used four samples with bilirubin-to-blood concentration ratios of 2, 4, 6, and 8 mg/dL of bilirubin to 148 g/L of blood. Two wavelength ranges were chosen for this experiment. One was from 460 nm to 490 nm, where the molar extinction coefficient ratio between bilirubin and blood is relatively high, as shown in Figure 2.7(b). The other was from 540 nm to 545 nm, where blood has high absorption, but bilirubin has almost no absorption. The measurements for the mixed samples with 75% and 100% sO_2 are shown in Figure 2.8(b) and

Figure 2.8(c), respectively. According to Equation 2.5, the RMSEP value of the bilirubin for the 75% sO_2 mixed samples was calculated to be 1.04 mg/dL, where the systematic error is 0.14 mg/dL and the random error is 1.03 mg/dL. For the 100% sO_2 mixed samples, the RMSEP value was 0.86 mg/dL, where the systematic error was 0.62 mg/dL and the random error was 0.55 mg/dL. Also, as shown in Figures 2.8(b) and 2.8(c), the sO_2 value can be recovered in the mixture.

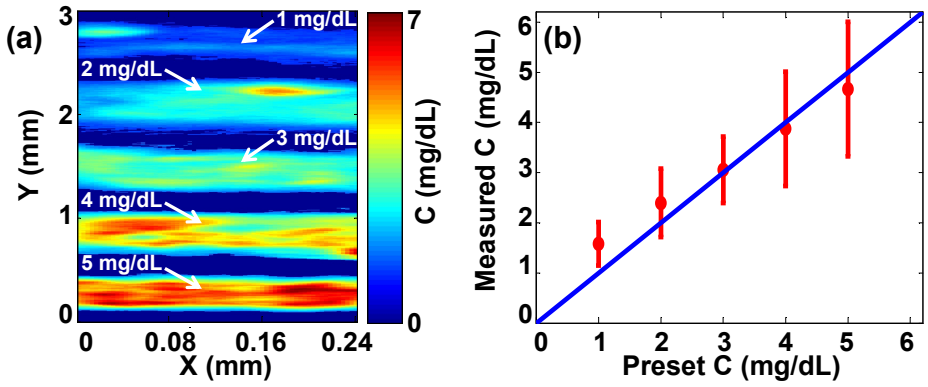

Figure 2.9 Quantitative PAM of tissue-mimicking samples containing bilirubin with varied concentrations. (a) Bilirubin distribution image. From top to bottom in the image, the sample concentrations are 1, 2, 3, 4, and 5 mg/dL, respectively. (b) Volume-averaged bilirubin concentrations from the PAM measurements in each sample. Red circle: experimental measurement. Blue line: ideal fit if the measured and preset concentrations are identical.

Next, we implemented quantitative PAM of pure bilirubin samples. Five congealed samples with different volume-averaged bilirubin concentrations (1, 2, 3, 4, and 5 mg/dL) were prepared as described above, which covered the normal and elevated bilirubin levels in humans. Each sample was cylindrical with a diameter of about 0.5 mm (determined by the inner diameter of the metal tube used as the sample mold), and the space between the samples was filled with ultrasonic gel. With a step size of 2 μm, a 3 mm by 0.3 mm area was scanned at 430 nm wavelength, where bilirubin has a strong absorption, to acquire PAM images of bilirubin distributions. The volume-averaged concentrations of bilirubin in the samples were set to be 1 mg/dL to 5 mg/dL, from the top to the bottom of Figure 2.9(a). The measured average concentration of bilirubin in each sample

was in accordance with the preset concentration, as shown in Figure 2.9(b). The results show that the PAM system not only can measure the bilirubin concentration but also can provide its spatial information in the pure bilirubin sample.

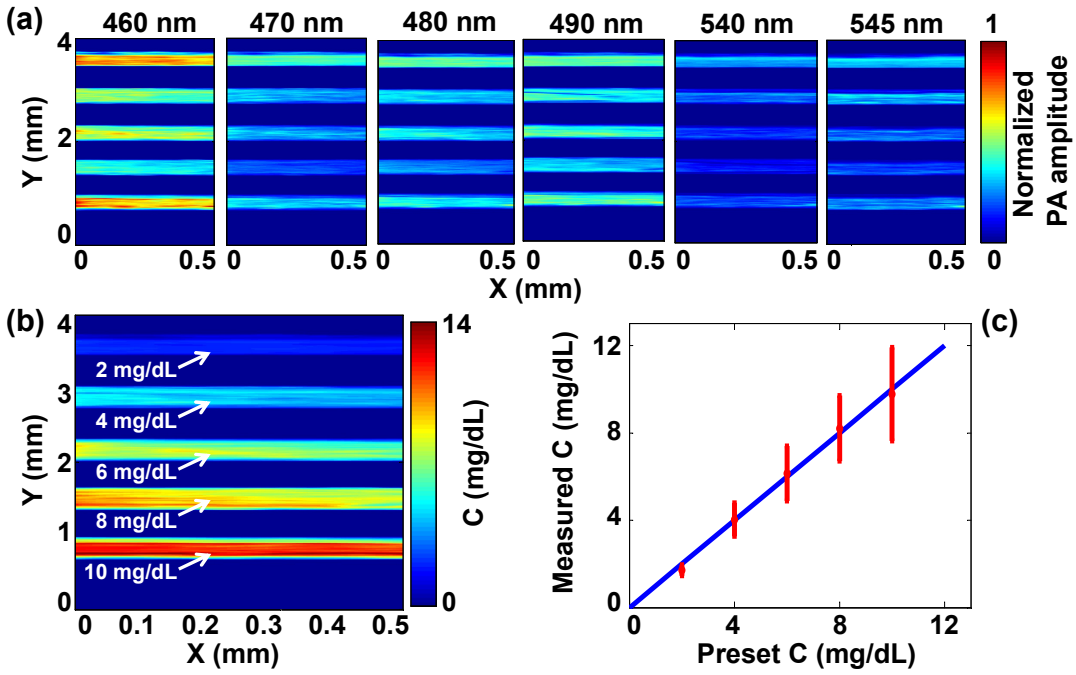

Figure 2.10 Multi-wavelength PAM of the mixtures of bilirubin and blood (75% sO_2). (a) Quantitative PAM images at six optical wavelengths. (b) Bilirubin distribution image calculated from the multi-wavelength PAM images. From top to bottom in the image, the bilirubin concentrations are 2, 4, 6, 8, and 10 mg/dL, respectively, whereas the blood concentration is 148 g/L. (c) Volume-averaged bilirubin concentration from the PAM measurements in each tube. Red circle: experimental measurement. Blue line: ideal fit if the measured and preset concentrations are identical.

We also detected the bilirubin spatial distribution in the mixed samples with 75% sO_2. Wavelengths of 460, 470, 480, 490, 540, and 545 nm were selected. Solutions with bilirubin-to-blood ratios of 2, 4, 6, 8 and 10 mg/dL to 148 g/L were prepared, corresponding to both normal and elevated ratios in physiology. Five tubes with the same diameters as in the previous experiment held the mixture samples. Here, a 4 mm by 0.5 mm area was scanned with a step size of 2 μm. The

PAM images of the mixed solutions acquired at each wavelength are shown in Figure 2.10(a). Since blood has much higher absorption than bilirubin, it is difficult to distinguish the bilirubin concentrations based merely on a single image. However, based on the multi-wavelength images, the image of the bilirubin concentration distribution can be calculated and is shown in Figure 2.10(b). The average bilirubin-to-blood ratios in the sample, from top to bottom, ranged from 2 mg/dL to 10 mg/dL of bilirubin to 148 g/L of blood. The measured average concentrations of bilirubin are in fair accordance with the preset concentrations, as shown in Figure 2.10(c).

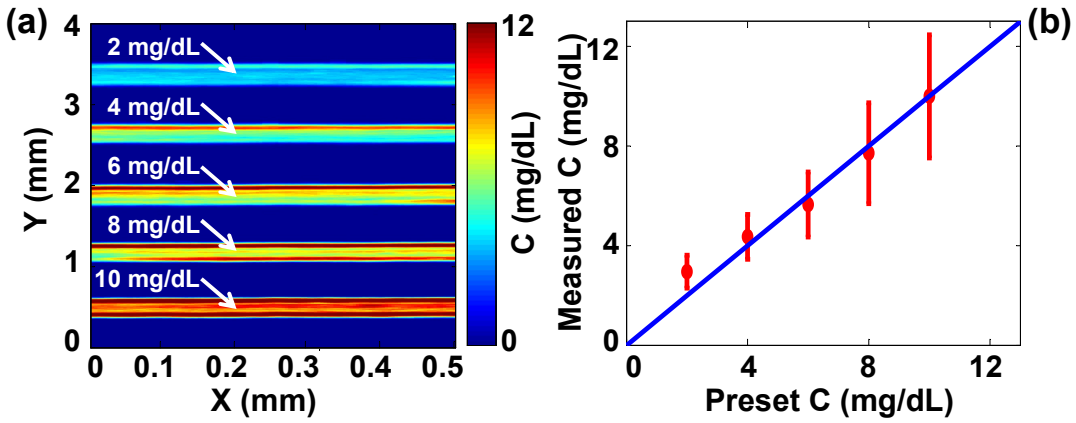

Figure 2.11 Multi-wavelength PAM of the mixtures of bilirubin and blood (100% sO_2). (a) Bilirubin distribution image calculated from the multi-wavelength PAM images. From top to bottom in the image, the bilirubin concentrations are 2, 4, 6, 8, and 10 mg/dL, respectively, whereas the blood concentration is 148 g/L. (b) Volume-averaged bilirubin concentration from the PAM measurements in each tube. Red circle: experimental measurement. Blue line: ideal fit if the measured and preset concentrations are identical.

Similarly, we detected the bilirubin spatial distribution in the mixed samples with 100% sO_2. The image of the bilirubin concentration distribution is shown in Figure 2.11(a). The measured average concentrations of bilirubin are shown in Figure 2.11(b). The results in Figures 2.10 and 2.11 illustrate that PAM can quantitatively image bilirubin distributions in the presence of blood.

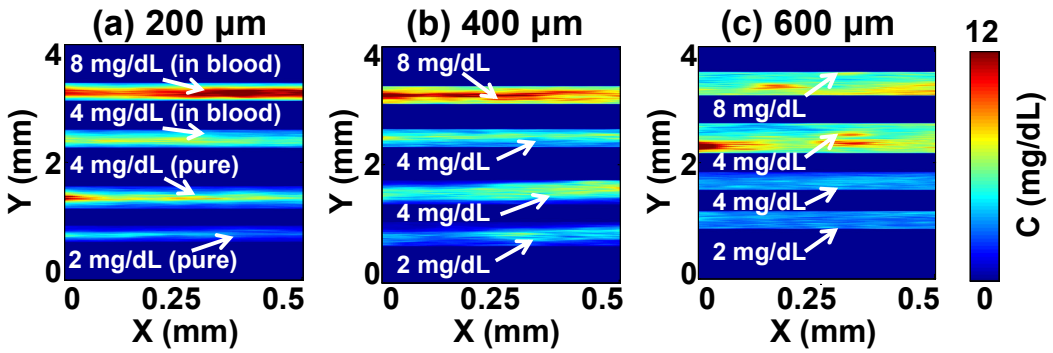

Figure 2.12 PAM of tissue phantoms with varied bilirubin concentrations. The three images are acquired with underlaid mouse skins with thickness of 200 μm (a), 400 μm (b), and 600 μm (c), respectively. For every image, the upper two tubes are bilirubin solutions mixed with blood. The concentration ratios between bilirubin and blood are 8 mg/dL : 148 g/L and 4 mg/dL : 148 g/L, respectively. The lower two samples are pure bilirubin phantoms with concentrations of 4 mg/dL and 2 mg/dL, respectively.

Finally, to further demonstrate the ability of PAM to measure bilirubin distribution in biological tissue, pure and mixed samples underlaid by mouse skins (light illuminated from the bottom) were imaged simultaneously. Fresh mouse skins, with thicknesses of 200 μm, 400 μm, and 600 μm, were used to underlay the samples. Pure bilirubin samples with concentrations of 2 mg/dL and 4 mg/dL and mixed samples with bilirubin-to-blood ratios of 4 mg/dL and 8 mg/dL to 148 g/L (75% sO_2) were prepared. In each experiment, a 4 mm by 0.5 mm area was scanned, with a step size of 2 μm (Figure 2.12). In every image of Figure 2.12, the upper two samples are bilirubin solutions mixed with blood (with concentration ratios of 8 mg/dL and 4 mg/dL to 148 g/L), and the lower two samples are pure bilirubin phantoms (with concentrations of 4 mg/dL and 2 mg/dL). For pure and blood-mixed bilirubin, the detection procedure was the same as discussed before. The skin thicknesses in Figures 2.12(a), (b), and (c) were 200, 400, and 600 μm, respectively. From Figure 2.12, we can see that the measured bilirubin concentrations were consistent with the preset values when the skin thicknesses were 200 and 400 μm. However, when the thickness of skin increased to 600 μm, the measurements were less accurate. Table 2.1 shows bilirubin measurements between

phantoms without and with underlaid mouse skins is shown. With skin underlaid (200 μm and 400 μm), the measurement accuracy is similar to that without skin underlaid. However, when the skin thickness increases to 600 μm, the results are less accurate because of the low signal-to-noise ratio (SNR). Thus, at least a 400 μm penetration depth can be achieved by our method in measuring bilirubin concentration both inside blood vessels (i.e., the mixed samples) and outside blood vessels (i.e., the pure samples).

Bilirubin C measured by PAM				
	Pure bilirubin phantoms		Blood mixed solutions	
	2 mg/dL	4 mg/dL	4 mg/dL	8 mg/dL
No skin	2.40 ± 0.68	3.88 ± 1.14	4.03 ± 0.76	8.21 ± 1.50
200 μm	2.05 ± 1.02	3.97 ± 2.03	4.45 ± 1.33	7.74 ± 2.89
400 μm	2.23 ± 1.23	3.73 ± 1.77	4.03 ± 1.13	7.72 ± 2.16
600 μm	3.00 ± 0.48	3.01 ± 0.65	6.09 ± 1.30	5.83 ± 1.86

Table 2.1 Bilirubin concentrations measured by PAM in various phantoms without and with underlaid mouse skins.

Discussion In these tissue phantom experiments, the quantitative measurements down to 400 μm in depth rely on accurate calibration. The influences of ultrasound refraction/reflection and depth dependence of fluence may be very difficult to calibrate in future *in vivo* experiments. However, since bilirubin is located shallow in the skin (tens of micrometers, both in the dermis and epidermis), we should be able to map bilirubin distribution *in vivo* with reasonable accuracy within tens of micrometers of depth, similar to measuring oxygen saturation (sO_2) *in vivo*.

There are four main types of absorbers in the visible spectral range in the skin: oxyhemoglobin, deoxyhemoglobin, bilirubin, and melanin. In blood vessels, absorption mainly originates from oxyhemoglobin, deoxyhemoglobin, and bilirubin; while outside the blood vessel absorption is mainly due to bilirubin and melanin. As our work was focused on demonstrating the feasibility of PAM measurements of bilirubin concentration and distribution, the influence of melanin in the

pure bilirubin was not taken into account. However, in principle, if we choose at least four optical wavelengths, each absorber's concentration can be quantified.

As discussed above, to measure the pure bilirubin distribution, only one wavelength is needed. For bilirubin mixed with blood, with sufficient SNR, three wavelengths are enough to differentiate the concentration of bilirubin from that of blood. But more wavelengths (as used in our experiments) provide more data to obtain a more accurate least squares fit because the SNR is improved. However, using more wavelengths to measure the sample would take longer, which could be an important concern for *in vivo* imaging. Thus, there is a trade-off between accuracy and speed. To reduce the measurement time, voice-coil scanning [54] or laser scanning [55] can be utilized in the future.

A transmission-mode PAM system was used to detect bilirubin distribution in this work. For clinical applications, it is difficult to measure the skin by transmission-mode PAM because of the large thickness of the tissue. Thus, it is preferred to use reflection-mode PAM, which can be achieved by the use of a parabolic mirror with a central hole for light delivery [56].

When a healthy human with a very low bilirubin level in blood is imaged, PAM currently may not be able to provide accurate quantitative results. But PAM can complement other techniques, such as blood analysis, by providing the spatial distribution of bilirubin noninvasively. With further development of our technique, we expect to detect relative levels of albumin conjugated bilirubin, which is of clinical significance [57]. Blood analyses can be used to measure the total serum bilirubin level for a quantitative validation.

2.3 Photoacoustic Microscopy of Red Blood Cell Aggregation

Background Over the past few years, PAM has been proven to be capable of structural, functional, molecular, and metabolic imaging. In PAM, the object is illuminated by a short-pulsed laser beam. Following the absorption of light, the increased temperature generates an initial pressure rise, which propagates as PA waves and is detected by an ultrasonic transducer. Because the initial pressure is directly proportional to the absorbed optical energy density $A(\vec{r})$ ($J \cdot m^{-3}$) in the tissue, which is the product of the optical fluence $F(\vec{r})$ ($J \cdot m^{-2}$) and the optical absorption coefficient $\mu_a(\vec{r})$ (m^{-1}), multi-wavelength PA measurements can provide spectral information of optical absorption. Moreover, because it is essentially background free for blood-vessel imaging, PAM has better imaging contrast than other back-scattering-based optical imaging modalities. So far, PAM has shown its viability in detecting many intrinsic contrasts in biological tissues, such as hemoglobin, bilirubin, DNA and RNA in nuclei, lipid, cytochromes, and melanin. To obtain the intrinsic contrast property $\mu_a(\vec{r})$, we need to compensate for the extrinsic quantity $F(\vec{r})$. However, the optical fluence is usually unknown because of the light attenuation in tissue. Therefore, it is generally challenging to provide quantitative PA studies of, for example, oxygen metabolism.

Currently, the optical fluence $F(\vec{r})$ can be compensated for either invasively [58] or noninvasively [59-64]. In the invasive method, an optical absorber with *a priori* known absorption spectrum is placed close to the target of interest and used as a reference. PA amplitude from the target of interest is normalized by the measured PA amplitude of this reference absorber. A noninvasive method involves solving both optical diffusion and PA wave equations. However, the inverse problems are computationally intensive and ill-posed due to optical diffusion. In another

noninvasive method, the temporal profiles of PA signals are used to determine the absolute absorption coefficient [65-68]. However, the acoustic attenuation and the limited bandwidth of the transducer may distort the PA signals. Thus, the direct fitting method may be inaccurate. To avoid this issue, our group has proposed to use acoustic spectra to determine the absolute absorption coefficient [69, 70].

Here we present another quantitative approach to measure absolute absorber concentrations by statistical analyses of PA signals. To obtain a fluence-independent detection, the particle count in the detection volume needs to be small enough so that PA signal fluctuation due to the particle Brownian motion is dominant compared to other fluctuating sources, such as laser intensity fluctuation, electronic thermal noise, and photon shot noise. This method is analogous to fluorescence correlation spectroscopy and dynamic light scattering (also known as photon correlation spectroscopy). The former has been widely used to measure the fluorescence intensity fluctuations, while the latter has been used to measure the scattered light intensity fluctuations.

The part of dissertation is organized as follows. We first developed a model to describe the relationship between the measured PA signal and the particle count. The principle was then demonstrated experimentally. After samples of varied microsphere concentrations were studied, red blood cells (RBCs) were measured to show that our method can be applied to biological samples. Finally, we performed *in vivo* experiments to demonstrate the potential of our method in biological applications.

Methods and Materials Particle fluctuation in a detection volume caused by Brownian motion is governed by Poisson distribution [71]. Thus, the variance of the particle count (N_p) equals its mean, i.e.,

$$Var(N_p) = E(N_p). \tag{2.8}$$

where Var() denotes the variance, and E() denotes the mean. Fluctuations of the particle count contribute to the PA signal fluctuations, which were assessed with multiple laser pulses. However, other sources could also lead to fluctuations in the PA signal, such as laser intensity fluctuation, electronic thermal noise, and photon shot noise. Because the photon shot noise is much smaller than the electronic thermal noise in PAM, it can be ignored. In a typical PA system, a photodiode (PD) is used to compensate for the laser pulse energy fluctuations. A beam sampler is used to extract a small portion of light into PD, while the remaining light illuminates the sample. The output of photodiode amplitude (A_{PD}) can be expressed as

$$A_{PD} = k_{PD} R N_{ph} + n_{PD}, \tag{2.9}$$

where k_{PD} is the efficiency of conversation from photons to voltage; R is the percentage that light reflects from the beam sampler; N_{ph} is the photon count of the incident light; and n_{PD} is the PD electronic thermal noise after the mean value is subtracted. The photon count fluctuation is typically specified as a few percent of average pulse energy, hence the variance of photon count fluctuation can be assumed to be proportional to the square of mean photon counts:

$$Var(N_{ph}) = \alpha^2 E^2(N_{ph}), \tag{2.10}$$

where α denotes the photon count fluctuation coefficient. Parameter α is a property of the laser but it can be controlled to some extent by discarding laser pulses outside of the predetermined range of pulse energies.

Because the thermal noise is zero-mean, the mean and variance of A_{PD} are derived from Equation 2.9 as

$$E(A_{PD}) = k_{PD} R E(N_{ph}), \tag{2.11}$$

$$Var(A_{PD}) = k_{PD}^2 R^2 Var(N_{ph}) + Var(n_{PD}). \tag{2.12}$$

Based on Equations 2.11 and 2.12, we have

$$Var(A_{PD}) = \alpha^2 E^2(A_{PD}) + Var(n_{PD}). \tag{2.13}$$

Equation 2.13 shows a parabolic relationship between $Var(A_{PD})$ and $E(A_{PD})$.

Similar to the analysis of PD, the PA amplitude (A_{PA}) can be expressed as

$$A_{PA} = k_{PA} N_p T N_{ph} + n_{PA}, \tag{2.14}$$

where k_{PA} is a constant factor including Grueneisen parameter, heat conversion percentage, absorption cross section, and other minor contributors; N_p is the particle count inside the detection volume; T is the percentage that light transmits through the beam sampler; and n_{PA} is the electronic thermal noise of the ultrasonic transducer. Note that R + T is slightly less than unity due to absorption and scattering loss.

Based on Equation 2.14, the mean and the variance of A_{PA} are

$$E(A_{PA}) = k_{PA} E(N_p) T E(N_{ph}), \tag{2.15}$$

$$\begin{aligned} Var(A_{PA}) &= k_{PA}^2 Var(N_p T N_{ph}) + Var(n_{PA}) \\ &= k_{PA}^2 T^2 [Var(N_p) E^2(N_{ph}) + Var(N_{ph}) E^2(N_p) + Var(N_p) Var(N_{ph})] + Var(n_{PA}) \end{aligned}. \tag{2.16}$$

Substituting Equation 2.8 into Equation 2.16, we have

$$\begin{aligned} Var(A_{PA}) &= k_{PA}^2 T^2 [E(N_p) E^2(N_{ph}) + Var(N_{ph}) E^2(N_p) + E(N_p) Var(N_{ph})] + Var(n_{PA}) \\ &= k_{PA}^2 T^2 [E(N_p) E^2(N_{ph}) + (E^2(N_p) + E(N_p)) \alpha^2 E^2(N_{ph})] + Var(n_{PA}) \end{aligned}. \tag{2.17}$$

When $E(N_p) \gg \alpha^{-2}$, we have

$$\begin{aligned} Var(A_{PA}) &\approx k_{PA}^2 E^2(N_p)\alpha^2 T^2 E^2(N_{ph}) + Var(n_{PA}) \\ &= \alpha^2 E^2(A_{PA}) + Var(n_{PA}) \end{aligned} . \tag{2.18}$$

The ratio between the mean squared and the variance of A_{PA} is the power-based signal-to-noise ratio (SNR):

$$\begin{aligned} SNR_{PA} &= \frac{E^2(A_{PA})}{Var(A_{PA})} \\ &= \frac{(k_{PA}E(N_p)TE(N_{ph}))^2}{k_{PA}^2 T^2[E(N_p)E^2(N_{ph}) + (E^2(N_p) + E(N_p))\alpha^2 E^2(N_{ph})] + Var(n_{PA})} \end{aligned} . \tag{2.19}$$

Defining $SNR_{th} = \frac{E^2(A_{PA})}{Var(n_{PA})}$, and substituting it into Equation 2.19, we have

$$\begin{aligned} \frac{1}{SNR_{PA}} &= \frac{1}{E(N_p)} + (1 + \frac{1}{E(N_p)})\alpha^2 + \frac{1}{SNR_{th}} \\ &= (1+\alpha^2)\frac{1}{E(N_p)} + \frac{1}{SNR_{th}} + \alpha^2 \end{aligned} . \tag{2.20}$$

Since $\alpha^2 \ll 1$, we get

$$\frac{1}{SNR_{PA}} \approx \frac{1}{E(N_p)} + \frac{1}{SNR_{th}} + \alpha^2 . \tag{2.21}$$

Equation 2.21 can be discussed in two different cases. In case 1, when particles are dense enough so that $E(N_p) \gg \alpha^{-2}$, we have

$$\frac{1}{SNR_{PA}} \approx \frac{1}{SNR_{th}} + \alpha^2 . \tag{2.22}$$

SNR_{PA} approaches α^{-2} when SNR_{th} increases. In case 2, when particles are sparse enough so that $E(N_p) \ll \alpha^{-2}$, we have

$$\frac{1}{SNR_{PA}} \approx \frac{1}{E(N_p)} + \frac{1}{SNR_{th}}. \tag{2.23}$$

SNR_{PA} approaches $E(N_p)$ when SNR_{th} increases. Using Equation 2.23 or more generally Equation 2.21, one can measure the expected value of the absolute particle count. In addition, if $E(N_p) \ll SNR_{th}$, Equation. 2.23 reduces to

$$SNR_{PA} \approx E(N_p). \tag{2.24}$$

Thus, the measurement outcome is independent of the laser fluence. Although our model is derived for static particle suspension, it is also valid for flowing particles, because the temporal statistics of particle count fluctuations in a static medium are equivalent to the spatial statistics of the particle count fluctuations in a flowing medium.

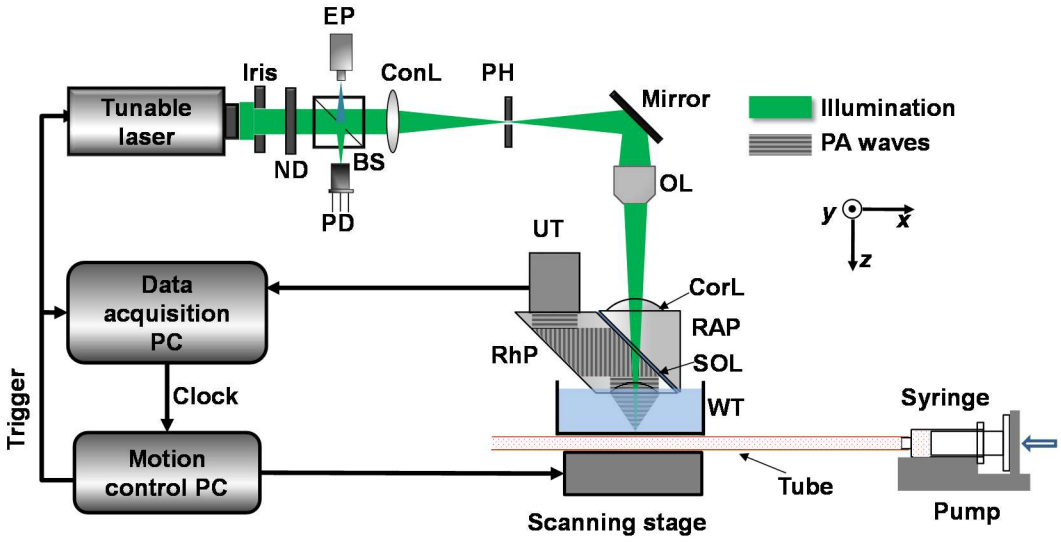

Figure 2.13 OR-PAM schematic. BS, beam splitter; ConL, condenser lens; CorL, correction lens; EP, eyepiece; ND, neutral density filter; OL, objective lens; PD, photodiode; PH, pinhole; RAP, right-angle prism; RhP, rhomboid prism; SOL, silicone oil layer; UT, ultrasonic transducer; WT, water tank.

We validated this idea using our optical-resolution PAM (OR-PAM) system shown in Figure 2.13. A tunable dye laser (CBR-D, Sirah, GmbH.), pumped by a Nd:YLF laser (INNOSAB, Edgewave,

GmbH.) at a 1 kHz pulse repetition rate, provides nanosecond laser pulses. The laser beam is filtered by a 50-μm-diameter pinhole and focused into the sample by a microscope objective lens (numerical aperture is 0.1). An acoustic-optical beam combiner, composed by two prisms sandwiching a layer of silicone oil, provides the acoustic-optical coaxial alignment. Acoustic detection is achieved with an ultrasonic transducer (V214-BC, Panametrics-NDT, Inc.) and a spherically focused acoustic lens, which is placed confocally with the optical objective lens. The detected PA signal is then amplified, digitized, and stored. Unlike confocal and two-photon microscopy, depth scanning is not needed in OR-PAM for volumetric imaging. A three-dimensional image is obtained by raster scanning the sample and piecing together the depth-resolved one-dimensional images (A-lines). So far, this OR-PAM system has achieved a lateral resolution of ~5 μm and an axial resolution of ~15 μm with an imaging depth of ~1 mm. Thus, the detection volume is about 500 μm^3 based on 1/e excitation beam width. In all experiments, plastic tubing with inner diameter of 300 μm was used to flow the liquid sample. A fast flow speed of 9 mm/s was applied to the fluid in the tubing to avoid potential heat aggregation or photobleaching, and to make sure the multiple PA signals were completely independent.

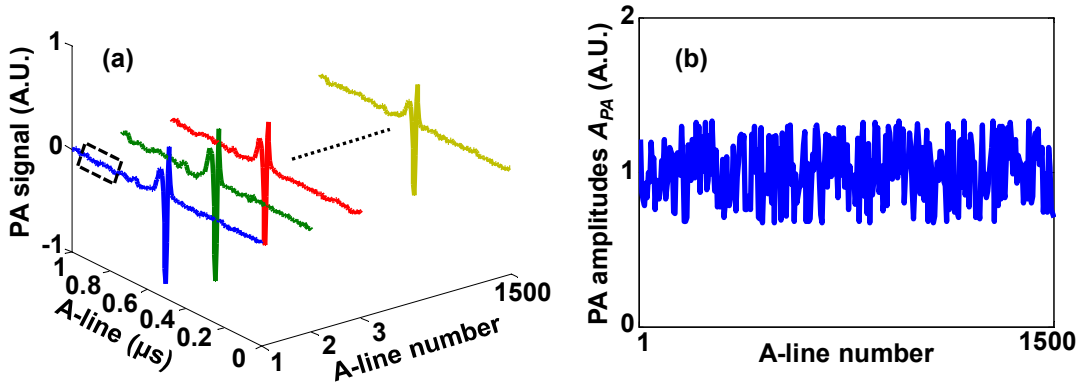

Figure 2.14 Representative PA signals (a) and PA amplitudes (b) of multiple A-lines with the same incident laser energy for each particle count.

To calculate $Var(A_{PA})$ and $E(A_{PA})$, for each particle count, we measured 1500 A-lines with the same incident laser energy. Representative A-lines and corresponding PA amplitudes are shown in Figures 2.14(a) and (b), respectively. Thus, $Var(A_{PA})$ and $E(A_{PA})$ can be obtained by calculating the variance and mean of the PA amplitudes. The background of each A-line inside the dashed box in Figure 2.14(a) was used to calculate the electronic thermal noise n_{PA}. Then we tuned the neutral density filter, shown in Figure 2.13, to change the incident laser energy. Thus, different SNR_{PA} and SNR_{th} could be obtained. Meanwhile, for each PA A-line, we monitored the incident energy by using a PD. Similarly, we could also calculate $Var(A_{PD})$ and $E(A_{PD})$ after 1500 measurements. By selecting PA A-lines with corresponding $E(A_{PD})$ only in a predetermined range, the photon count fluctuation α can be controlled. If $E(N_p) \ll \alpha^{-2}$, the absolute particle count can be quantified based on Equation 2.23 or Equation 2.24.

Lysed bovine blood was used for the experiment with large particle counts. It is estimated that there are about one billion hemoglobin molecules in the detection volume,[26] which satisfies the condition that $E(N_p)$ is much larger than α^{-2} for Equation 2.22. For small particle counts, defibrinated whole bovine blood was used instead for the experiment. In whole blood, RBCs, instead of hemoglobin molecules, constitute the particles moving in and out of the detection volume. Since there are only a few RBCs in the detection volume, $E(N_p)$ will be much smaller than α^{-2}, satisfying the condition for Equaiton 2.23.

To demonstrate quantitative particle count measurement, we prepared samples with different particle concentrations. Since we require that particle count fluctuation be dominant in the PA signal fluctuation, two different sizes of red dyed microspheres were used to make the samples: a

0.5 μm diameter particle with a stock concentration of ~3.64×10^{11} particles per milliliter (2.5% w/w), and a 1 μm diameter particle with a stock concentration of ~4.55×10^{10} particles per milliliter (2.5% w/w). The smaller particle stock solution was diluted by 2 and 4 times, while the larger particle stock solution was diluted to 8 and 16 times the stock concentration of the smaller particle solution.

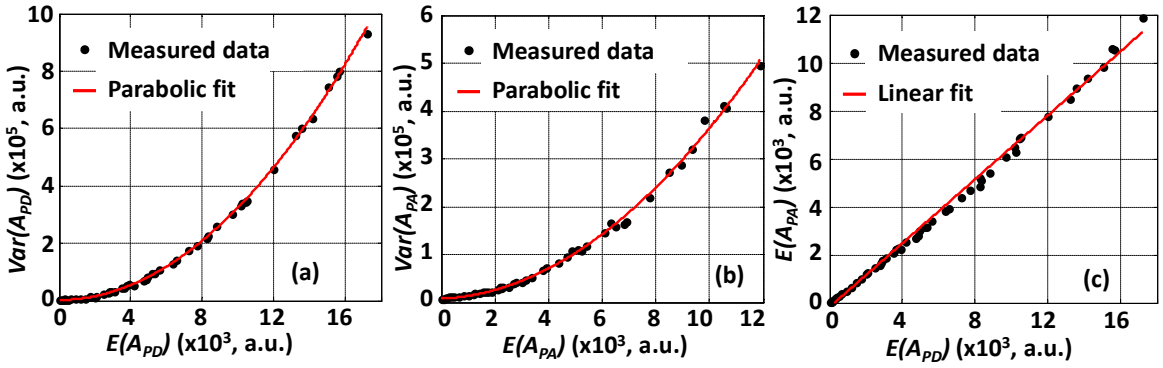

Figure 2.15 Relationships between (a) $Var(A_{PD})$ and $E(A_{PD})$, (b) $Var(A_{PA})$ and $E(A_{PA})$, (c) $E(A_{PA})$ and $E(A_{PD})$ as estimated from the experimental data. Fitting equation for (a): $Var(A_{PD}) = \alpha^2 \times E^2(A_{PD}) + 2631$, where $\alpha = 0.0567$, coefficient of determination $R^2 = 0.9994$. Fitting equation for (b): $Var(A_{PA}) = \alpha^2 \times E^2(A_{PA}) + 7508$, where $\alpha = 0.0576$, $R^2 = 0.9974$. Fitting equation for (c): $E(A_{PA}) = 0.6656 \times E(A_{PD}) - 190.7$, $R^2 = 0.9964$. (a) and (b) show that when the particle count is sufficiently large, both $Var(A_{PA})$ and $Var(A_{PD})$ follow a parabolic relationship with $E(A_{PA})$ and $E(A_{PD})$, respectively. The coefficients α for PD and PA are almost identical, both due to the photon count fluctuation. (c) shows a good linearity between $E(A_{PA})$ and $E(A_{PD})$.

We used defibrinated bovine blood in two experiments: an *ex vivo* experiment and an *in vivo* mimicking experiment. For the *ex vivo* experiment, defibrinated bovine blood with four different concentrations was prepared. The original undiluted defibrinated bovine blood (150 g/L) was serially diluted to 3/4, 1/2, and 1/4 of the original concentration. Since there were too few RBCs in the original resolution voxel of OR-PAM, we increased the detection volume to 1.2×10^{-5} mm^3 by defocusing the light beam. For the simulated *in vivo* experiment, the original undiluted

defibrinated bovine blood (150 g/L) was serially diluted to 1/2 and 1/4 of the original concentration.

Results Based on Equations 2.13 and 2.18, $Var(A_{PD})$ and $Var(A_{PA})$ parabolically depend on $E(A_{PD})$ and $E(A_{PA})$, respectively. In addition, $E(A_{PA})$ should be proportional to $E(A_{PD})$. In the experiment using lysed bovine blood, the result shows a clear parabolic relationship between $Var(A_{PD})$ and $E(A_{PD})$ [Figure 2.15(a)]. The photon count fluctuation coefficient α was fitted to be 5.67%, close to the laser specification. The similar result between $Var(A_{PA})$ and $E(A_{PA})$ is shown in Figure 2.15(b). The coefficient α was fitted to be 5.76%, very close to the one for PD. In addition, Figure 2.15(c) shows that there is a good linearity between $E(A_{PA})$ and $E(A_{PD})$.

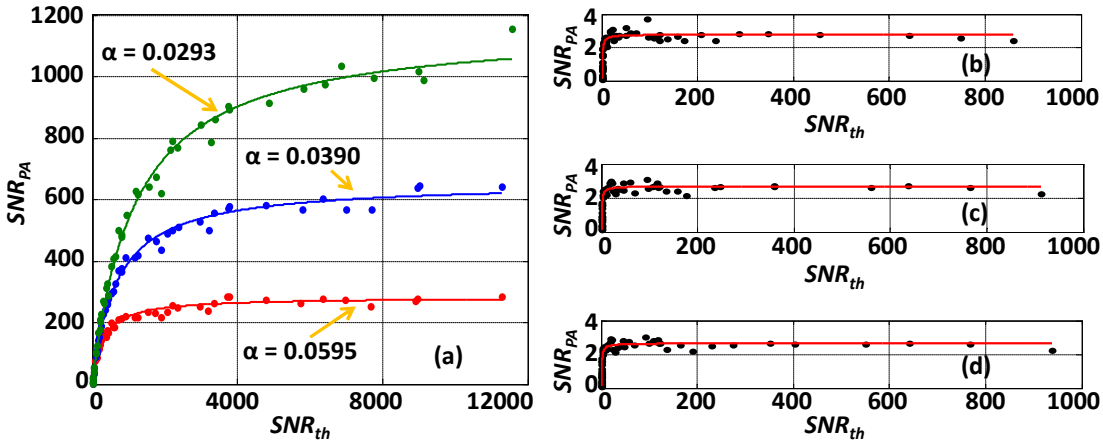

Figure 2.16 Measurements for different photon count fluctuation coefficients. (a) For larger particle counts, the SNR_{PA} at sufficiently high SNR_{th} depends only on photon count fluctuation. (b)-(d) If the particle count is small, the SNR_{PA} at sufficiently high SNR_{th} depends primarily on the particle count. (b) α = 0.0066. (c) α = 0.0284. (d) α = 0.0587. The dots are the measurement data, and the solid curves are the fitted results based on Equation 2.21.

As mentioned above, we can regroup the laser pulses based on the photodiode readings. By doing this, the laser intensity fluctuation coefficient α can be artificially controlled to a predetermined

value. Figure 2.16(a) shows that with large particle counts, SNR_{PA} is dominated by the light fluctuations when SNR_{th} increases, consistent with Equation 2.22. Here the neutral density filter was adjusted to change the laser fluence and thus to change the SNR_{th}. On the other hand, when the particle counts are small in the detection volume, the measurement results with high SNR_{th} only rely on the particle counts [Figures. 2.16(b) to (d)], consistent with Equation 2.23. Although the photon count fluctuation coefficients are varied, the measurement results stay the same. Thus, the fluence-independent measurement is achieved with the conditions of high SNR_{th} and small particle counts.

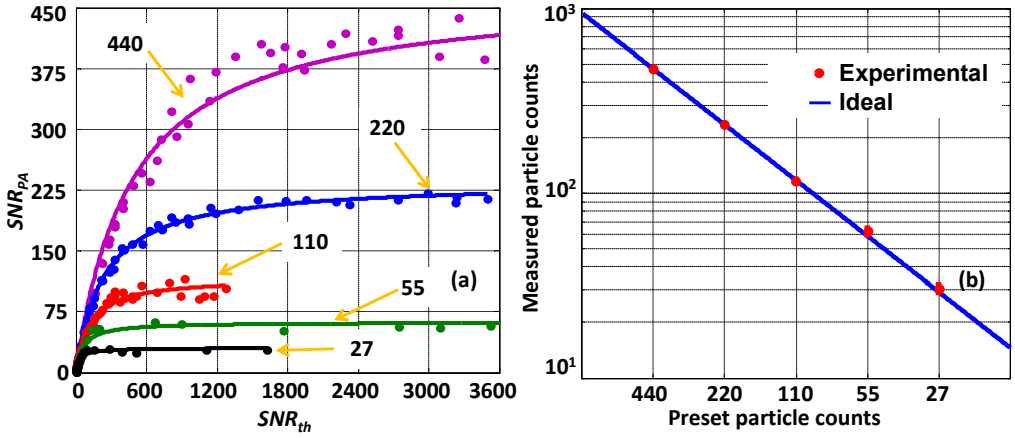

Figure 2.17 Quantitatively measuring particle concentration from different samples with the same light fluctuation. (a) The preset particle counts are 440 (purple), 220 (blue), 110 (red), 55 (green), and 27 (black). Solid lines: theoretical fitting based on Equation 2.23. (b) Measured particle count versus the preset value.

Next, we applied our method to quantitatively measure five different particle concentration samples. Figure 2.17(a) shows measured results with five different preset particle counts of 440, 220, 110, 55, and 27 in the detection volume. The experimental results agree well with the preset values. In addition, we observed that the measured particle count does not change with the laser

fluence any longer when the SNR_{th} is high enough. The fitted coefficient $E(N_p)$ in the model was used to quantify the absolute particle count for each sample. As shown in Figure 2.17(b), the experimental results agree well with the preset particle counts in the detection volume.

We also measured RBCs to validate the feasibility of our method in biological applications. Figure 2.18(a) illustrates the measured results with the fitting curve for four different preset RBC counts of 400, 300, 200, and 100 in the detection volume. We used the fitted coefficient $E(N_p)$ to represent the counts of RBCs and compared with the corresponding preset RBC counts [Figure 2.18(b)]. The results demonstrate that our method is fluence-independent and can be used to quantitatively measure biological samples.

For *in vivo* application, additional signal fluctuation mainly comes from the perturbation of laser fluence by micro-flows in the light path. To mimic the *in vivo* situation while maintaining the flexibility of varying the RBC concentration, we covered targets made of black tape and bovine-blood-filled tubing with a living mouse ear, as shown in Figures 2.19 (a-c).

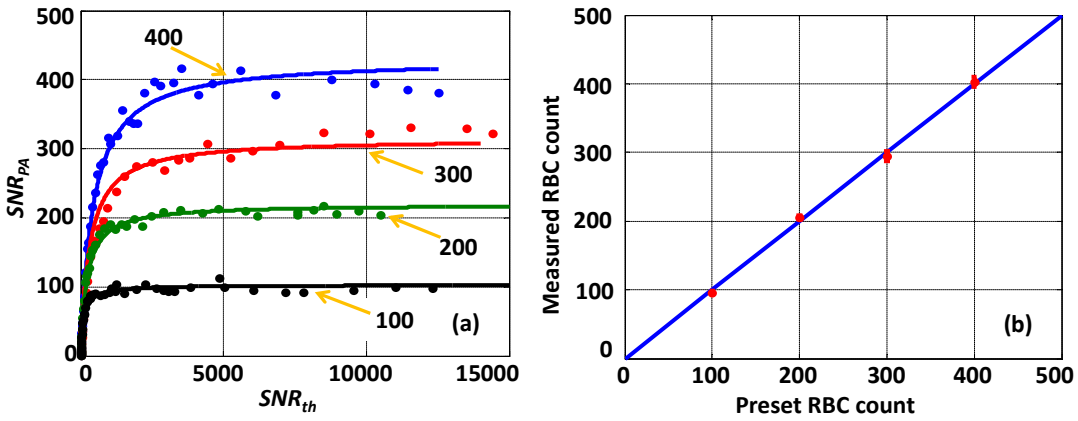

Figure 2.18 Measured RBC counts under the same light fluctuation. (a) The preset particle counts are 400 (blue), 300 (red), 200 (green), and 100 (black). Solid lines: theoretical fitting based on Equation 2.23. (b) Measured particle count versus the preset value.

We first measured the signal fluctuations from black tape, which did not show Brownian motion. As shown in Figure 2.19(d), measurements were made at 40 random spots on the black tape. For all the spots, the PA signal fluctuations were around 2%. As described before, the power-based signal-to-noise ratio (SNR_{PA}) was used to denote the measured particle counts. Since a 2% fluctuation corresponds to an SNR_{PA} of 4×10^{-4}, it is negligible. The experimental results show that the *in vivo* PA signal fluctuation due to other sources rather than Brownian motion is insignificant.

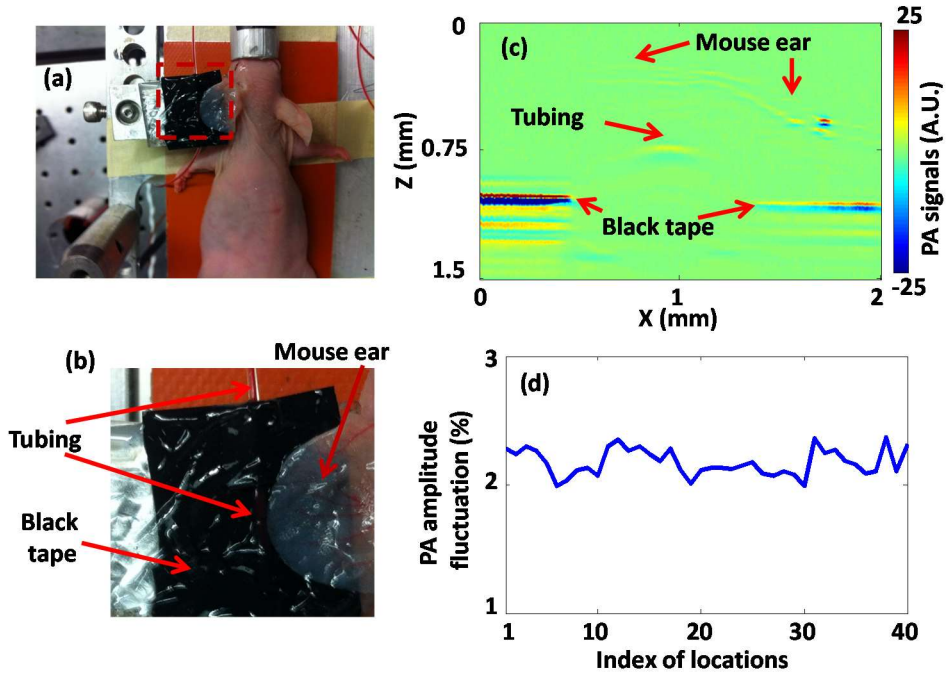

Figure 2.19 Measurement of RBC counts in tubing covered by a living mouse ear. (a) Photo of the experimental setup. (b) Close-up of the region within the red dashed box in (a), showing the blood-filled tubing and black-tape targets covered by the living mouse ear. (c) A typical cross-sectional PA image showing that the tubing and part of the black tape were covered by the mouse ear. (d) Measurement of PA amplitude fluctuation from black tape at 40 random spots covered by the mouse ear.

Furthermore, we measured RBC counts in the same setup. Figure 2.20(a) illustrates the measured results, with fitting curves for three different preset RBC counts of 1080, 540, and 270 in the

detection volume. We used the fitted coefficient $E(N_p)$ to represent the RBC counts. As shown in Figure 2.20(b), the experimental results agree with the preset RBC counts. The result shows that our method can be used to measure RBC counts in an *in vivo* mimicking situation using OR-PAM.

To show the potential for actual *in vivo* applications of our method, we performed two more demonstrations, which correspond to anemia caused by blood loss and by RBC aggregation, respectively. In each *in vivo* experiment on RBC count, we maintained the laser fluence constant (see the *Discussion* section). In the first demonstration, saline was injected into mouse tail vein to mimic blood loss (blood dilution), as shown in Figure 2.21(a). The same vein was monitored to quantify the RBC count changes. Figure 2.21(b) shows a PA image of the vein, where the black cross denotes the monitoring spot. We slowly injected ~0.03 mL saline into the tail vein during a 3 minute window. As shown in Figure 2.21(c-d), the measured RBC count was reduced by injected saline. As soon as we stopped injection, the RBC count quickly returned to its normal value.

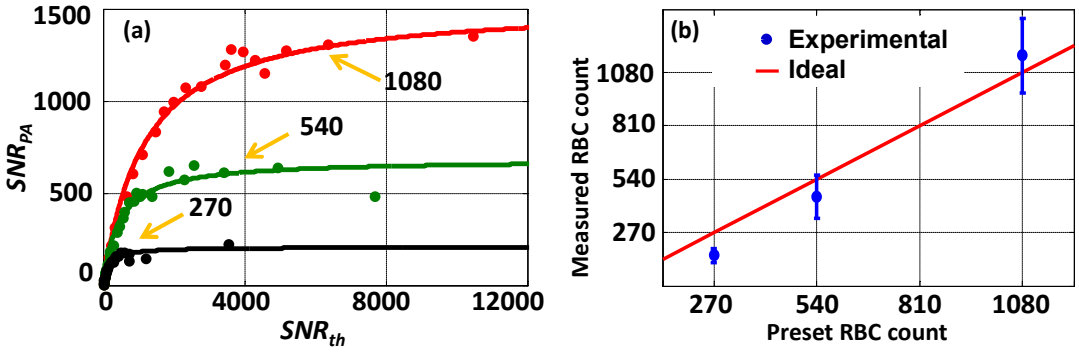

Figure 2.20 RBC count measurement with the blood-filled tubing covered by a mouse ear. (a) The preset RBC counts in the voxel were 1080 (red), 540 (green), and 270 (black). (b) Measured versus preset RBC counts.

In the other demonstration, to induce RBC aggregation, we used ~0.3 mL 3% dextran-70 solution to mix with 3 mL original RBC solution. The diluted original and aggregated RBC solutions were

imaged *ex vivo* by a commercial microscope, as shown in Figure 2.22. The results show that we can induce RBC aggregation successfully *ex vivo* and probably *in vivo*.

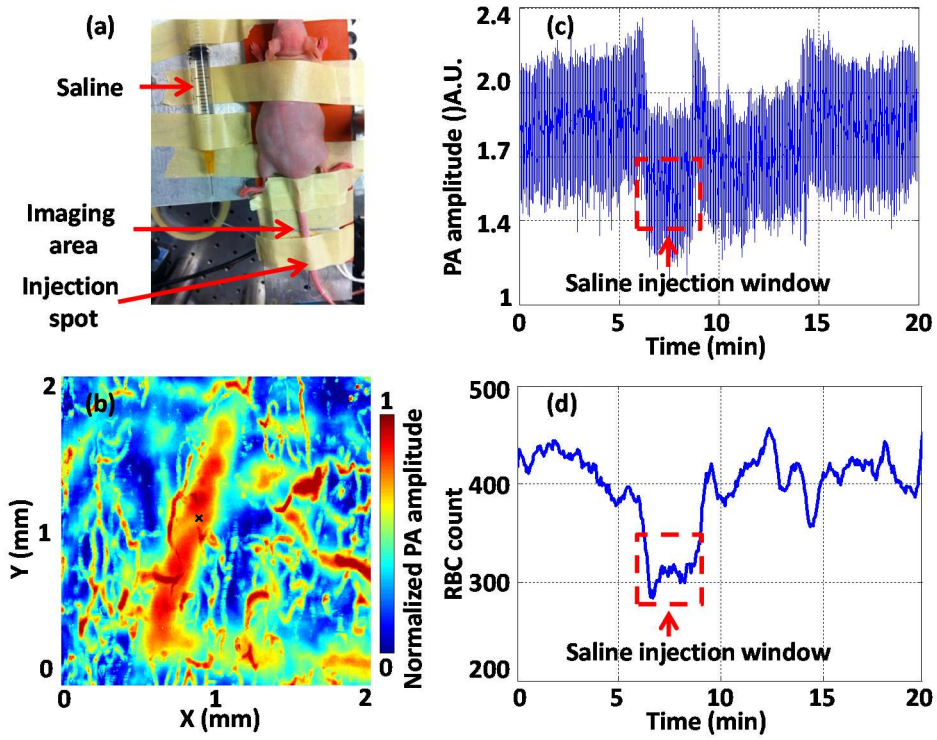

Figure 2.21 *In vivo* RBC count changes in a mouse tail vein when injecting saline. (a) Animal setup in the experiment. The imaged area was downstream of the saline injection spot. (b) PA MAP image of part of the tail *in vivo*. The large vessel in the middle is the mouse tail vein where we injected the saline. The black cross denotes the monitoring spot. (c) Time course of PA amplitude. The red dashed box highlights a clear decrease in the PA signal mean value. (d) RBC counts measured by our method before, during, and after saline was injected into the tail vein.

Then we performed an *in vivo* experiment to observe RBC aggregation. The same dextran-70 solution was injected into a mouse through the tail vein, and the mouse ear was used to monitor the RBC aggregation, as shown in Figure 2.23(a). Figure 2.23(b) shows the PA image of the mouse ear, where the red cross denotes the RBC monitoring spot. As shown in Figure 2.23(c-d), an increase of PA signal fluctuation and corresponding RBC count decrease were observed about 50 minutes after the dextran-70 solution injection. Based on the results of our *ex vivo* experiment, we

think that this decrease in RBC count was from RBC aggregation, induced by the mixing of dextran-70 solution with blood.

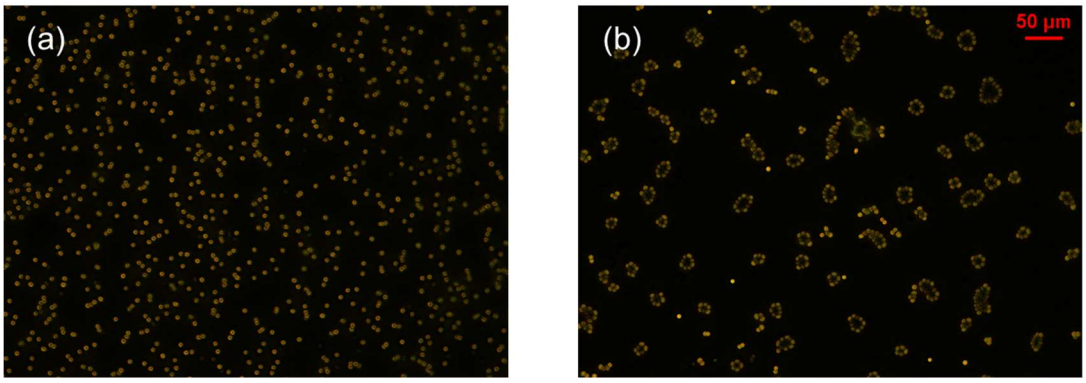

Figure 2.22 RBC aggregation induced by 3% Dextran-70 solution. The concentration of RBCs was the same in the two images. (a) Original and (b) aggregated RBCs imaged by a commercial microscope.

Discussion Both the theoretical model and experimental study showed that our method is applicable when the particle count in the detection volume is sufficiently small such that the particle Brownian motion dominates the PA signal fluctuation. If we can control the photon count fluctuation coefficient within 1%, the maximum count of particles that we can measure is on the order of 1000 ($\ll 1/\alpha^2$). By contrast, the minimum measurable count of particles is limited by SNR_{th}. If the count of particles in the detection volume is too small, noise reduces the measuring accuracy significantly. Either particles with larger absorption cross-sections or greater detection volumes can reduce the minimum. Based on our experimental results (Figures 2.16(b)-(d)), we conclude that our method can measure as few as three RBCs in the detection volume.

As shown in Figure 2.17, our measured particle counts are slightly larger than the preset absolute counts estimated based on the detection volume of 500 μm. This is most likely due to the inaccurate estimation of the detection volume. We calculated the detection volume based on the 1/e detection sensitivity field. However, particles not in this volume can still generate PA signals, which will

contribute to the total PA signals. If we take those particles into account, the actual detection volume becomes greater.

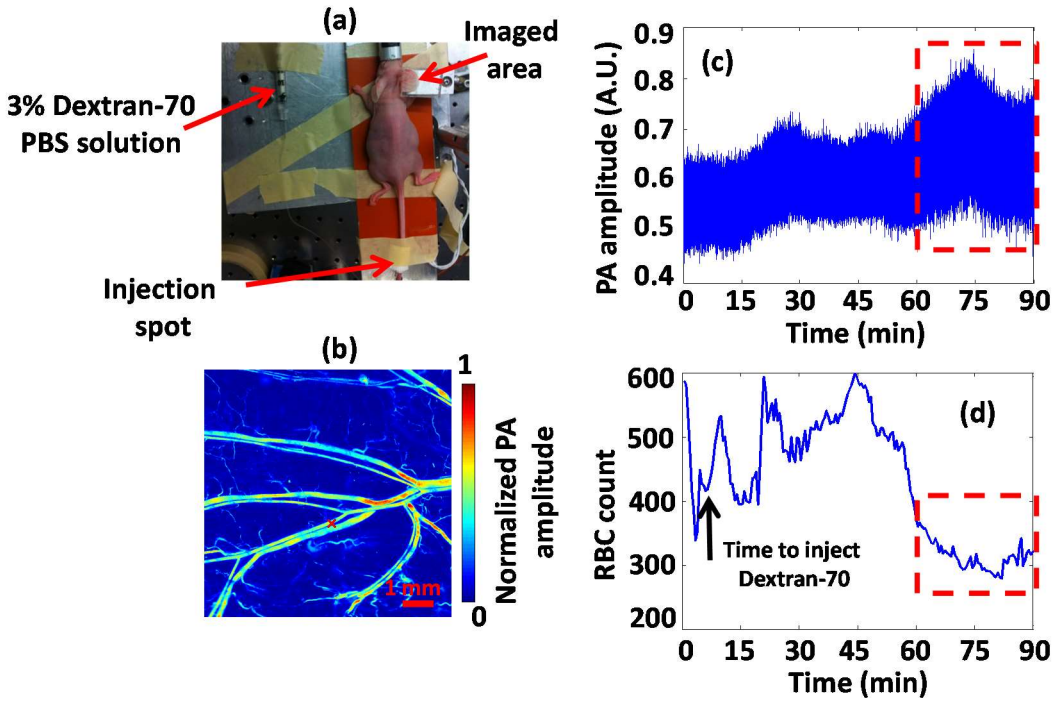

Figure 2.23 RBC aggregation measured *in vivo*. (a) Animal mounting in the experiment. Dextran-70 solution was injected into the mouse through the tail vein. The mouse ear was imaged and monitored over time. (b) PA MAP image of the mouse ear. The red cross denotes where we monitored the RBC count. (c) Time course of PA amplitude. The red dashed box highlights a clear increase in the PA signal fluctuation. (d) Time course of RBC count measured by our method. The selected red dashed box window highlights a decrease in RBC count.

In addition, as shown in Figures. 2.16(a), 2.17(a), and 2.18(a), when SNR_{th} becomes high enough, the measured particle counts are independent of the SNR_{th} and laser fluence. Although we examined the complete trend in this study with varying SNR_{th}, a measurement with a single, high enough SNR_{th} is sufficient to measure the fluence-independent particle counts in the detection volume, as we have done in the *in vivo* experiment.

In our experiments, we chose a flowing medium for the following two reasons. First, we focused on measuring counts of RBCs, which usually flow constantly *in vivo*. Second, using a flowing medium can avoid potential heat accumulation and photobleaching, which, however, can be mitigated by decreasing the pulse repetition rate. For example, the heat diffusion time is about 0.2 ms in our experiment (characteristic dimension: 5 μm; thermal diffusivity: 1.3×10^{-3} cm^2/s). Thus, a laser repetition rate of 1 kHz causes minimal heat accumulation, which is further reduced by blood perfusion.

Finally, we may be able to apply our method in deep tissue imaging modalities such as acoustic resolution PAM and PA computed tomography where fluence compensation is even more challenging. However, compared with OR-PAM, their greater detection volume may require even lower particle concentrations. Although it may be difficult to detect absolute RBC counts, we can use our method to monitor the absolute counts of other cells in blood, such as intact or labeled white blood cells [72], which are much sparser in the blood stream.

2.4 Conclusions

First, we applied optical clearing to PAM. Our results show that both the penetration depth and lateral resolution of PA imaging can be enhanced by TOC. For backscattering-based optical imaging modalities such as optical coherence tomography, optical clearing can provide deeper penetration depth as well. However, it may destroy some of the intrinsic scattering contrasts that these modalities rely on, which can result in potential information loss. By contrast, PA imaging is based on optical absorption with 100% sensitivity. Since the optical absorption cross section of the substance (e.g., hemoglobin) remains largely intact in the optical clearing procedure, information loss is avoided. Not only can PA imaging benefit from optical clearing, it can also be

used to study the physiological effects induced by optical clearing. With enhanced penetration depth and resolution, PAM will become more valuable for structural, molecular, functional, and metabolic imaging.

Second, we used PAM for quantitative mapping of bilirubin distribution. The RMSEP of concentration was quantified to be 0.52 mg/dL for pure bilirubin samples, 1.04 mg/dL for bilirubin-blood mixtures with 75% sO_2, and 0.83 mg/dL for bilirubin-blood mixtures with 100% sO_2, respectively. The bilirubin distribution, both in the pure bilirubin samples and in the blood-mixed samples, was imaged by multi-wavelength PAM. Finally, imaging bilirubin with underlaid mouse skins illustrated that at least a 400 μm penetration depth can be achieved by PAM without noticeable degradation in accuracy. Therefore, our method shows promise to quantitatively image bilirubin *in vivo* for further clinical applications, such as the diagnosis of jaundice.

Third, we used PAM for fluence-independent particle count measurement by statistically analyzing PA signals. This method has been experimentally verified by using different kinds of samples, including RBCs. We also demonstrated the feasibility of our method in the *in vivo* experiment. Therefore, our method shows promise for quantitatively measuring biological samples *in vivo,* which could be used for red blood cell aggregation monitoring.

Chapter 3 Pain Syndrome Study with Photoacoustic Tomography in Patients

3.1 Microcirculatory Changes Identified by Photoacoustic Microscopy in Patients with Complex Regional Pain Syndrome Type I (CRPS-1) after Stellate Ganglion Blocks

Background Complex regional pain syndrome (CRPS) is a pain disorder characterized by severe and disproportionate pain, autonomic changes such as abnormal regulation of blood flow and sweating, edema of skin and subcutaneous tissues, motor disorders, and dystrophic changes. The pathophysiological mechanism of CRPS is still poorly understood, although our knowledge of this syndrome has increased significantly [73-75]. Multiple factors, including vascular and microcirculatory dysfunction, neurogenic inflammation [76], alteration in sympathetic and catecholaminergic function, as well as peripheral and central sensitization, may all play important roles in the pathogenesis of this disabling syndrome [77]. However, microcirculatory parameters, including rate and volume of blood flow and tissue oxygen saturation (sO_2), are of considerable interest for potentially diagnosing CRPS and monitoring its progress, due to the connection between the microvascular blood supply and the development of neuropathic pain [78].

There is increasing evidence to show that inflammatory processes and immune reactions are involved in the pathophysiology of CRPS [79]. In a systemic review and meta-analysis study, Parkitny et al [76], concluded that CRPS is associated with proinflammatory states in the blood, blister fluids, and cerebrospinal fluid (CSF). The CRPS-related inflammation may change the sympathetic tone of blood vessels and therefore affect blood supply and tissue oxygenation. The acute and chronic phases of CRPS demonstrate different inflammatory features in both clinical

manifestations and inflammatory profiles. The measurement of microcirculatory parameters, such as blood flow rate, blood volume, and blood oxygen saturation (sO_2) can be used to potentially diagnose the presence of CRPS, to indicate the activity of the disease, and to monitor the effectiveness of the therapeutic intervention.

In pain studies, traditional techniques for detecting microcirculatory parameters include functional magnetic resonance imaging (fMRI) and positron emission tomography (PET) [80]. However, both have limitations: fMRI makes indirect measurements by the blood-oxygenation-level dependent (BOLD) method [81, 82] or makes direct flow measurements with low sensitivity by the arterial spin labeling (ASL) method; PET has to use radioactive tracers to measure blood flow directly [83]. To overcome these limitations, optical methods provide alternative ways to make direct, sensitive, non-invasive, and non-ionizing measurements of blood flow and sO_2 in pain studies [84-87]. Optical spectroscopic methods, such as near-infrared spectroscopy (NIRS) [84] and micro-lightguide spectrophotometry [85], can provide non-invasive measurement of average blood flow and sO_2, but with poor spatial resolution. Optical coherence tomography and optical Doppler imaging provide blood vasculature anatomy imaging with high spatial resolution and sensitive measurements of flow speed, but lack high sensitivity for measuring sO_2, because their imaging contrasts are based on optical scattering.

The diagnosis of CRPS is based on clinical manifestations, and there are limited laboratory tests or image studies to verify the diagnosis. With its high spatial resolution and label-free nature, PAM is potentially an ideal tool for monitoring and diagnosing CRPS by imaging peripheral blood perfusion [88]. In this work, we performed a series of experiments to show the feasibility of this new imaging tool.

Methods In this prospective observational study, we screened patients with a possible diagnosis of CRPS -1 who were referred to the Pain Management Center of Washington University in St. Louis between January 2011 and December 2011. Nine adult patients (28-69 years old, 6 female, 3 male) with CRPS-1 were recruited. Patients with pain in only one upper extremity were selected to participate in the study. One patient withdrew from the study. Patients were considered to be candidates for the study if they were diagnosed with CRPS-1 by using the proposed new diagnostic criteria of the International Association for the Study of Pain (IASP) [89]. All patients signed consents to be involved in the study. All human research procedures were carried out in conformity with the protocol approved by the Institutional Review Board at Washington University in St. Louis.

For all the patients, symptoms and signs of CRPS were present for less than one year. Average pain level was 5 or higher on a numerical rating score (NRS) scale of 0–10 (with 0 being no pain and 10 being the worst imaginable pain). Exclusion criteria were pregnancy, coagulopathy, fever, general infection or local infection at the block puncture site, substance abuse, peripheral neuropathy or any other diseases that may account for signs and symptoms mimicking CRPS.

Benefits and risks of stellate ganglion block (SGB) were explained to the patients in detail. A written consent was obtained for the procedure. ASA standard monitors were applied during the procedure and post procedure in the recovery room. The skin temperature of the hands was measured before and 10 mins after the procedure. SGB on the cervical sympathetic chain was performed at the C7 vertebral level using the standard anterior paratracheal approach under fluoroscopic guidance. The patient was placed in the supine position with the head slightly hyperextended. The needle entry point was fluroscopically identified by anterior-posterior view at the junction of the C7 vertebral body and transverse process on the side of the diseased limb. Sterile

technique was used throughout the entire procedure. After sterilization and preparation, 1-3 ml of 1% lidocaine was used for skin infiltration at needle entry point. Then a 10-mm, 25-gauge nerve block needle was inserted and advanced to the junction of the transverse process and the corresponding C7 vertebral body. Bony contact was made. The appropriate needle positioning was confirmed by anterior-posterior and lateral views. Once the needle was confirmed in the correct position fluoroscopically, aspiration was made for negative blood and other body fluids. Then a small amount (0.5–1 ml) of contrast dye was injected to visualize and prevent potential intravascular injection. After an adequate craniocaudal contrast dye spread from C5 to T1 was obtained, an injection of 10 ml of 0.25% bupivacaine with 1:200,000 epinephrine was given in 2 ml increments, with interval negative aspiration. The patient was observed in the recovery area for 15 mins after the procedure. 10 mins after SGB, skin temperature in the block side increased 1.1 ± 0.1°C. Meanwhile, pain level reduced by 2.5 ± 0.6 on discharge.

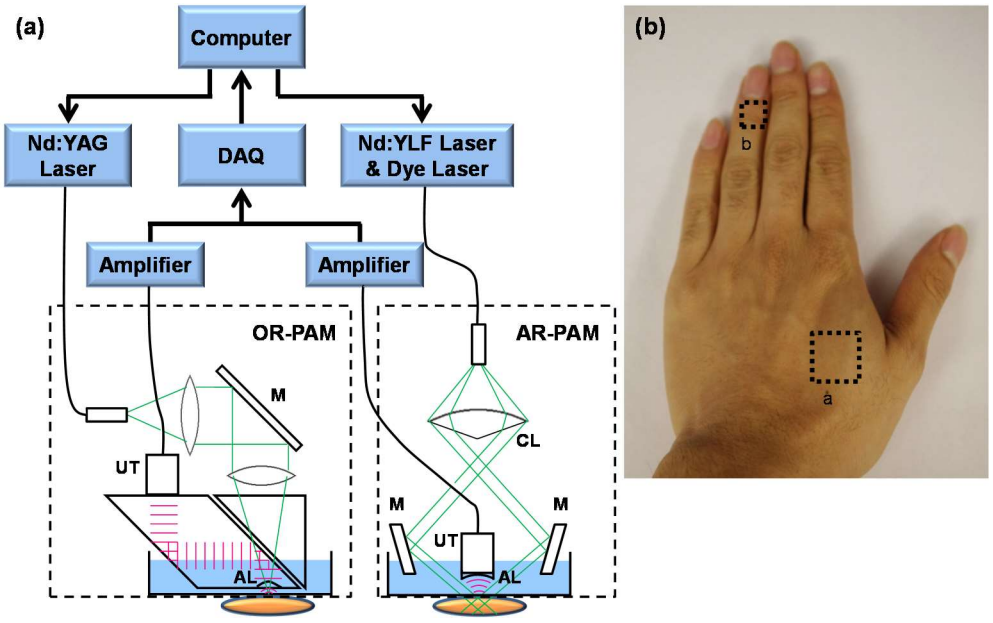

Figure 3.1 (a) Schematic of the OR-PAM and AR-PAM systems. AL: acoustic lens; CL: conical lens; DAQ: data acquisition system; M: mirror; UT: ultrasound transducer. (b) Photograph of the hand, showing the scanned regions. a: region scanned by AR-PAM; b: region scanned by OR-PAM.

The experimental paradigm consisted of two imaging sessions, with a SGB between the sessions. For each patient, the back of their hand and the cuticle of the same hand were imaged before SGB (baseline) and then after SGB. Two sites (Figure 3.1b) were chosen to image: superficial microvasculature at the cuticle and deeper and larger vessels at the back of the hand.

According to its light illumination mechanism, PAM can be classified into two categories: AR-PAM and OR-PAM. In AR-PAM, the light is weakly focused, and the lateral resolution is determined by the acoustic focusing of the ultrasonic transducer. In OR-PAM, the light is tightly focused, and thus the lateral resolution is determined by the optical focusing provided by the objective. The axial resolution of both AR- and OR-PAM is determined by the bandwidth of the transducer used in the system. Usually optical focusing is much tighter than acoustic focusing, and thus OR-PAM has a better lateral resolution than AR-PAM. However, since acoustic scattering is much weaker than optical scattering in soft tissue, AR-PAM can focus deeper than OR-PAM. To monitor hemodynamic changes with both high spatial resolution and deep penetration, both AR- and OR-PAM systems were used in this research. The schematics are shown in Figure 3.1(a). In the AR-PAM system, a donut-shaped illumination is formed when light passes through the conical lens. A 20-MHz ultrasonic transducer collects the PA signals. In the OR-PAM system, light illumination and acoustic collection are achieved by an ultrasound-optical beam combiner. A 50-MHz ultrasonic transducer detects the PA signals. Each laser pulse generates a one-dimensional depth-resolved image ("A-line") in both the AR- and OR-PAM systems. By two-dimensional raster-scanning of the entire area, a three-dimensional image can be acquired. For more accurate sO_2 calculation in both AR- and OR-PAM systems, a photodiode compensates for the local fluence fluctuation. A detailed system description can be found in our previous papers. The lateral resolutions of the AR- and OR-PAM systems are 80 μm and 3 μm, respectively. To measure sO_2,

light at two wavelengths, 570 nm and 578 nm, was used in both AR- and OR-PAM. The PA signal from both wavelengths can be described as

$$P(\lambda_1) = k \times (\varepsilon_{Hb}(\lambda_1) C_{Hb} + \varepsilon_{HbO_2}(\lambda_1) C_{HbO_2}) \tag{3.1}$$

$$P(\lambda_2) = k \times (\varepsilon_{Hb}(\lambda_2) C_{Hb} + \varepsilon_{HbO_2}(\lambda_2) C_{HbO_2}), \tag{3.2}$$

where P denotes PA signal amplitude, λ_1 and λ_2 denote the first and second wavelengths, k denotes a system dependent constant, ε denotes the molar extinction coefficient, Hb denotes deoxygenated hemoglobin, HbO_2 denotes the oxygenated hemoglobin, and C denotes the molar concentration. Based on Equations 3.1 and 3.2, we can solve for C_{Hb} and C_{HbO2}. In the end, sO_2 can be calculated as

$$sO_2 = \frac{C_{HbO_2}}{C_{HbO_2} + C_{Hb}}. \tag{3.3}$$

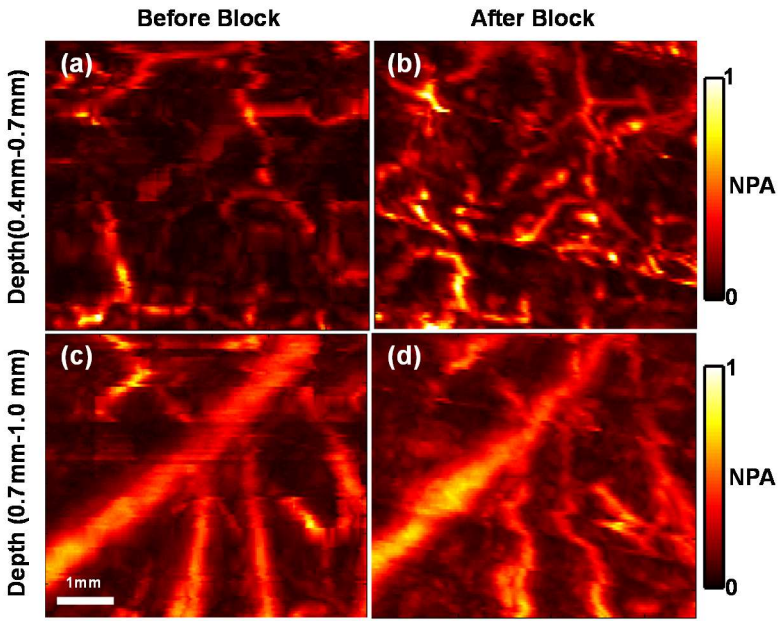

Figure 3.2 Maximum amplitude projection (MAP) images of vasculature in the back of one patient's hand by AR-PAM. MAP image in the depth range between 0.4 mm and 0.7 mm before block (a) and after block (b). MAP image in the depth range between 0.7 mm and 1 mm before block (c) and after block (d). NPA, normalized photoacoustic amplitude.

Results Typical AR- and OR-PAM hand images of patients are shown in Figures 3.2 and 3.3, respectively. For fair comparisons, the distance between the patient's hand and the ultrasonic transducer was adjusted to be the same before and after SGB for imaging. In AR-PAM, a ~6 mm by 6 mm field of view was scanned. The signals down to 1 mm deep were collected. Due to the high axial resolution of AR-PAM, we were able to differentiate signals from different depths. Maximum-amplitude-projection (MAP) images along the depth direction, with ranges of 0.4 mm-0.7 mm and 0.7 mm-1.0 mm, are shown in Figure 3.2. Two major differences can be easily seen: more blood vessels and stronger signals after the block. Because the local optical fluence fluctuation had been compensated for, the PA signal was mainly dependent on the absorption coefficient of the target. Thus, an increase in the PA signal indicates an increase in the local absorption coefficient, probably due to increased blood concentration or volume. Therefore, we suspect that there was increasing blood perfusion and blood vessel dilation after the block.

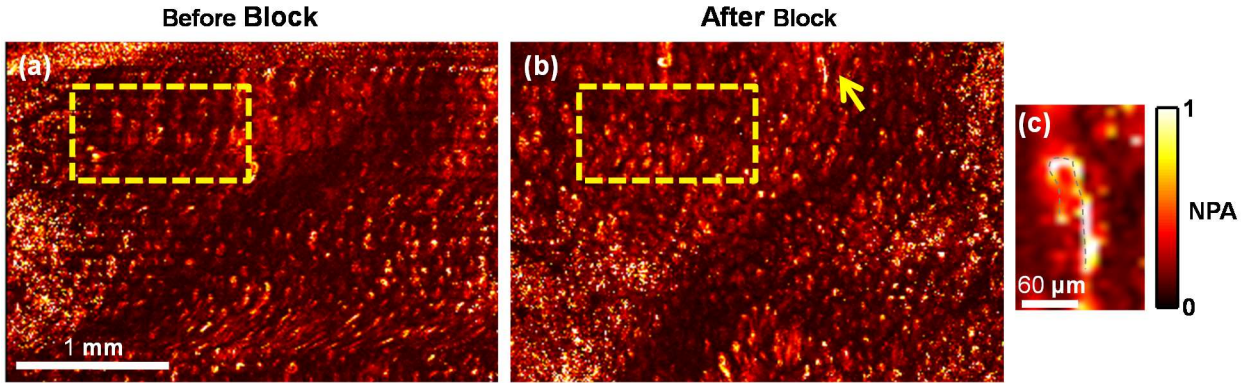

Figure 3.3 OR-PAM vasculature image of the fingertip of one patient. MAP of scanned region before block (a) and after block (b). The dashed box represents the region used for statistical analysis. (c) Close-up image of the capillary loop indicated by the arrow in (b).

Typical blood vessels in the finger cuticle imaged by OR-PAM are shown in Figure 3.3. As indicated in Figures 3.3(b) and (c), OR-PAM successfully imaged a single capillary loop, which

is the smallest vessel in human blood circulation. As shown in Figure 3.3(b), a stronger signal was found after the block, which is consistent with the results from AR-PAM.

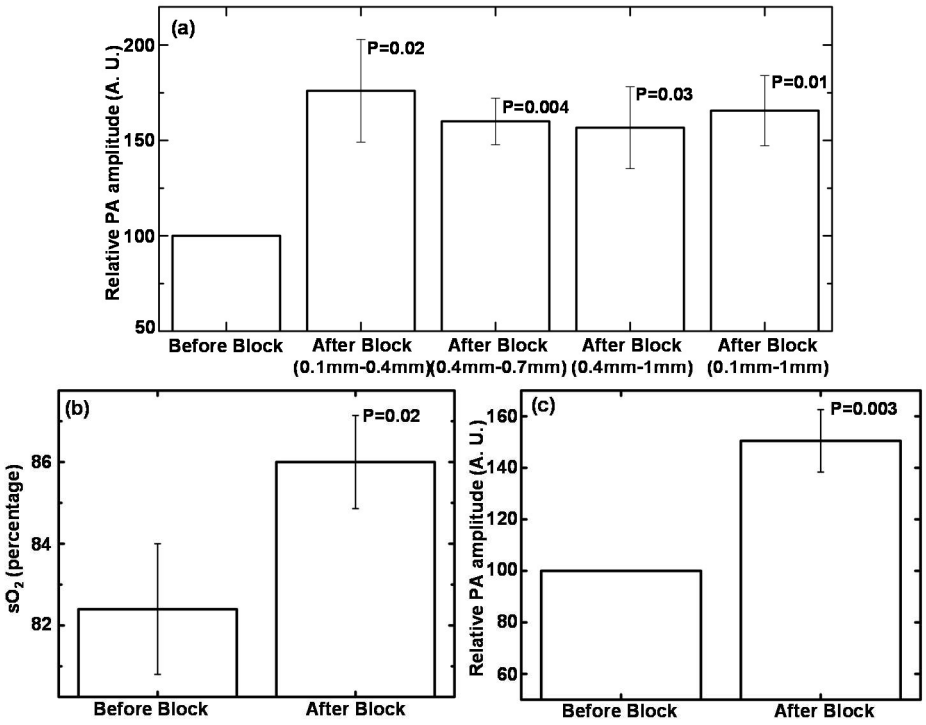

Figure 3.4 (a) Normalized photoacoustic (PA) signal measured by AR-PAM before and after block in different depth ranges. (b) Average sO_2 measured by AR-PAM before and after block. (c) Normalized PA signal measured by OR-PAM before and after block.

Statistical analysis of all the patient data are shown in Figure 3.4. Figure 3.4(a) shows the average increase in signal intensity at different depths after the block. On average, there was more than 50% signal increase in all depth ranges. In addition, the signal increased most within the 0.1 mm – 0.4 mm depth range, where the capillary bed is located. Similar results from OR-PAM can be found in Figure 3.4(c). According to the dual-wavelength measurement by AR-PAM, the average sO_2 increased ~4%.

Discussion CRPS-1 is a difficult clinical condition to diagnose and treat. Early diagnosis and management are necessary to prevent a long-standing or permanent disability. The diagnosis of CRPS-1 is primarily based on clinical observation and assessment of symptoms and signs, although a diagnostic algorithm has been recently proposed [90]. A unique pathophysiological mechanism for CRPS-I has not yet been established and therefore sensitive and specific laboratory diagnostic parameters are lacking, resulting in difficulties in making valid diagnosis and distinguishing CRPS from other extremity pain entities. Several diagnostic procedures, such as bone scintigraphy, plain radiographs, quantitative sensory testing, skin temperature measurements, and fMRI are used to support the diagnosis of CRPS. However, they require pathognomonic markers. For example, the recommended three phase bone scan demonstrated both cortical and cancellous osteopenia in CRPS patients and controls treated with casting [85]. Meanwhile, there are no universally accepted tools to measure the effectiveness of treatment. It is known that CRPS is accompanied by impaired microcirculation of affected tissue, such as vasoconstriction and reduced regional blood flow and oxygenation, which then leads to skin temperature change, pain, and atrophic changes. Thus, a direct non-invasive measurement of microcirculation is of considerable interest for accurate and early diagnosis of CRPS. PAM is shown to be a powerful tool for studying the microcirculatory system at the site of CRPS. In the presented results, the blood perfusion increase after SGB was directly observed, which is consistent with the patients' subjective sense of pain relief. Based on time-of-flight in the depth direction and raster 2D scanning in the horizontal direction, PAM can reconstruct 3D information of the blood vessel anatomy and the distributions of hemoglobin concentration and oxygen saturation, which may provide additional information for diagnosis and improvement after treatment. Our experiments show that a relatively obvious blood perfusion increase after SGB exists at the shallow depth where

the capillary bed is located. Although the data are preliminary, they suggest a strong relation between the development of CRPS and microcirculatory changes.

PAM is able to measure the oxygen saturation in a single blood vessel or the average values in a desired area. Pain, autonomic changes, and functioning impairment in patients with CRPS may be more related to the actual tissue extraction of oxygen and nutrients in the affected area than to the supply of oxygen and nutrients from microcirculation. Some reports suggest that arterial oxygen saturation (SaO_2) alone may not be helpful enough to diagnose CRPS, and thus venous oxygen saturation is essential. Due to its absorption contrast mechanism, PAM with double wavelengths is sensitive to both oxyhemoglobin and deoxyhemoglobin, and is able to measure the oxygen saturation in both arteries and veins.

SGB with local anesthetics is used frequently in the management of CRPS-1 of the upper extremities, with variable degrees of success in pain relief and improvement of function. This inconsistency of outcome may be related to sympathetically maintained pain (SMP) and sympathetically independent pain (SIP). SMP may be differentiated from SIP by a sympatholytic challenge provided by an intravenous injection of the α-adrenergic blocker phentolamine or sympathetic blocks. Our preliminary data indicated only a subset of patients responded to SGB well, with significant pain relief and changes of PA signal and sO_2, which supports the observation that "neuropathic pain is mediated or maintained by the sympathetic nervous system in only a subset of patients".

Despite the advantages listed above, the two-dimensional scanning of current PAM has relatively a long acquisition time, which leads to some motion artifacts in the image. Further improvement of imaging speed is possible by implementing mirror scanning. Limited by the strong attenuation

of high frequency acoustic signals, the AR-PAM system used in this work can image only as deep as 3 mm in biological tissue. To investigate the microcirculatory changes of deep tissue such as muscles and bones in the area affected by CRPS, an AR-PAM system with a lower central frequency transducer (e.g., 5 MHz) can be used in the future, which extends the imaging depth to 4 cm. Based on a small number of subjects, our data are promising but preliminary. Randomized, controlled, and double-blinded clinical trials are needed to verify the clinical application of PAM systems to CRPS evaluation and management.

3.2 Conclusions

In this paper, peripheral blood vessels in two sites in patients' hands were imaged by PAM systems. From pre to post SGB block, there were a 50% increase in signal intensity of PAM and 4% increase in sO_2, which agreed with the increased temperature and decreased pain level. The results showed that blood perfusion increased after SBG, which is consistent with prior reports. Unlike other imaging methods, PAM can provide non-invasive high spatial resolution images as well as functional sO_2 measurement. In these preliminary results, PAM showed its potential for helping both monitor and diagnose CRPS.

Chapter 4 Photoacoustic Flowmetry in Humans

In this chapter, we aim to quantify blood flow velocity in humans. We first propose a cross-correlation-based method to measure blood flow velocity by using optical resolution photoacoustic microscopy. We demonstrate our method in phantom, *ex vivo*, and *in vivo* experiments. However, because this method can work only in the optical ballistic regime, deep flow in humans cannot be quantified. Then we propose two methods to solve this problem: saline-injection-based and cuffing-based flowmetry. For the saline-injection-based method, we demonstrated it in mice. For the cuffing-based method, we successfully measured blood flow speed in humans. Work in this chapter has been published in Journal of Biomedical Optics, Optics Letters, and Journal of Biophotonics [31, 91-93].

4.1 Calibration-free Transverse Blood Flow Measurement Based on Time-domain Cross Correlation Using Photoacoustic Microscopy *in Vivo*

Background Noninvasive and accurate blood flow measurement provides important physiological information for medical diagnosis [94, 95]. Many imaging modalities have been implemented to measure blood flow [96-100]. PAM has been widely used in various applications, including functional brain imaging, gene expression, and early cancer detection. PAM has also shown promising results in flow measurement [30, 101-105]. These previous investigations were based on photoacoustic Doppler (PAD) shift, time-domain PA autocorrelation or frequency-domain PAD bandwidth broadening. The PAD shift is introduced when a static ultrasonic transducer receives PA signals generated by moving particles. The shift can be converted to flow

velocity using the Doppler theory. This method has several advantages, such as illumination angle independence, high signal-to-noise ratio (SNR), and weak background noise. However, Doppler flowmetry becomes less accurate when the detection axis becomes nearly perpendicular to the flow direction. Therefore, it cannot accurately measure microvascular flow velocity at a shallow depth where the transverse flow component dominates. Time-domain PA autocorrelation can also be used for flow velocity measurement. When a moving particle traverses the illumination area, the flow velocity is determined by the time duration of the resultant PA signal and can be extracted by analyzing the slope of the normalized autocorrelation function. In the frequency domain, flow velocity is represented by the broadening effect of the PAD bandwidth. However, the measured flow velocity from these methods depends on the particle size, and a calibration is required.

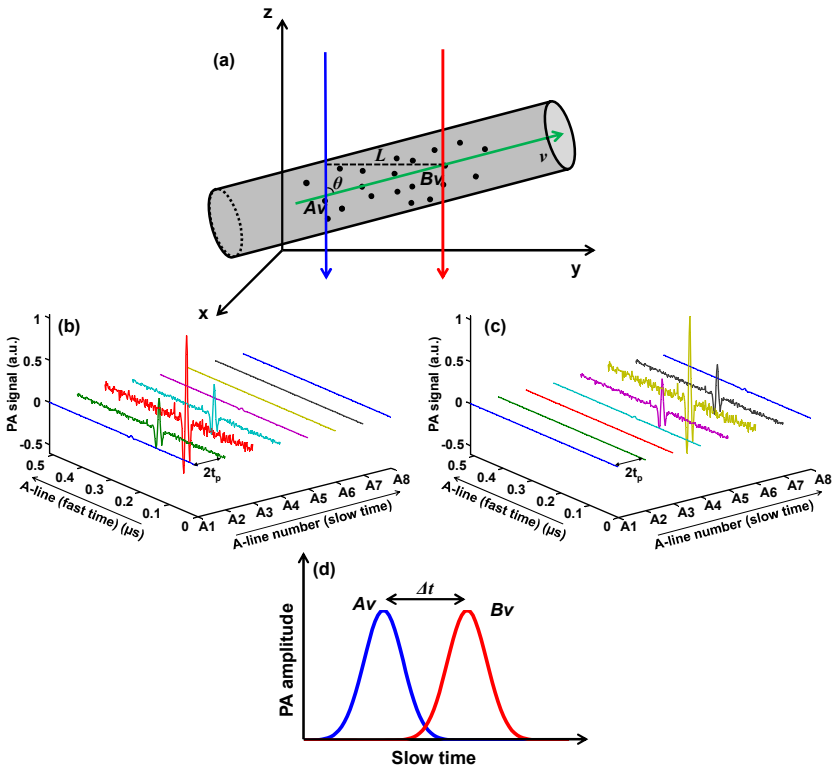

Figure 4.1 Principle of flow measurement by PAM based on cross correlation. (a) Two laser beams (blue and red arrows) illuminate the measurement area of a blood vessel alternately. The axes of the two beams are separated by

distance L. Sequential A-lines are acquired at (b) A_v and (c) B_v at an interval time of $2t_p$. (d) The slow-time PA profiles from A_v and B_v are shifted in time by Δt.

In this section, we propose a method to measure transverse flow velocity by using cross correlation. The proposed method overcomes the limitations of previous approaches. We shall demonstrate that our proposed method is able to deliver a pair of spatially-resolved laser beams to the target, so that the transverse flow speed and the direction can be directly retrieved by cross correlating a pair of slow-time PA profiles (to be defined below). In addition, our method can detect depth-dependent flow velocity, and the measurement is not affected by the particle size. Moreover, we investigated both maximum and minimum measurable velocities. Finally, we demonstrate the feasibility of our method in phantom, *ex vivo*, and *in vivo* experiments.

Method The principle of cross-correlation-based flow velocity measurement is depicted in Figure 4.1. Two parallel laser beams, separated in space by a distance L, alternately illuminate the measurement region of a blood vessel. The time interval between two consecutive laser pulses is t_p. The flow is assumed to be laminar and linear. An in-plane streamline with a velocity v is drawn as a green arrow in Figure 4.1(a). The points of intersection between the two beams and the streamline are denoted as A_v and B_v. Both points lie within the acoustic focus of the ultrasonic transducer. Radiofrequency PA A-lines, referred to as "fast-time-resolved" PA signals, are acquired from each beam alternately at half of the pulse repetition rate of the laser (Figure 4.1(b), (c)). A series of fast-time-resolved signals is time-gated according to the depths of A_v and B_v. PA amplitudes of all A-lines at these depths are extracted by taking the maximum amplitude projection (MAP) of the A-lines. Subsequently, a series of PA amplitudes from A-line sequences acquired from both points are converted to two envelopes, referred to as "slow-time" PA profiles. When the same group of particles traverses A_v and B_v, the slow-time PA profiles from A_v and B_v appear with

identical shapes, and with a time shift Δt (Figure 4.1(d)). The time shift is computed with the cross correlation of the slow-time PA profiles from A_v and B_v. The flow velocity is calculated by

$$v = \frac{L}{\sin\theta\left(\Delta t + t_p\right)}, \tag{4.1}$$

where θ is the angle of the particle flow direction with respect to the detection (z) axis. In addition, the flow direction can be determined from the sign of Δt. Therefore, both flow speed and direction are measured by the cross-correlation method. Moreover, flow velocity at any selected depth can be measured.

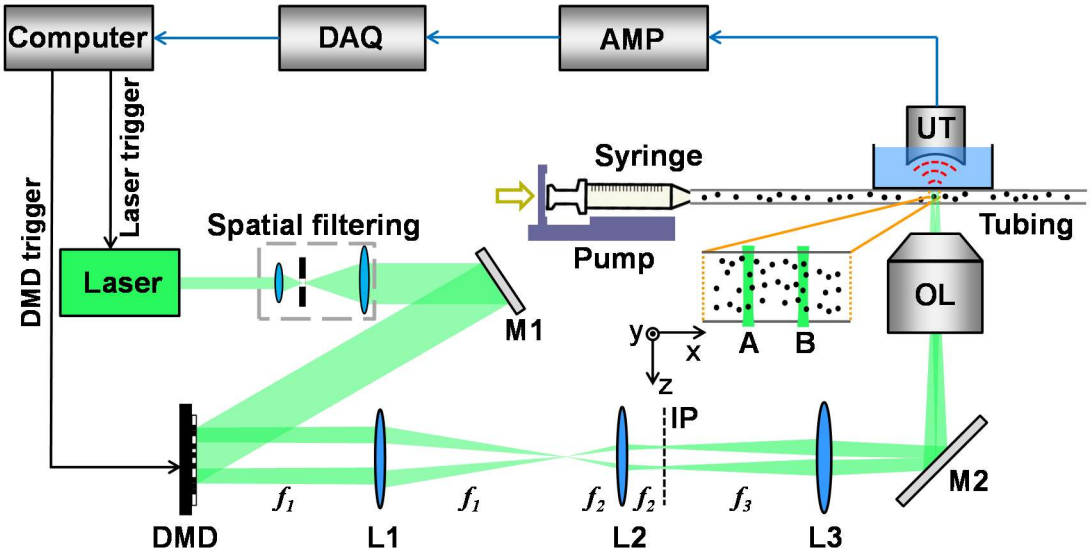

Figure 4.2 Schematic overview of the setup, not to scale. AMP, signal amplifiers and filters; DAQ, data acquisition; DMD, digital micromirror device; IP, Intermediate image plane; L1-L3, lenses (focal lengths f_1-f_3); M1-M2, mirrors; OL, objective lens; UT, ultrasound transducer.

Two requirements are imposed by the proposed method. First, the voxel size should be small enough that the PA signal fluctuation induced by the variations of the particle density within the voxel is greater than the noise. Second, two spatially separated laser beams must be delivered at a high repetition rate, in order to enable measuring a fast flow velocity. We integrated a digital

micromirror device (DMD) (.7XGA DDR Discovery™ 4100, Texas Instruments) with an OR-PAM system to satisfy these two requirements (Figure 4.2). A diode-pumped solid-state laser (INNOSLAB, Edgewave, $\lambda = 532$ nm) with a repetition rate of 10 kHz ($t_p = 0.1$ ms) was used as the illumination source. This laser had maximum output pulse energy of 300 μJ, and the pulse duration was 10 ns. After spatial filtering and collimation, the expanded laser beam was incident on the DMD. Patterns generated by micromirrors on the DMD were imaged into the target. An ultrasonic transducer (V214-BB-RM, Olympus NDT Panametrics) with a central frequency of 50 MHz was placed confocally with the objective lens. Fast-time-resolved PA signals (A-lines) were amplified and then acquired by a 12-bit digitizer (ATS9350, AlazarTech). The entire system was synchronized by a multifunction data acquisition card (PCI-6251, National Instruments).

The DMD consists of an array of 1024×768 micromirrors with a pitch distance of 13.68 μm. To realize the "ON" or "OFF" state, each micromirror can be latched in either the +12° or -12° position from the DMD surface normal. The entire device, therefore, functions as a binary-amplitude spatial light modulator. As the most widely adopted spatial light modulator, DMD has advantages in operation speed, stability, and reliability. Two binary patterns were encoded on the DMD in our experiments. For the first pattern, a 96×96 micromirror square was turned "ON" while the rest of micromirrors stayed "OFF". The second pattern had the identical square pattern but was spatially shifted along the flow direction by a set distance. For most experiments presented in this paper, this distance was chosen to be 2.63 mm. When alternately imaged into the target, these two patterns formed two laser beams. Each beam had a diameter of 5 μm, and the separation between these beams was 10 μm. The DMD was synchronized with the laser at a rate of 10 kHz, resulting in an A-line repetition rate of 5 kHz (interval time 0.2 ms) from each beam.

We measured the flow of microspheres in a straight capillary tubing (60985-700, inner diameter = 300 μm, VWR). Three sizes of microspheres (17137-15 (diameter $d_p = 3\,\mu\text{m}$), 15714-5 ($d_p = 6\,\mu\text{m}$), and 24294-2 ($d_p = 10\,\mu\text{m}$), Polysciences) were separately suspended in water. The suspensions were pumped into the tubing through a syringe, and the flow speed was controlled by a syringe pump (BSP-99M, Braintree Scientific). For each measurement, N_{total} pulses were used for each laser beam to acquire a series of PA A-lines at a 5 kHz rate for a given detection time $t_{total} = 2N_{total}t_p$. For a selected fast-time window, we applied maximum amplitude projection (MAP) to all measured A-lines to detect the slow-time PA profile, then correlated the two slow-time PA profiles and averaged the multiple correlation results to determine the flow velocity.

Results In the first experiment, we used 10-μm-diameter microspheres to measure the flow velocity (Figure 4.3). The red line with the legend of "Ideal" in this and the following figures represents measured flow velocities equal to the preset values. The flow velocity was varied from -6.84 mm/s to +6.84 mm/s, which covers the normal physiological flow velocity range in arterioles with diameters less than 80 μm. The tubing was adjusted to be perpendicular to the detection axis of the ultrasound transducer ($\theta = 90^\circ$), and to be in the same plane as the two laser beams. For each measurement, we observed an expected positive or negative time shift from the raw data (insets in Figure 4.3). The average velocity and standard error at each data point were computed from 10 measurements. The measured velocities agreed well with the preset average flow speeds in both directions. We used the root-mean-square error of prediction (RMSEP) to describe the measurement accuracy,

$$RMSEP(v) = \sqrt{e_s^{\,2} + e_r^{\,2}}\,, \tag{4.2}$$

where systematic error e_s and random error e_r are defined as

$$e_s = \sqrt{\frac{1}{n-1}\sum_{i=1}^{n}(v_{mi} - v_{pi})^2} \tag{4.3}$$

and

$$e_r = \sqrt{\frac{1}{n}\sum_{i=1}^{n}\sigma_i^2}\ . \tag{4.4}$$

Here, v_{pi}, v_{mi}, and σ_i are the preset average velocity, measured average velocity, and measured standard error of the i_{th} velocity out of a total of n velocities, respectively. For this experiment, the RMSEP of the measured flow velocity was quantified to be 0.22 mm/s, with the systematic error and random error being 0.10 mm/s and 0.19 mm/s, respectively.

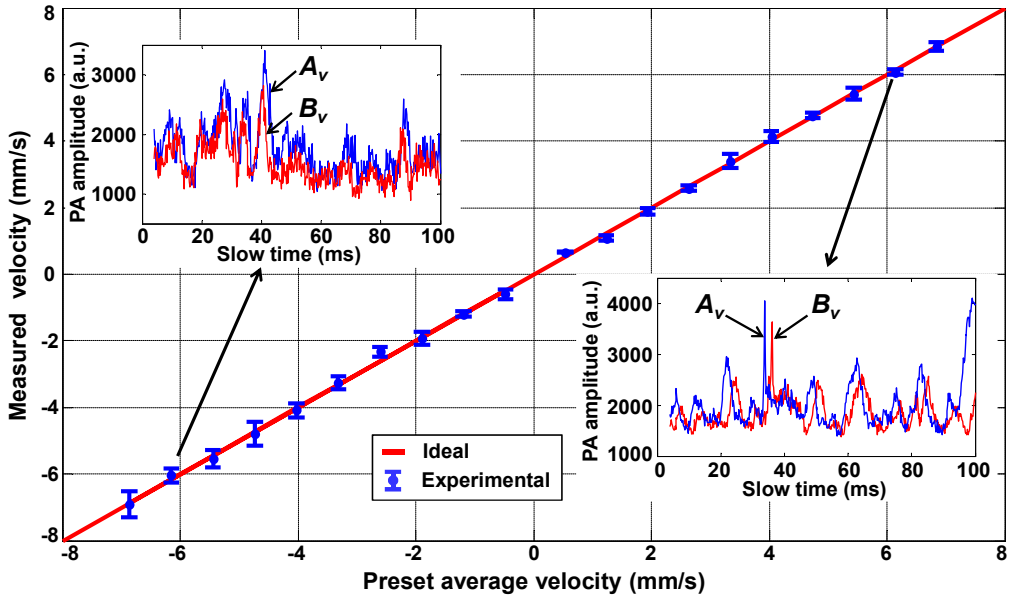

Figure 4.3 Measured transverse flow velocities using 10-μm-diameter microspheres. Inset figures show raw slow-time PA profiles from A_v (blue) and B_v (red) in Figure 4.1 at two selected flow velocities v = +6.14 mm/s and v = –6.14 mm/s. Error bars: standard errors.

In addition, we investigated the flow velocity with different particle sizes (Figure 4.4). Experimental results evidently illustrate that the measured flow velocity is independent of the particle size (Figure 4.4(a)) within the preset range $|v| = 0.55 - 6.49$ mm/s. A detailed examination of the raw data (Figures 4.4(b)-(d)) reveals that measured slow-time PA profiles were modulated with different intensities and time durations, which resulted both from different particle sizes and from the relative positions between the particles and the laser beams. For the autocorrelation method, because the flow velocity is calculated based on the time-domain narrowing effect (or on bandwidth broadening in the frequency domain) of individual profiles, it is necessary to calibrate for the particle size. On the contrary, we circumvented this calibration process by analyzing the time delay between two sequential slow-time PA profiles. Consequently, all three sets of raw data produced the consistent result, and the flow velocity was not subject to experimental changes in particle sizes.

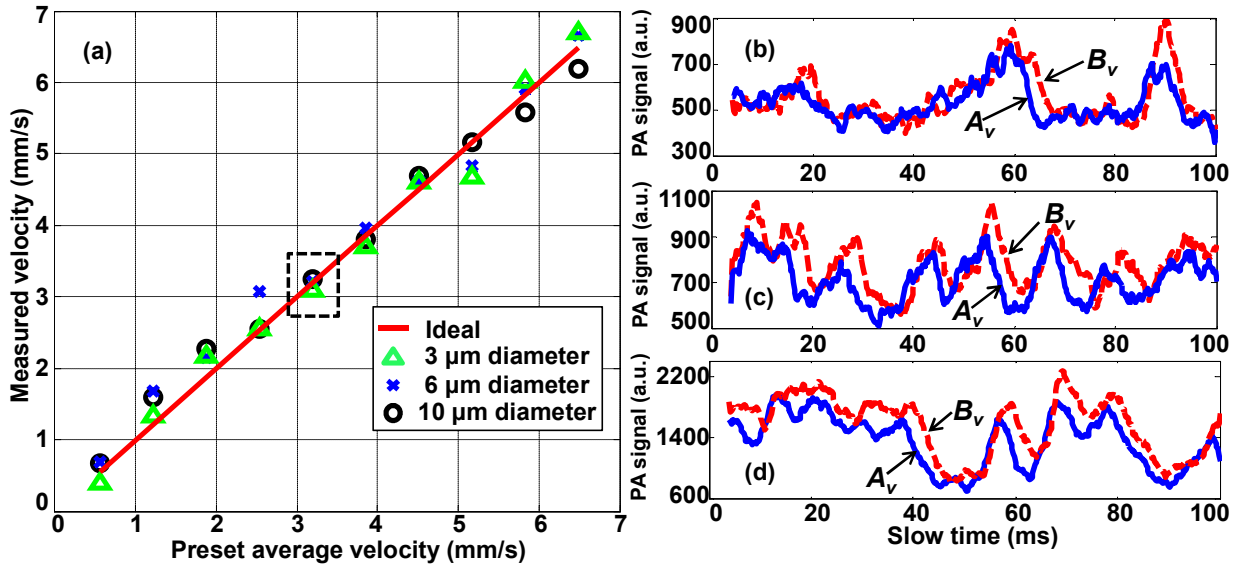

Figure 4.4 (a) Flow velocities measured using three sizes of microspheres. (b)-(d) The slow-time PA profiles from A_v (blue solid line) and B_v (red dashed line) in Figure 4.1 with the same flow speed (dashed box in (a)) for (b) 3 μm, (c) 6 μm, and (d) 10 μm -diameter microspheres. The calculated average time shift between the blue and red slow-time PA profiles is the same regardless of individual profile shapes.

The size-independent flow measurement makes the proposed method attractive for measuring blood flow. The non-spherical shape of red blood cells (RBCs) or RBC clusters would alter the shape of the slow-time PA profiles. Using previous methods, this change would increase the measurement errors. On the other hand, using the proposed method, flow velocity information is extracted from the time delay between the two slow-time PA profiles. Because the two laser beams are only 5-15 μm away from each other, RBCs or RBC clusters are likely to maintain their orientation when they traverse these two laser beams. Thus, the two slow-time PA profiles will still have identical shapes, and the flow speed can be accurately calculated.

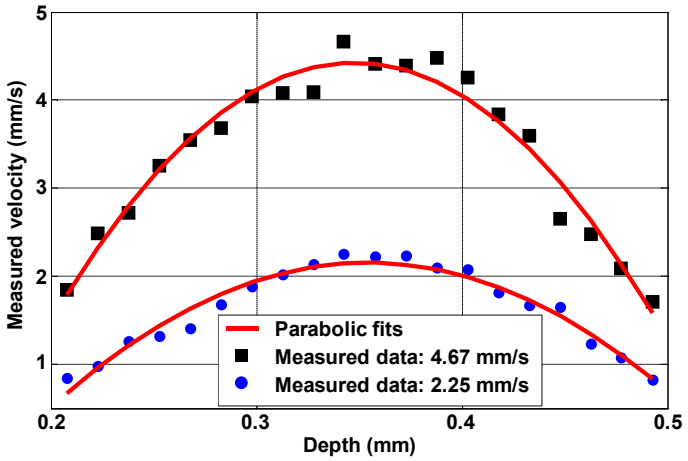

Figure 4.5 Measured flow velocities with parabolic fits in the depth direction, using 10-μm-diameter microspheres. The peak flow velocities are 2.25 mm/s (●) and 4.67 mm/s (■).

With the assumption of laminar flow, the transverse flow velocity should follow a parabolic curve in the depth direction. In our experiment, each PA A-line was time gated with 10 ns windows, which divided the entire tubing diameter uniformly into 20 streamlines of 15 μm thick each. Then the flow velocity was analyzed for each layer. Two measured depth profiles for different preset average transverse flow velocities are shown with parabolic fits in Figure 4.5. Measured peak

velocities of these two profiles are 2.25 mm/s and 4.67 mm/s. As expected, the flow velocity peaks at the center of the tubing and falls approximately parabolically to the wall.

Using the proposed method, we further investigated the maximum and minimum measurable flow velocities of 10-μm-diameter microspheres. For the measurement of maximum flow velocity, the experimental results illustrated that the measured values were linear with the preset flow velocities until plateaus develop appreciably (Figure 4.6(a)). In theory, the maximum measurable velocity was reached when a flowing particle was detected only once by each laser beam. Thus, the maximum measurable velocity in our experimental setup at $\theta = 90^\circ$ can be computed by Equation 4.1 as

$$|v_{\max}| = \frac{L}{t_p}. \tag{4.5}$$

Equation 4.5 shows that, at a constant laser repetition rate, $|v_{\max}|$ solely depends on the distance L. For $L = 5,\ 10,\ \text{and}\ 15\ \mu\text{m}$, the theoretical $|v_{\max}|$ values are 50.00 mm/s, 100.00 mm/s, and 150.00 mm/s, respectively. In comparison, the maximum relative errors of the measurements occurred at preset velocities of 26.73, 50.47, and 56.41 mm/s in the range of $|v| = 0.46 - 62.34\,\text{mm/s}$ (Figure 4.6(b)). This discrepancy comes from the discrete nature of the time shift measurement, which produces the plateaus before the theoretical $|v_{\max}|$ values. Based on Equation 4.1 ($\theta = 90^\circ$ in our experimental setup), we could not accurately measure velocities between $L/(\Delta t + t_p)$ and $L/(\Delta t + 3t_p)$. The velocity difference Δv is expressed as

$$|\Delta v| = \frac{L}{\Delta t + t_p} - \frac{L}{\Delta t + 3t_p} = \frac{2Lt_p}{(\Delta t + t_p)(\Delta t + 3t_p)}. \tag{4.6}$$

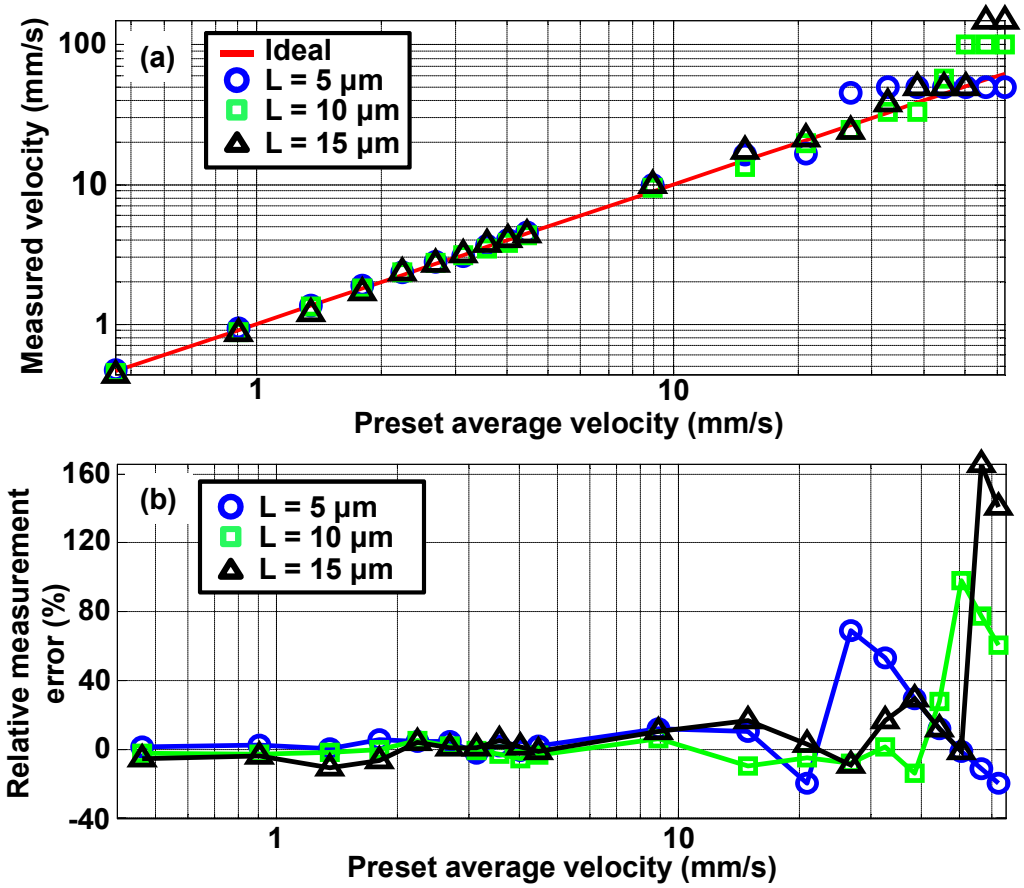

Figure 4.6 Quantification of the maximum measurable velocities for 10-μm-diameter microspheres. (a) Log-log plot of the measured flow velocities for three different distances. (b) Semi-log plot of the relative errors of the measured velocities.

The mean velocity $\bar{v}$ within this velocity range is:

$$\bar{v} = \left(\frac{L}{\Delta t + t_p} + \frac{L}{\Delta t + 3t_p}\right) / 2 = \frac{L(\Delta t + 2t_p)}{(\Delta t + t_p)(\Delta t + 3t_p)}. \tag{4.7}$$

Thus, the maximum relative error is given by

$$\left|\frac{\Delta v}{\bar{v}}\right| = \frac{2t_p}{\Delta t + 2t_p}. \tag{4.8}$$

Equation 4.8 shows that, when Δt had small discrete values, the cross-correlation process had low accuracy, resulting in the plateaus in Figure 4.6(a). In order to maintain acceptable velocity accuracy, we chose a 2-point shift between the two slow-time PA profiles to calculate $|v_{\max}|$, which has a relative error less than 33%. The resulting $|v_{\max}|$ values were 10.00 mm/s for $L = 5$ μm, 20.00 mm/s for $L = 10$ μm, and 30.00 mm/s for $L = 15$ μm.

It is noted that a short distance between the two beams (L) and a long detection time (t_{total}) are conducive to slow flow measurement. Fundamentally, the minimum measurable velocity $|v_{\min}|$ is limited by particle diffusion caused by Brownian motion. Particles could move out of the laser illumination area in a laminar flow during the traveling time, which would de-correlate the slow-time PA profiles from A_v and B_v. Based on the Brownian motion theory, the average displacement of particles $\bar{r}$ with diameter d_p can be calculated by

$$\frac{\bar{r}^2}{2t} = \frac{k_B T}{\pi \eta d_p}, \tag{9}$$

where $t = L/|v|$, k_B is Boltzmann's constant, η is the viscosity of the liquid, and T is the absolute temperature. Given a Gaussian beam with 5 μm diameter, a 1 μm shift in space introduces only a small change of PA signals, and the two slow-time PA profiles are still correlated. Correspondingly, we can detect flow with velocity as low as $|v_{\min}| = 1.44$ μm/s for 10-μm-diameter particles.

In addition, particles can drift in the depth direction due to gravity, drag, or convective motion due to laser-induced temperature distribution. Such depth drift could lead to de-correlation between

slow-time PA profiles for a chosen fast-time gate. The following example is given to estimate the minimum measurable flow velocity. Particles with 10 μm diameter are suspended in water. Let us assume a 5% mismatch between the mass densities of the particle and the surrounding liquid, due to either the material or thermal expansion of the particle. Such a level of mismatch is typical for red blood cells in phosphate buffered saline especially in the presence of a substantial temperature fluctuation. The particles mainly experience the Stokes force, buoyance, and the gravity force. In equilibrium, these particles carry a flow speed of 2.72 μm/s in the depth direction. Assuming the particle starts drifting from a depth in the center of a 10 ns window, it would take 2.76 s for the particle to drift out of the time window. Correspondingly, $|v_{\min}|$ would be approximately 1.80 μm/s for a distance $L = 5$ μm .

Before this limit would be reached, however, other experimental factors might intervene in the measurement. Flow velocity, especially in biological systems, changes over time. Hence, there is a good reason to keep the detection time as short as possible. In our experiments, at a slow velocity, it was possible that the particle had not traversed the laser beam during the entire measurement; as a result, only a fraction of the slow-time PA profile of the particle was captured. Consequently, the cross-correlation result was exacerbated due to reduced correlation between the two measured slow-time PA profiles. Thus, we required that the full profile of the particle be captured by both laser beams to maintain an accurate cross-correlation result, which defined $|v_{\min}|$. Correspondingly, $|v_{\min}|$ was determined by the distance L, beam diameter d_b, particle size d_p, total time for one measurement (t_{total}), and the noise-induced correlation peak shift ΔN_n, using

$$|v_{\min}| = \frac{d_b + L + d_p}{[2(N_{total} + \Delta N_n) + 1]t_p}. \tag{2.10}$$

The typical SNR in our experiments ranged from 15 to 20, and our results showed that this produced only a negligible ΔN_n in the measurement; therefore, $|v_{\min}|$ was primarily determined by the distance parameter and t_{total}.

We first set the distance to three different numbers ($L = 5,\ 10,$ and 15 μm) to examine $|v_{\min}|$ (Figure 4.7(a)). We measured flows in the range $|v| = 0.06 - 0.46$ mm/s at these distances. The calculated $|v_{\min}|$ for these distances were 0.20 mm/s, 0.25 mm/s, and 0.30 mm/s, respectively, for a fixed time $t_{total} = 100$ ms. Above the calculated $|v_{\min}|$, the measured results were in close agreement with the preset values. However, when the preset flow velocities were smaller than the calculated $|v_{\min}|$, the measured velocities stayed roughly equal to the calculated $|v_{\min}|$.

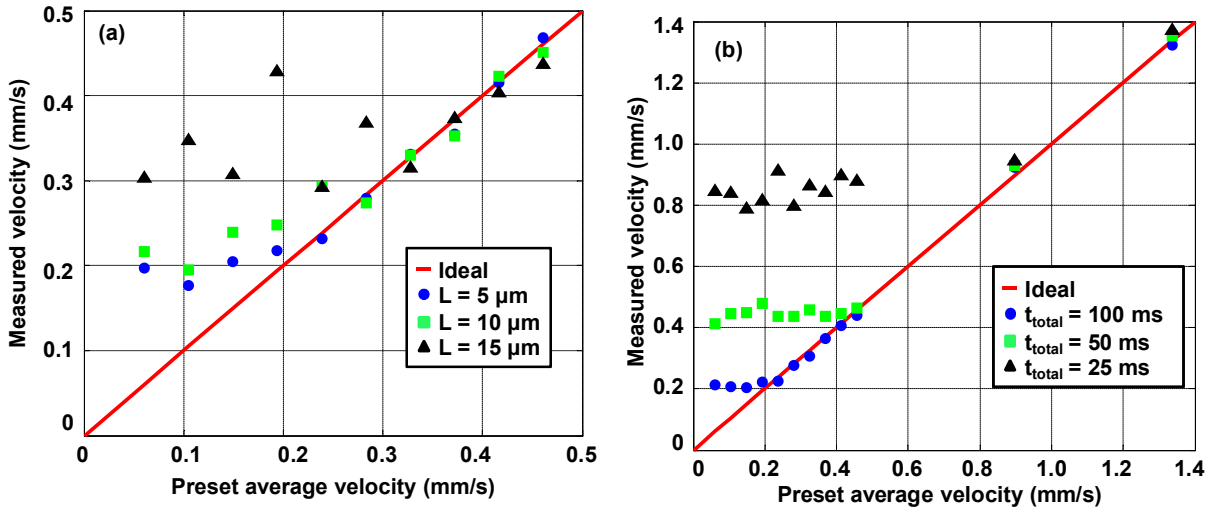

Figure 4.7 Quantification of the minimum measurable flow velocity for 10-μm-diameter microspheres. (a) Measured flow velocities for three different distances at slow preset flow velocity range $|v| = 0.06 - 0.46$ mm/s for a fixed time $t_{total} = 100$ ms. (b) Measured flow velocities using three different t_{total} at a fixed distance $L = 5$ μm.

We also studied the relation between t_{total} and $|v_{\min}|$ at a fixed distance $L = 5$ μm (Figure 4.7(b)). Measurements in the range $|v| = 0.06 - 1.34$ mm/s were made using $t_{total} = 25$, 50, and 100 ms. The calculated $|v_{\min}|$ for these times were 0.80 mm/s, 0.40 mm/s, and 0.20 mm/s, respectively. Similar to Figure 4.7(a), the measured flow velocity reached a constant value approximately equal to the calculated $|v_{\min}|$, showing good agreement with the theoretical values.

Next, we demonstrated the feasibility of our proposed method in a biological environment. A piece of chicken tissue 250–300 μm thick was placed underneath the tubing as a scattering and absorbing medium. We set the distance $L = 10$ μm for the experiment and used 10-μm-diameter microspheres as the target. As shown in Figure 4.8, the measured flow velocities were in conformity with preset values in the entire range. From Equations 4.2–4.4, the measurement accuracy was calculated to be 0.35 mm/s, with a systematic error of 0.29 mm/s and a random error of 0.19 mm/s.

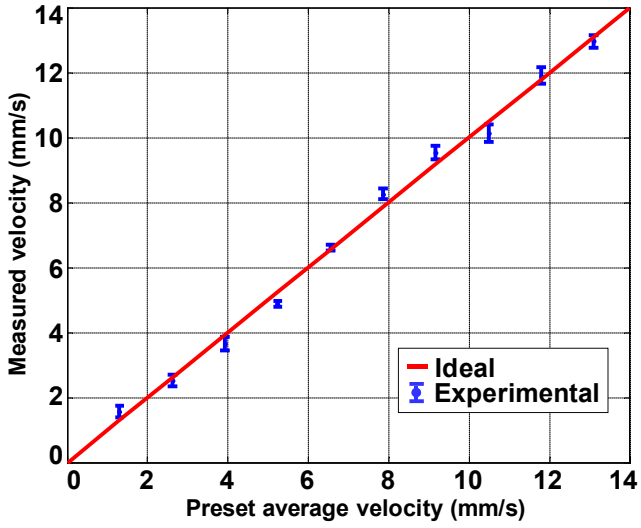

Figure 4.8 Measured average flow velocities with underlaid chicken tissue. Error bars: standard errors.

In an *ex-vivo* study, fresh defibrinated bovine blood (910-250, Quad Five) was driven through a straight plastic tube (60985-700, inner diameter = 300 μm, VWR) by a syringe pump (BSP-99M, Braintree Scientific), with flow velocities ranging from 0.45 to 18 mm/s. In the experiment, the distance d between the two measurement spots A_v and B_v was set to 5 μm, and the angle θ was set to 90°. The standard deviation at each data point was calculated from 10 measurements. As shown in Figure 4.9, the measured flow velocities agreed well with the preset values in the flow velocity range. The similar shape of the slow-time PA amplitude profiles in each of the two inset figures clearly illustrates that the same group of RBCs was accurately captured at A_v and B_v. The unequal PA amplitudes from A_v and B_v are due to the uneven spatial light intensity distribution and uneven detection sensitivity of the transducer in the field of view. Because Δt must be an integral multiple of the laser pulse interval, the cross-correlation process had low precision when Δt digitally approached zero, displaying as larger error bars in Figure 4.9.

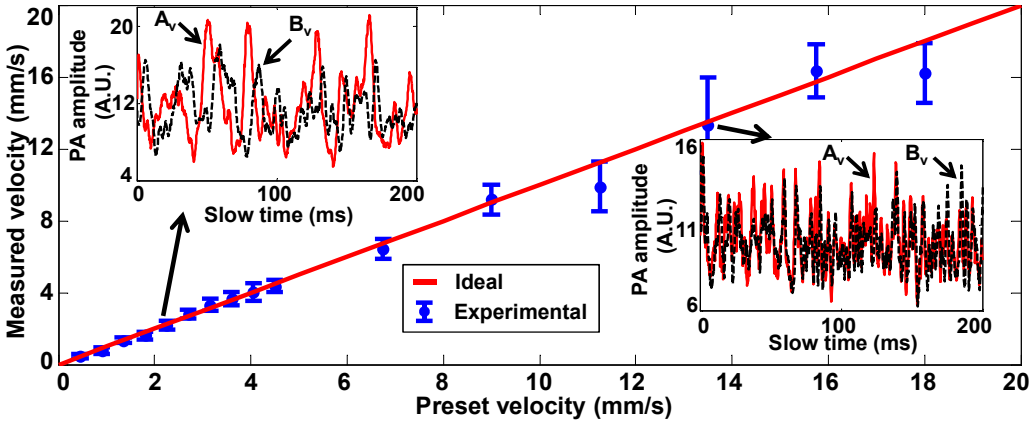

Figure 4.9 Measured transverse flow velocities of defibrinated bovine blood versus preset values. Inset figures show time courses of slow-time PA profiles from A_v (red line) and B_v (black dashed line) in (a) at two selected flow velocities, $v = 2.25$ mm/s and $v = 13.5$ mm/s.

We next measured flow velocities of vessels in a mouse ear *in vivo*. A nude mouse (Hsd:Athymic, Nude Mouse; Harlan, Indianapolis, Indiana) was used in the experiment. The experimental animal procedure was carried out in conformance with the laboratory animal protocols approved by the Animal Studies Committee of Washington University in St. Louis. For all the *in vivo* experiments, we targeted shallow

micro-vascular structures that were parallel to the tissue surface. As a result, all the measured vessels were perpendicular to the detection axis ($\theta = 90°$).

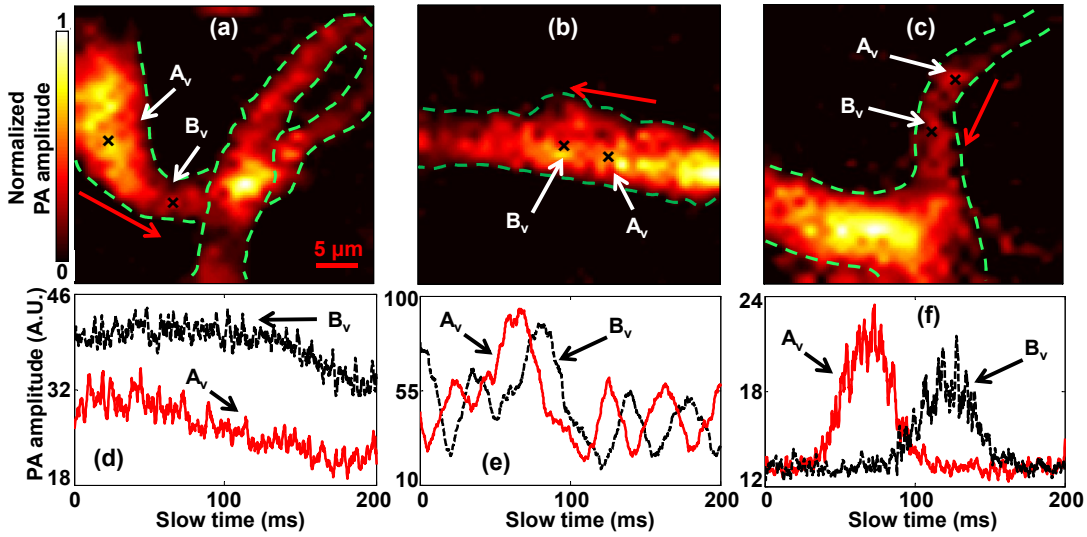

Figure 4.10 *In vivo* blood flow measurements in vessels with different structures. Black crosses denote locations of the two measurement spots. Red arrows denote the flow direction. PA images of (a) a loop vessel, (b) a straight vessel, and (c) a vessel bifurcation. (d-f) Time courses of slow-time PA profiles from A_v and B_v in (a-c), respectively.

Table 4.1 Flow velocity measurements in vessels with different structures.

Corresponding figures	*d* (μm)	Δ*t* (ms)	*v* (mm/s)
(a) and (d)	7.8	2.3	3.4
(b) and (e)	3.2	13.9	0.23
(c) and (f)	5.8	55.1	0.11

To show that our method can be used to measure flow velocity in vessels with different structures, we imaged three representative structures: a loop, a straight vessel, and a bifurcation, as shown in Figures 4.10(a-c). To quantify the flow velocities in these vessels, two close spots A_v and B_v were selected in each vessel. The measured slow-time PA amplitude profiles from A_v and B_v in Figures 4.10(a-c) are shown in Figures 4.10(d-f), respectively. The measured distances *d*, time shifts Δ*t*, and flow velocities *v* are shown

in Table 4.1. In addition, the signs of the time shift Δt in each vessel denote the flow direction of the blood, as marked by the red arrows in Figures 4.10(a-c). Our results show that, in vessels with different structures, the flow velocity can be quantified by our method.

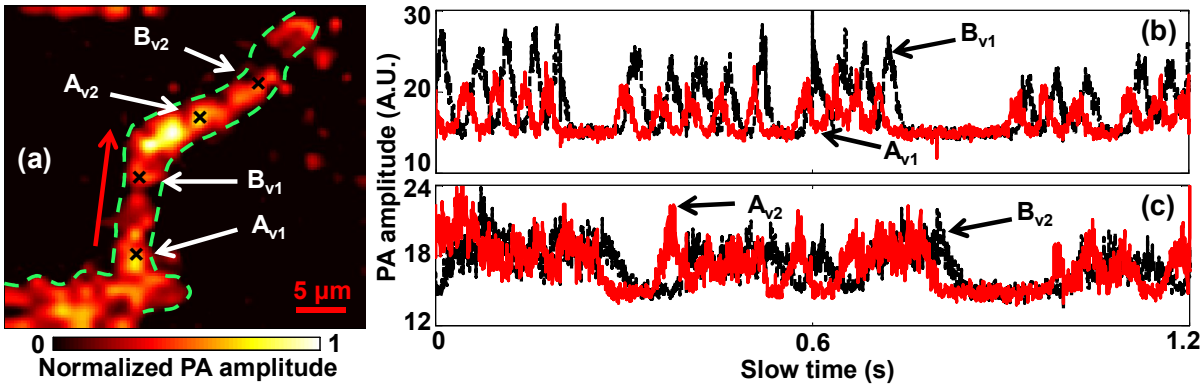

Figure 4.11 Measurement of flow changes in a curved vessel. (a) PA image of the vessel. Black crosses denote the locations of the monitoring spots. Red arrow denotes the flow direction. Time courses of slow-time PA profiles from (b) A_{v1} and B_{v1}, (c) A_{v2} and B_{v2} in (a).

Table 4.2 Flow velocity measurements in a single vessel.

Monitoring spots	d (μm)	Δt (ms)	v (mm/s)
A_{v1} and B_{v1}	4.0	16.5	0.24
A_{v2} and B_{v2}	5.0	36.9	0.14

In addition, we studied spatial flow velocity changes in the same vessel. As shown in Figure 4.11(a), two pairs of spots denoted as A_{v1}-B_{v1}, A_{v2}-B_{v2}, were chosen to measure flow velocities in different locations of a curved vessel. The measured slow-time PA amplitude profiles from A_{v1}-B_{v1} and A_{v2}-B_{v2} are shown in Figure 4.11(b-c), respectively. As shown in Table 4.2, the flow velocities calculated from A_{v1}-B_{v1} and A_{v2}-B_{v2} were 0.24 mm/s and 0.14 mm/s, respectively. The similar profiles from A_{v1}, B_{v1}, A_{v2}, and B_{v2} illustrate that the same group of RBCs was imaged at these spots. However, while travelling in the vessel, this group of RBCs slowed down. This might be caused by blood leakage, blood flux conservation, or

interaction between RBCs and the vessel wall. To our knowledge, this is the first time that a flow velocity change was observed for the same group of RBCs, which might be useful for many blood disorder studies.

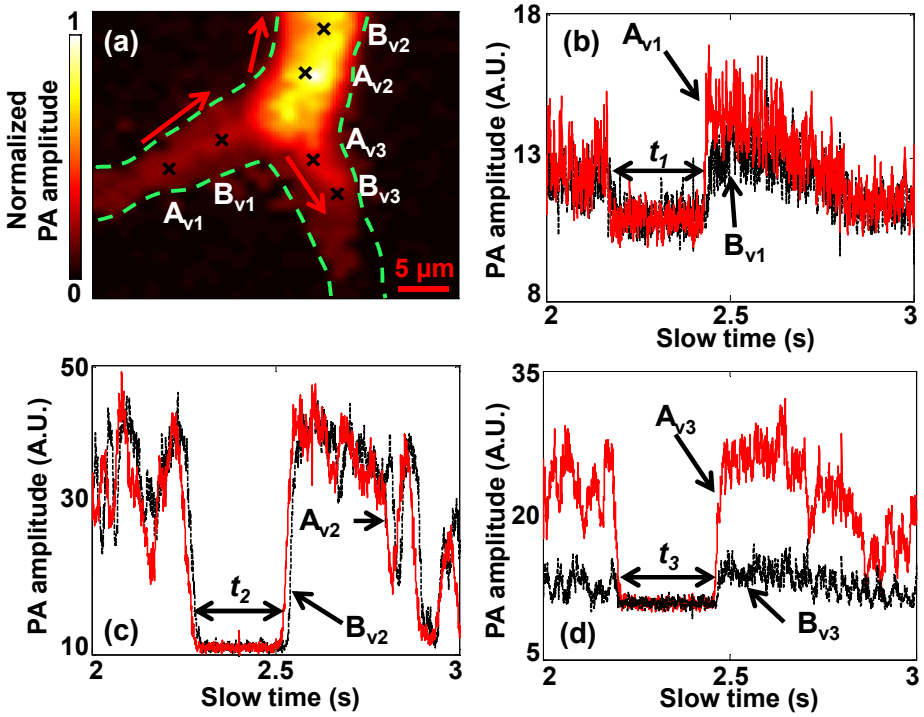

Figure 4.12 Observation of feature conservation in a vessel bifurcation. (a) PA image of a vessel bifurcation. Black crosses denote locations of the monitoring spots. Red arrows denote the flow directions. Time courses of slow-time PA profiles from (b) A_{v1} and B_{v1}, (c) A_{v2} and B_{v2}, (d) A_{v3} and B_{v3} in (a). The duration of the valley was (b) t_1, (c) t_2, and (d) t_3.

Table 4.3 Flow velocity measurements in a vessel bifurcation.

Monitoring spots	*d* (μm)	Δ*t* (ms)	*v* (mm/s)
A_{v1} and B_{v1}	5.0	7.1	0.71
A_{v2} and B_{v2}	4.5	12.1	0.37
A_{v3} and B_{v3}	3.2	12.7	0.25

Finally, we further quantified the flow velocity from the same feature in a vessel bifurcation. A PA image of the vessel bifurcation is shown in Figure 4.12(a). For flow measurement, three pairs of spots (A_{v1}-B_{v1}, A_{v2}-B_{v2}, and A_{v3}-B_{v3}) were chosen in the bifurcation. The measured slow-time PA amplitude profiles from A_{v1}-B_{v1}, A_{v2}-B_{v2}, and A_{v3}-B_{v3} are shown in Figure 4.12(b-d), respectively. The measured distances d, time shifts Δt, and flow velocities v are shown in Table 4.3. Because of the conservation of blood flux in the vessel, the features appearing upstream should be also observed downstream. If the cross section of the feature keeps constant in the stream, which might be true over a very short distance, the length of the features should be the same. As shown in Figure 4.12(b-d), the same "valley" was observed in all three pairs. The time durations of this valley in all the three figures were quantified to be t_1 = 262.2 ms, t_2 = 277.8 ms, and t_3 = 272.4 ms, respectively. Thus, the valley in the upstream vessel had a length of $t_1 \times v_1$ = 186.2 μm. Meanwhile, the sum of the valley lengths in the two downstream vessels was calculated to be $t_2 \times v_2 + t_3 \times v_3$ = 170.9 μm, close to the valley length in the upstream vessel. Taken together, these observations supported the idea of blood flux conservation.

4.2 Saline-injection-based Photoacoustic Flowmetry in the Optical Diffusive Regime

Background PAT is a modality that provides imaging in either two dimensions (2D) or three dimensions (3D). Combining the advantages of optical excitation and acoustic detection, PAT can image rich optical absorption contrast in biological tissues at depths. To date, PAT has been widely used for both structural and functional biological imaging in many different fields, including hematology, oncology, dermatology, ophthalmology, and gastroenterology. Depending on the limiting factor for spatial resolution, PAT can be divided into optical-resolution PAT (OR-PAT) and acoustic-resolution PAT (AR-PAT). In OR-PAT, the optical focus is much tighter than the acoustic focus, and a high spatial resolution can be achieved. AR-PAT provides a lower spatial

resolution, defined by the acoustic focus. Nevertheless, because in biological tissue ultrasound suffers much less scattering than light, AR-PAT can achieve deep imaging with a depth-to-resolution ratio of more than 100. So far, with high resolution, OR-PAT has imaged a variety of important biological parameters *in vivo*, such as sO_2, blood flow velocity, pulse wave velocity, and the metabolic rate of oxygen (MRO_2). However, although AR-PAT has imaged sO_2 at depths, it still cannot provide *in vivo* blood flow information. In addition, in order to calculate MRO_2 with PAT, flow needs to be measured, which makes it even more important to quantify flow.

There are two fundamental reasons why it is difficult for AR-PAT to measure blood flow velocity. First, unlike ultrasound, PAT almost has no speckles [106]. If the target has a smooth boundary with respect to the wavelengths of the PA waves, the boundary signals of the target will stand out, while the speckles inside the target are largely suppressed. Because blood vessels in biological tissues usually have smooth boundaries, it is challenging for PAT to extract blood flow information merely based on speckle fluctuations. Second, AR-PAT has a lower spatial resolution than OR-PAT and thus a larger detection voxel size. In typical OR-PAT, the spatial resolution is comparable to the size of red blood cells (RBCs). Thus, when RBCs flow into and out of the detection voxel, the PA signal changes are observable. By monitoring how fast the signal changes, the flow velocity can be calculated. However, in AR-PAT, the large detection voxel contains many more RBCs than in OR-PAT. Because the number of RBCs inside the detection voxel can be assumed to follow a Poisson distribution [27], a larger mean number of RBCs leads to a smaller relative RBC number change and thus a smaller PA signal change. For example, if there are 10,000 RBCs in the detection voxel, the PA signal change due to the RBC number change would be only around 1%, so the system would need a signal-to-noise ratio (SNR) of more than 100 to measure the flow velocity.

Although challenging, different methods have been proposed to achieve blood flow measurement with AR-PAT, including PA Doppler (PAD) flowmetry and ultrasonically encoded PA flowgraphy (UE-PAF). Based on the PAD effect, different PAD shifts have been observed from particles moving with different flow speeds, and the Doppler theory allows the flow speeds to be calculated. However, to observe the PAD shift, the moving particles have to be very sparse. Thus, this method cannot measure the flow velocity of whole blood. But by using ultrasound to encode the PA signals, UE-PAF can achieve whole blood flow imaging in deep tissue [107]. In UE-PAF, modulated ultrasound is focused into the blood vessel to create a heating source. Because PA signals are proportional to temperature, the PA signals from the heated area will increase. By monitoring the increased PA signals along the blood vessel, the flow speed in the blood vessel can be measured. However, this method's complexity has limited it to only phantoms, and so far, no *in vivo* data have been reported.

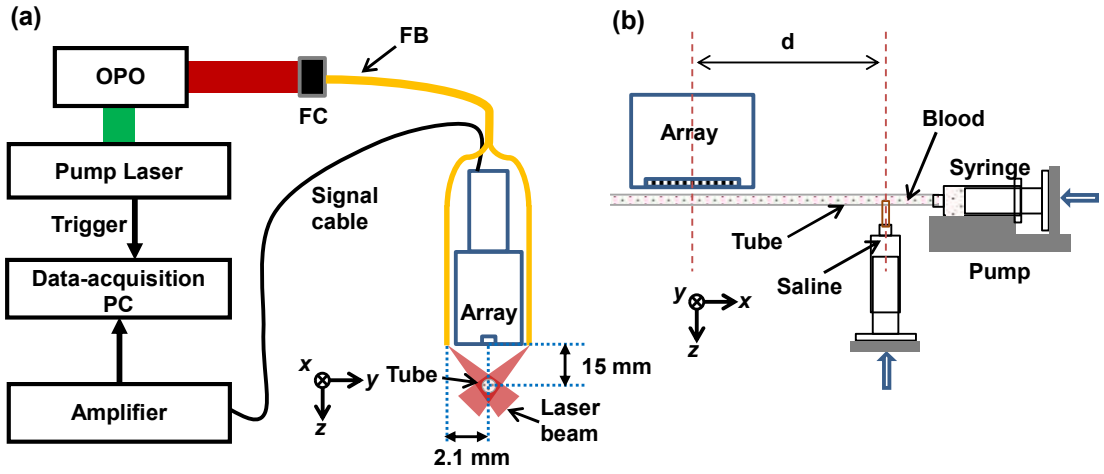

Figure 4.13 Schematic of the photoacoustic tomography system (a) and saline injection (b). (a) FB, fiber bundle; FC, fiber coupler; OPO, optical parametric oscillator. (b) d was 15 cm in the phantom experiment.

In this section, we present a new method to measure blood flow velocity deep in biological tissues. To increase the PA signal changes due to flowing RBCs, saline is injected into the blood stream.

As a result, at the saline-blood interfaces, the PA signals have sharp changes — blood's PA signal is strong while saline's signal is negligibly low. Thus, by monitoring the time course of the PA signals from the interface, the flow velocity in the blood stream can be quantified. In addition, because saline is widely used for intravenous infusion, no extra saline injection is needed in such patients.

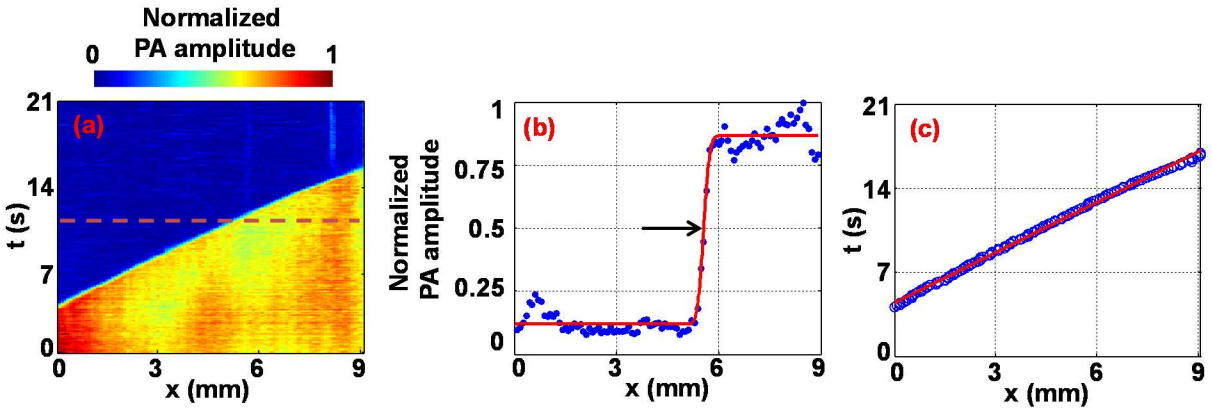

Figure 4.14 Steps to extract the flow velocity. (a) Time course of the photoacoustic (PA) amplitude of the blood vessel in the phantom experiment. (b) Blue dots, one dimensional PA amplitude along the dashed line in (a); Red line, error function fitting; Black arrow, the mean value of the error function. The mean value represents the saline-blood-interface (SBI). (c) Blue circles, time course of the SBIs; Red line, linear fitting.

Material and Method We employed a typical AR-PAT system to demonstrate this idea. As shown in Figure 4.13(a), the light source was a tunable optical parametric oscillator laser with a repetition rate of 20 Hz. For deep tissue imaging, 680 nm light was chosen for the experiments. The light was first coupled into an optical fiber bundle, which was divided into two rectangular strips (20 mm × 1.25 mm) at the output end. The incident pulse fluence on the tissue surface was controlled to be around 10 mJ/cm^2, which was less than the safety limit set by the American National Standards Institute (20 mJ/cm^2) at this wavelength. A linear-array transducer containing 256 elements (LZ250, Visualsonics Inc.) was used to detect the PA signals. Thus, each laser pulse

generated a two-dimensional (2D) PA image. With a central frequency around 21 MHz and a 78% one-way bandwidth, this transducer array had an axial resolution of 86 μm. With a size of 23 mm × 3 mm and a cylindrical focus at 15 mm, this transducer array provided a lateral resolution of 119 μm and an elevational resolution of 1237 μm.

Figure 4.13(b) shows a schematic of saline injection in phantom experiments. A silicone tube (300 μm inner diameter) filled with blood was used to mimic the blood vessel. The blood was pumped into the tube through a syringe, and the flow speed was controlled by a syringe pump. A second syringe was employed to perpendicularly inject saline solution into the tube. The distance between the injection point and the center of the field of view was set to 15 cm so the injection disturbance to the flow was minimized.

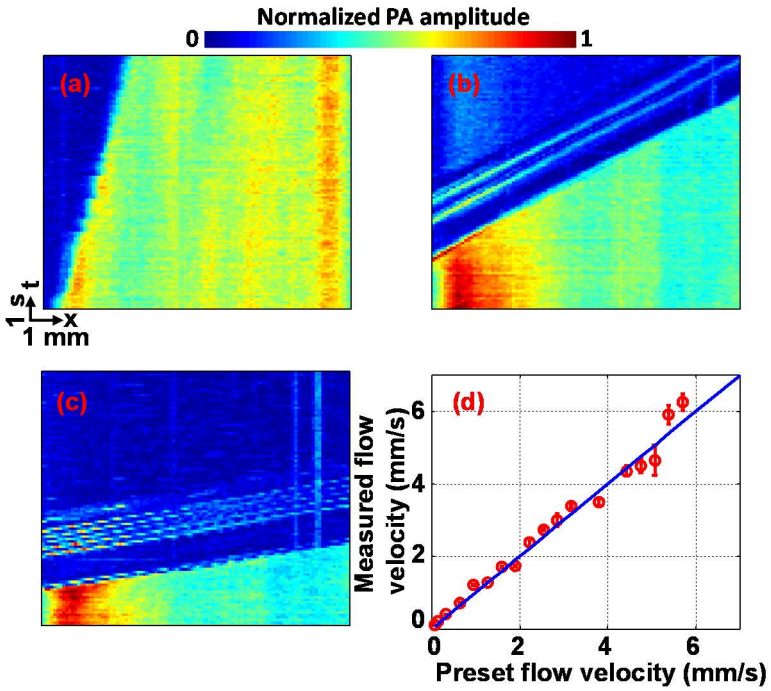

Figure 4.15 Phantom experiments. Time course of the photoacoustic (PA) amplitude of the blood with flow velocity at 0.2 (a), 1.3 (b), and 4.5 mm/s (c) in a vessel. (d) Measured flow velocity versus preset flow velocity. Red circles, experimental measurement; Blue line, ideal fit if the measured and preset velocities are identical.

The flow velocity was extracted in three steps from the PA signals of the saline-blood interface (SBI). First, the whole process of the interface propagation through the field of view (FOV) of the transducer array was monitored. At each time point, a 2D image of the blood vessel was acquired and then converted to a one dimensional (1D) amplitude image via the Hilbert transformation, followed by taking the absolute value and then taking the peak amplitude. By piecing together all the 1D images at consecutive time points, a final 2D amplitude image of the SBI was achieved, as shown in Figure 4.14(a). Note that the x-axis is the displacement along the blood vessel and the y-axis is time. Second, at each time point, the 1D PA amplitude of the phantom blood vessel was fitted by an error function to extract the location of the SBI, as indicated by the mean value of the error function in Figure 4.14(b). Last, by tracking the SBI along the phantom blood vessel, we calculated the blood stream flow velocity. As shown in Figure 4.14(c), although only two measurements of the SBI sufficed to calculate the blood flow velocity, multiple measurements could improve the accuracy by linear fitting.

Results Phantom experiments were first performed to demonstrate the capability of our method in flow measurement. To confirm that our method can measure blood flow in biological tissue at depths of the optical diffusive regime, fresh chicken breast tissue with a thickness of ~2 mm was laid atop the phantom blood vessel. Figures 4.15(a-c) show three representative 2D amplitude images of the SBI, with blood stream flow velocities of 0.2, 1.3, and 4.5 mm/s. Because of the strong optical absorption difference between blood and saline, SBIs were imaged by PAT with high contrast, as shown in Figures 4.15(a-c). Thus, by linear fittings of the SBI spatial-temporal locations, our measured blood flow velocities agreed well with the preset values, as shown in Figure 4.15(d). The root-mean-square error of prediction (RMSEP) was calculated to be 0.29

mm/s, indicating that our method can measure deep blood flow with high accuracy. Thus, we concluded that our method should be able to measure blood flow velocity *in vivo*.

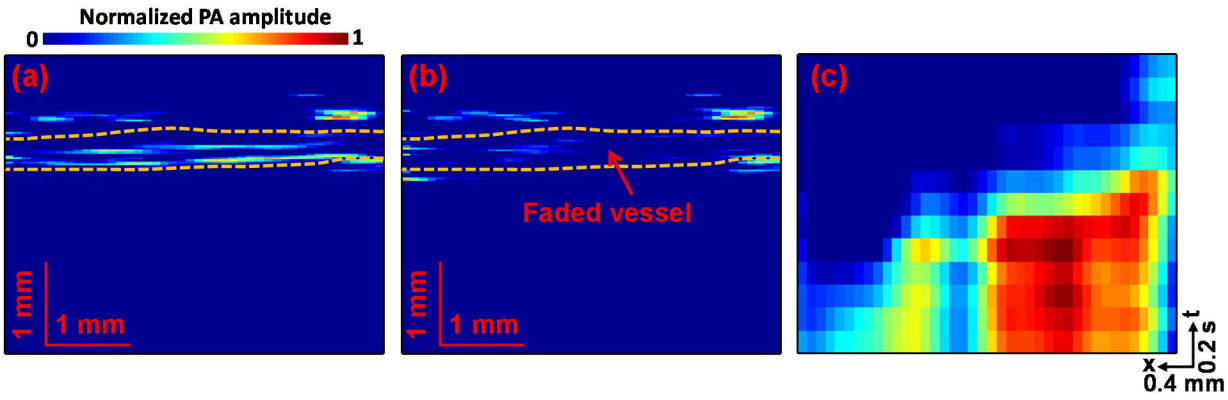

Figure 4.16 *In vivo* experiments. Photoacoustic (PA) images of the tail vein before saline injection (a) and after saline injection (b). Dashed lines indicate the vessel region. (c) Time course of the PA amplitude of the tail vein when the saline flushed in.

We then measured blood flow velocity in a mouse tail vein *in vivo* to show the detection ability of the saline-injection-based method. Again, a slice of chicken breast tissue (~1 mm) was put atop the tail vein to increase the measurement depth. Saline was injected into the tail vein with a home-made catheter to induce the SBI for blood flow measurement. The distance between the injection spot and the imaging window was ~3 cm. During the experiment, an infrared lamp kept the mouse warm, and a breathing anesthesia system (E–Z Anesthesia, Euthanex) kept the mouse motionless. All experimental animal procedures were carried out in conformity with laboratory animal protocols approved by the Animal Studies Committee of Washington University in St. Louis. As shown in Figure 4.16(a), before saline injection, the whole tail vein in the field of view (FOV) could be clearly observed. However, when the saline flushed in, there were almost no signals from the blood vessel anymore because of the low absorption of saline, as shown in Figure 4.16(b). Again, the SBI's spatial-temporal location can be clearly imaged by PAT, as shown in Figure

4.16(c). Based on the same procedure as in the phantom experiments, the blood flow velocity was quantified to be around 4.5 mm/s.

Discussions With an ~10 mm FOV along the lateral direction, the system has a frame rate of 10 Hz. Limited by the system's memory, a maximum of 1000 continuous frames can be stored. If we use the lateral resolution (119 μm) as the minimum displacement that the system can separate, the minimum flow speed the system can measure is around 119 μm/50 s = 2.38 μm/s. For the maximum flow speed, in theory it should be around 50 mm/s based on the current frame rate and FOV along the lateral direction. Here we require that the saline-blood interface be imaged twice in order to measure the flow speed, for both the minimum and maximum flow estimation.

4.3 Cuffing-based Photoacoustic Flowmetry in Humans in Depths of the Optical Diffusive Regime

Background In this section, we present a cuffing-based method to measure blood flow speed in humans. Aided by a common sphygmomanometer, PAT successfully measured blood flow in humans for the first time. This procedure has three steps. First, a window along the blood vessel of interest is imaged. Second, the blood flow upstream of the window is stopped by cuffing the blood vessel with the sphygmomanometer. A high pressure (220 mg Hg in our experiments) is maintained in the cuff for a short time (e.g., 10 seconds) until there is almost no blood left in the vessel in the imaging window. Finally, the sphygmomanometer is quickly released, and the blood flow speed is calculated by monitoring the blood wash-in process.

Methods To test our method, we employed a commercialized linear-array-transducer based PAT system (Vevo LAZR, VisualSonics, Toronto, ON, Canada), as shown in Figure 4.17(a-b). A Nd:YAG laser combined with an optical parameter oscillator provided tunable illumination

wavelengths from 680 nm to 970 nm. To achieve deep penetration, 850 nm was chosen for our experiments. The laser pulse had a width around 10 ns and a repetition rate of 20 Hz. The light was coupled to an optical fiber bundle that was divided into two rectangular fiber bundles (20 mm × 1.25 mm) with an illumination angle of 60° toward the tissue surface. The incident pulse fluence was around 5 mJ/cm^2, below the safety limit set by the American National Standards Institute for this wavelength. A 256-element linear-array-transducer, with a central frequency of around 21 MHz (one-way bandwidth, 78%) and a size of 20 mm × 3 mm, detected ultrasonic signals. The array and the fiber bundles were aligned coaxially and confocally to maximize the system's sensitivity. Because the data acquisition system contained only 64 channels, a 4:1 electronic multiplexer was used to acquire ultrasonic signals from all the transducer elements. Thus, with a 20 Hz laser, the two-dimensional frame rate was reduced to 5 Hz to obtain a full-width image. However, the frame rate could be increased up to 20 Hz with fewer receiving channels and thus a smaller field of view (FOV). In our experiments, a frame rate of 10 Hz was used with a FOV of about 12 mm × 10 mm, along the axial and lateral directions of the array, respectively.

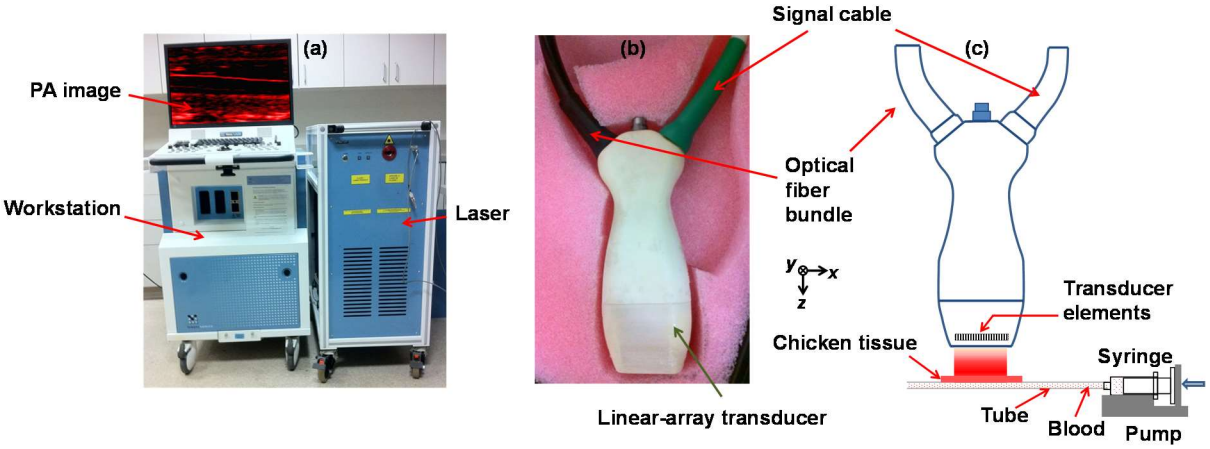

Figure 4.17 Photographs of the PAT system (a) and the linear-array-transducer (b). The workstation has a 64-channel data acquisition system, a data processing system, and an image display interface. (c) A schematic of the array in the phantom experiments.

We first conducted phantom experiments to demonstrate the feasibility of our method for measuring blood flow speed in the diffusive regime. As shown in Figure 4.17(c), to mimic a deeply embedded blood vessel, silicone tubing with an inner diameter of 300 μm (11-189-15E, Fisher Scientific, Houston, TX) was overlaid by a piece of chicken breast tissue with a 2 mm thickness. Fresh bovine blood (910, QUAD FIVE INC., Ryegate, MT) was flowed inside the tubing at different speeds controlled by a syringe pump (BSP-99M, Braintree Scientific, Braintree, MA).

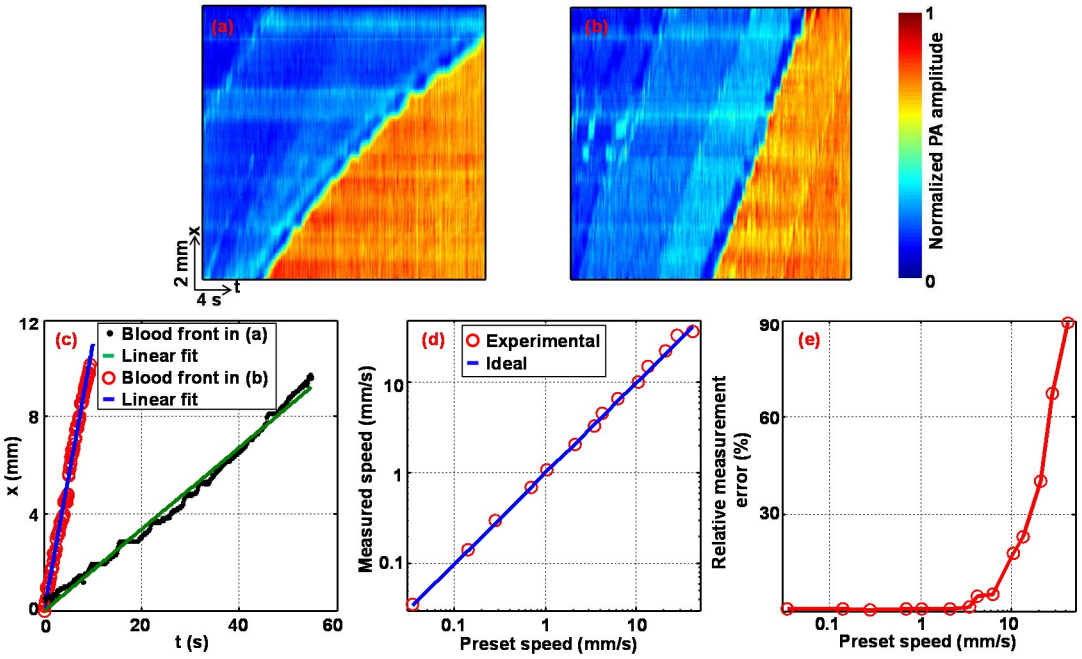

Figure 4.18 Phantom experiments. PA signal amplitude versus lateral position x and time t measured at different preset flow speeds: (a) 0.14 mm/s and (b) 1.1 mm/s. (c) Time course of the blood fronts in (a) and (b), where the slope of each linear fit directly represents the flow speed. (d) Log-log plot of the measured flow speeds versus the preset values. (e) Semi-log plot of the relative errors of the measured speeds in (d).

As shown in Figures 4.18(a)-(b), the blood wash-in process at different flow speeds could be accurately imaged. In those images, each column represents the one-dimensional PA amplitude image of the tubing in the FOV at a given time point. With increasing time, more blood flowed into the tubing in the imaging window. By quantifying how fast the blood front moved, the flow

speed could be calculated, as shown in Figure 4.18(c). As shown in Figure 4.18(d), the measured flow speed agreed well with the preset values. The measured minimum flow speed was 0.035 mm/s, which is smaller than the typical blood flow speed in capillaries in humans and also slower than the lowest flow speed that Doppler US can measure, i.e., 1 mm/s. We also tested the maximum measurable flow speed. To measure the moving speed of the blood front, we have to at least image it twice. Thus, based on current frame rate (10 Hz) and FOV (10 mm along the tubing direction), in theory our maximum measurable flow speed should be around 50 mm/s. However, as shown in Figure 4.18(e), as the preset flow speed increased, the measurement error increased as well, which was probably due to the decreased number of times that the blood front was imaged. In our experiment, the maximum measured flow speed was around 42 mm/s.

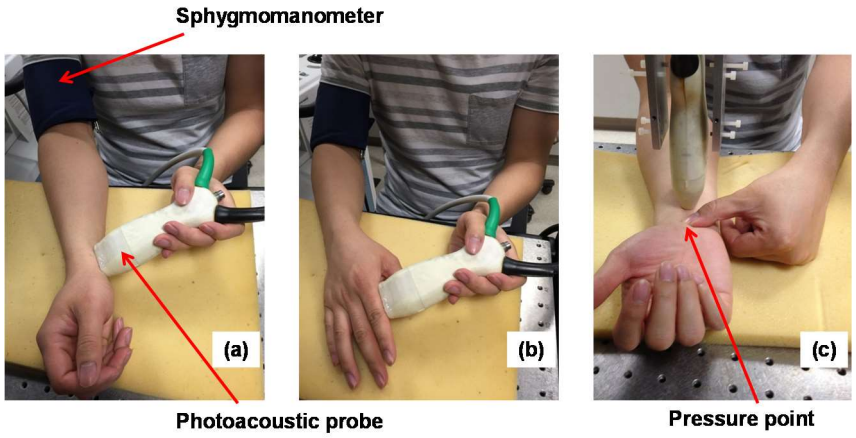

Figure 4.19 Photographs of the human experiments with imaging sites at a forearm radial artery (a), an index finger radial artery (b), and a forearm radial vein (c).

Results We then performed human experiments to show the capability of our method for measuring blood flow speed *in vivo*. As shown in Figure 4.19, there were three different imaging sites in our human experiments — a radial artery in the right forearm, a radial artery in the index finger of the right hand, and a radial vein in the right forearm. As shown in Figures. 4.19(a) and

(b), the upper arm was cuffed by the sphygmomanometer to measure the blood flow speed in the radial arteries in the forearm and finger. To measure venous flow speed, instead of cuffing, we directly compressed the radial vein close to the wrist and monitored a downstream location of the same vein, as shown in Figure 4.19(c). All methods and experimental procedures were carried out in accordance with the guidelines of The Institutional Review Board of Washington University in St. Louis. All experimental protocols were approved by The Institutional Review Board of Washington University in St. Louis.

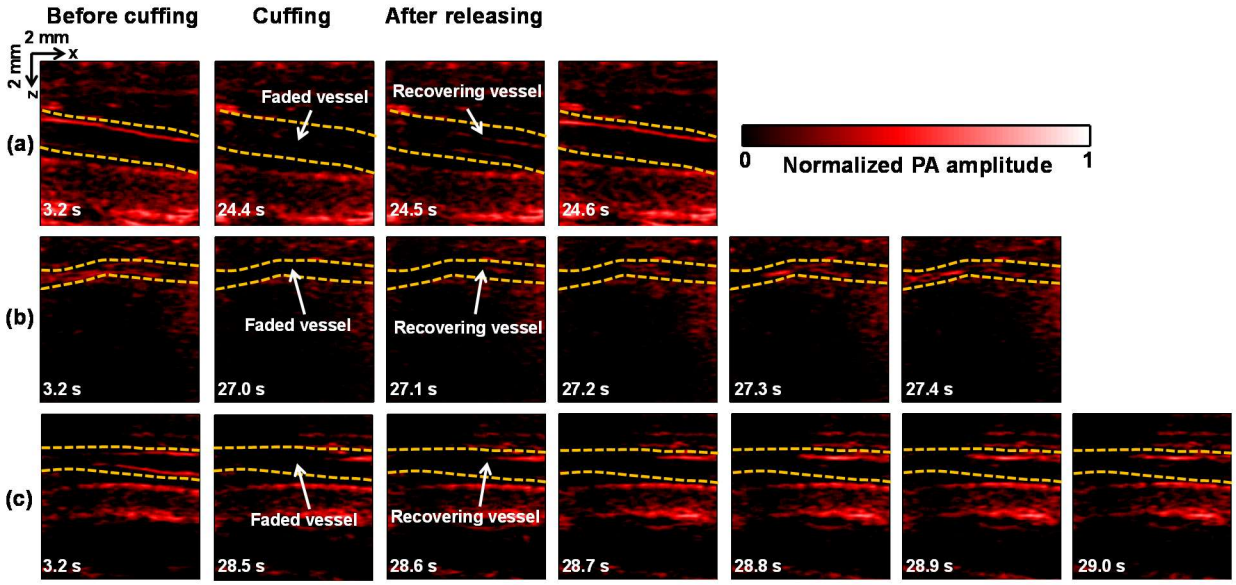

Figure 4.20 Human experiments. Representative PA images of a forearm radial artery (a), an index finger radial artery (b), and a forearm radial vein (c) before cuffing, during cuffing, and after releasing. The yellow dashed lines indicate the blood vessel regions.

As shown in Figures 4.20(a)-(c), the cuffing and releasing processes for all tested locations were clearly imaged. Before cuffing the vessel, both the top and bottom walls of the vessel could be detected. After cuffing, the blood vessel almost completely disappeared in the PA images. Once the cuff was released, the blood vessel appeared again. The recovery speed depended on the blood flow speed: For the big artery, the recovery process was the fastest; while for the vein, the process

was the slowest. Based on the same procedure as in the phantom experiments, the flow speeds in these blood vessels were calculated to be around 44 mm/s (forearm radial artery), 20 mm/s (index finger radial artery), and 10 mm/s (forearm radial vein). The measured blood flow speeds were close to the flow speeds measured with US Doppler, which were 50 mm/s, 18 mm/s, and 9.3 mm/s, respectively. Based on the experimental results, we conclude that our cuffing-based PA method can measure blood flow in humans in both big and small blood vessels.

Discussion When the blood vessel is completely cuffed, there is almost no detectable blood in the downstream but blood accumulates under pressure upstream of the cuffing spot. Thus, the initial post-release blood wash-in process is a surge, which diminishes to normal flow with increased distance from the cuffing spot. In our measurements, we sought to avoid surge effects by setting the downstream imaging locations at ~ 5 cm for the vein flow measurement and more than 30 cm for arterial measurements.

4.4 Conclusions

First, we provided a cross-correlation-based method to measure flow velocity *in vivo* by using PAM. Different from previous flow measurement methods, this method was independent of particle size. Thus, a calibration-free absolute flow velocity can be measured, including both the flow speed and direction. Taking advantage of absolute flow velocity information, we observed accurate flow velocity changes and the feature conservation nature in the vessel. With more accurate flow information, our method provides a promising tool for more accurate measurement of the metabolic rate of oxygen, and for blood disorder studies.

Second, to our knowledge, for the first time we achieved deep blood flow measurement *in vivo* with AR-PAT. SBIs were created by injecting saline into the blood vessel, and the blood flow

velocity was measured by monitoring a single SBI propagation in the blood stream. Our phantom experiments showed that we could achieve a highly accurate measurement of blood flow velocity in deep biological tissue, with a RMSEP of 0.29 mm/s. The *in vivo* mouse experiments indicated that we could potentially measure blood flow in humans. Based on saline injection, our method is particularly suitable for blood flow quantification in patients already undergoing intravenous infusion.

At last, for the first time to our knowledge, we measured blood flow speed in humans with PAT. By cuffing and releasing the targeted blood vessels, the flow information could be extracted. In phantom experiments, the minimum and maximum measurable flow speeds with the current system were experimentally quantified to be around 0.035 mm/s and 42 mm/s, respectively. We further applied our method to measure both arterial and venous flow speeds in humans. Because we used a handheld photoacoustic probe, our method can easily be used to detect blood flow speed both in the clinic and at home.

Chapter 5 Photoacoustic Tomography of Human Brain Vasculature

In this chapter, we image brains both in mice and humans. In the first section, we imaged the whole mouse brain with two systems: a ring transducer array with center frequency of 5 MHz and a linear array with 21 MHz center frequency. In the second section, we build a circular scan system with a 0.5 MHz center frequency for human brain imaging.

5.1 Photoacoustic Tomography of Mouse Brain *in Vivo*

Methods We first used a cylindrical-view PACT system for brain imaging. The system contained a 512-element full ring transducer array with a ring diameter of 25 cm. Each transducer element had a center frequency of 5 MHz and a 90% (one-way) detection bandwidth. To improve the cross-sectional imaging ability, each element was cylindrically focused to reject out-of-plane signals. The combined foci from all elements provided a central imaging region with an ~20 mm diameter and ~1 mm thickness. Strictly speaking, such a system is a circular-view system, since only a ring, not a cylinder, is used to reconstruct the image. However, by taking advantage of its cylindrical focusing capability, high-quality 2D cross sectional images are attainable. In addition, by scanning the sample or the array along the elevational direction, 3D images can be acquired. Within the imaging region, the system provided 125-250 μm transverse resolution in the circumferential direction and 1250 μm axial resolution in the radial direction. A laser operating at 1064 nm was used for illumination. An acoustic reflector was used to reflect ultrasound signals from the mouse brain to the transducer array.

We next used a 256-element linear-array-transducer, with a central frequency of around 21 MHz (one-way bandwidth, 78%) and a size of 20 mm × 3 mm, for brain imaging. Because the data

acquisition system contained only 64 channels, a 4:1 electronic multiplexer was used to acquire ultrasonic signals from all the transducer elements. Thus, with a 20 Hz laser at 1064 nm, the two-dimensional frame rate was reduced to 5 Hz to obtain a full-width image. In addition, we rotated the linear array from -40° to 40° to increase the acceptance angle for mouse brain imaging.

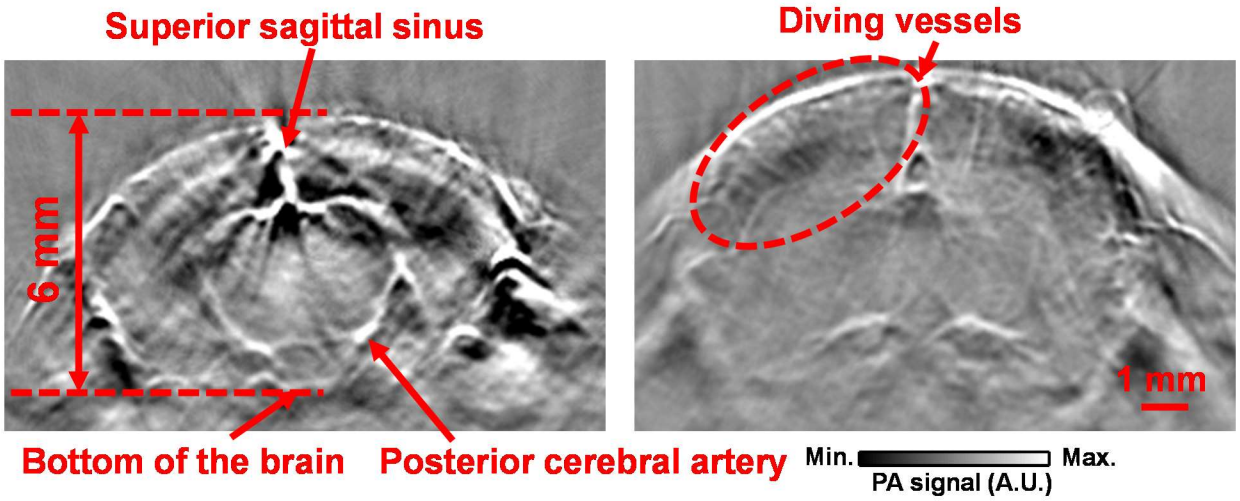

Figure 5.1 PACT of a mouse brain with a 5 MHz transducer array at two coronal planes.

Results As shown in Figure 5.1, a mouse brain could be imaged at two different coronal planes. Signature vessels can be detected, such as diving vessels, the superior sagittal sinus, and the posterior cerebral artery. In addition, the bottom of the mouse brain can also be imaged. However, because this system had poor spatial resolutions, the image contrast was not very high. One way to improve the image contrast is to employ a high frequency transducer array with a better elevational resolution. Thus, we next implemented a transducer array with 21 MHz center frequency. With this system, more blood vessels could be resolved with higher contrast, as shown in Figure 5.2.

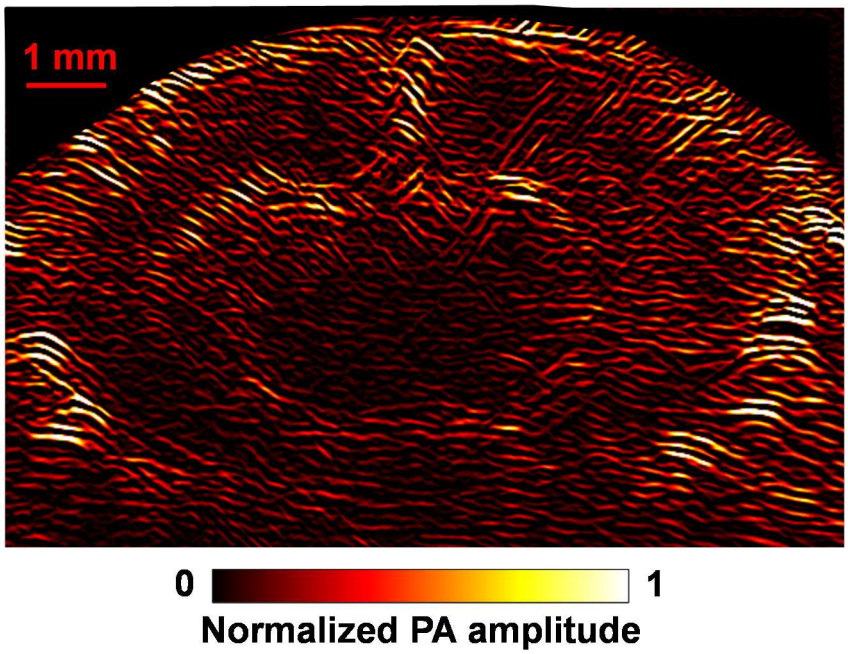

Figure 5.2 Blood vasculature imaged by a 21 MHz transducer array.

5.2 Photoacoustic Tomography of the Human Brain *in Vivo*

Background Current human brain imaging modalities include positron emission tomography (PET), functional magnetic resonance imaging (fMRI), diffuse optical tomography (DOT), and ultrasonography. However, all of them have limitations. PET requires tracers for sufficient contrast, which involves exposure to ionizing radiation. fMRI detects water and only indirectly measures brain functions, so the relationship between fMRI signals and underlying brain activities still remains unclear. In addition, both PET and fMRI employ nonportable imaging equipment and are very expensive. As a pure optical imaging modality, DOT suffers from a very low spatial resolution because of the strong optical scattering in both the skin and skull. Ultrasonography does not have the optical scattering problem, but suffers strong attenuation and distortion from the skull. Thus it can image only the pediatric brain before the closure of fontanelles. Moreover, the imaging

contrast of ultrasonography is based on acoustic scattering, which is low in soft brain tissue. Collectively, a complementary brain imaging modality is still desired.

Combining the advantages of optical excitation and acoustic detection, PAT is a promising alternative brain imaging tool. Compared to the brain imaging modalities listed above, PAT has four advantages: (1) Its contrast is based on intrinsic optical absorption, so it does not require ionizing radiation. (2) It detects the rich optical absorption contrast of biological tissue (such as hemoglobin, lipid, and DNA), and thus can perform both structural and functional imaging. (3) Because acoustic scattering is much lower than optical scattering in biological tissue, PAT can maintain a high resolution in deep tissue. (4) Although PAT also suffers acoustic attenuation and distortion due to the skull, it has only a one-way problem, unlike ultrasonography.

Previously, we reported that both a graphite phantom and a canine brain were imaged by PAT through a human skull. In that work, many artifacts appeared, which significantly reduced the image quality of the target. In reality, besides the targeted brain vessels, which are below the skull, there are also blood vessels above the skull (e.g., the vessels in the scalp). In the following text, for simplification, we use superficial blood vessels (SBVs) and cortical blood vessels (CBVs) to represent the blood vessels above and below the skull. It is estimated that PA signals generated from SBVs are at least 50 times stronger than those from CBVs, due to light attenuation. If we take into account the strong acoustic attenuation of the skull, the final detected signals of SBVs would be more than 100 times stronger than those of CBVs, even if we use, for example, a transducer with a center frequency at 0.5 MHz. How to mitigate those unwanted but strong superficial signals becomes a big roadblock for human brain imaging.

In this section, we introduce an acoustic blocker to remove the interfering signals generated from the SBVs. We show that, with the acoustic blocker, the CBVs below the skull can be imaged with almost no interference from the skull and the SBVs. In addition, skin from a monkey's head and a piece of chicken breast tissue were used to mimic real human head skin and the attached tissues. We show that the CBVs can be recovered, even with the thick tissue, skin, and SBVs. Our experimental results suggest that PAT can be used as a potential human brain imaging modality.

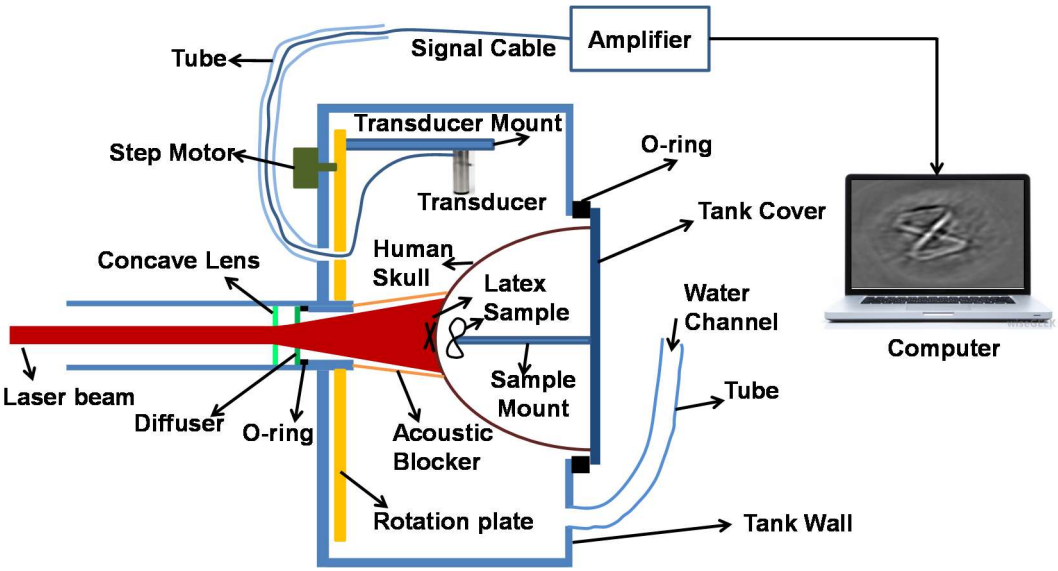

Figure 5.3 Schematic of human brain imaging system.

Methods A system schematic is shown in Figure 5.3. A Q-switched Nd: YAG laser (PRO-350-10, Newport, Irvine, CA) operating at 1064 nm was the light source. The laser pulse had a pulse width of 6.5 ns and a repetition rate of 10 Hz. After being expanded by a concave lens (LC2679-C, Thorlabs, Newton, NJ) and homogenized by a ground glass diffuser (DG10-1500, Thorlabs, Newton, NJ), the laser pulses finally illuminated the target. Latex cords (1775T21, McMaster-Carr, Elmhurst, IL) were used as the test targets. Some of them were placed above the human skull (Skull Unlimited International Inc. Oklahoma City, OK), mimicking the SBVs, while the others

were below the skull, mimicking the CBVs. The optical fluence at the skull surface was estimated to be 36 mJ/cm^2, which was smaller than the American National Standard Institute (ANSI) limit (100 mJ/cm^2). A 0.5 MHz ultrasonic transducer (V318-SU, Olympus, Waltham, MA) with a bandwidth of 70% detected the signals. The transducer was mounted on a rotation plate, which was driven by a step motor. Signals at 400 angles were detected by the transducer, amplified by an amplifier, and finally directed to a data-acquisition (DAQ) card (ATS9462-001-USD, ALAZAR TECHNOLOGIES INC., Pointe-Claire, CANADA). The transducer, skull, and phantoms were all immersed in water, which was contained in a home-made tank with O-rings for water sealing.

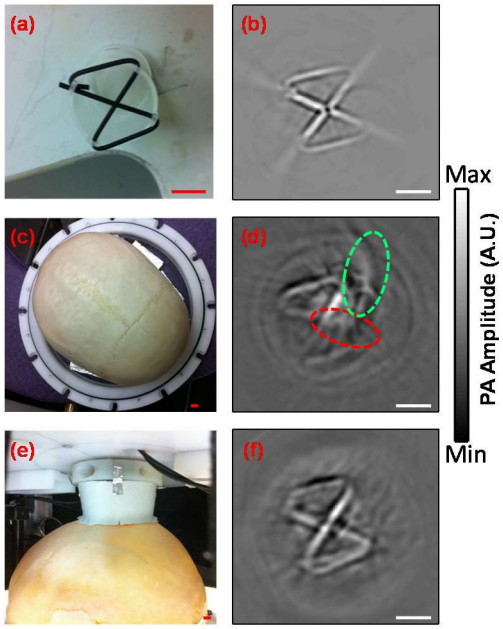

Figure 5.4 Cortex blood vessel (CBV) phantom experiment. (a) Photograph of the latex rubber phantom to mimic CBVs. (b) PACT image of the pure phantom. (c) Photograph of the skull with phantom inside. (d) PACT image of the phantom with skull. (e) Photograph of the acoustic blocker. (f) PACT image of the phantom with skull with the acoustic blocker. The dashed circles in (d) highlight the artifacts removed by the acoustic blocker, as shown in (f). Scale bars: 1 cm.

As shown in Figure 5.3, a styrofoam cup was used an acoustic blocker to reduce the interfering signals from the SBVs. The bottom of the cup was cut off for light transmission. Since the styrofoam contains a myriad of air cavities, it acts mainly as an acoustic reflector. Thus, by properly positioning the acoustic blocker, most of the interfering signals from the SBVs were reflected by the cup, while the signals from CBVs were unaffected. Ultimately, the transducer received very few interfering signals but most of the targeted signals, and a much cleaner image of the CBVs was achieved.

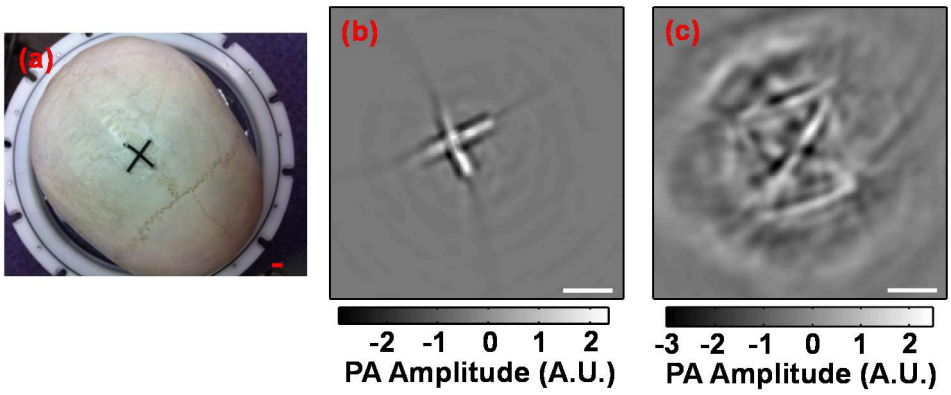

Figure 5.5 Superficial blood vessels (SBV) phantom experiment. (a) Photograph of the skull with SBVs. (b) PACT image of the SBV. (c) PACT image of the CBVs inside the skull with SBVs with the acoustic blocker. Scale bars: 1 cm.

Results Figure 5.4(a) shows a photograph of the CBVs phantom used in the experiment. The diameter of the latex rubber is 1.5 mm. We first acquired a control image without putting the phantom below the skull, as shown in Figure 5.4(b). Based on Figure 5.4(b), we can see the whole phantom can be successfully detected, and there is no distortion in the reconstructed image. However, after adding the skull (Figure 5.4(c)), three obvious differences can be observed in the reconstructed image (Figure 5.4(d)). First, many artifacts (e.g., artifacts inside the green-dotted oval) appeared. Second, the whole image became distorted, which can be clearly observed,

especially in the red-dashed oval area. Third, the image intensity was much less homogenous. The intensity in some parts of the phantom is much stronger than in other parts, and some parts of the phantom have almost disappeared in the image. Although these three differences are all caused by the skull, they have different origins. The first difference, the strong artifacts, stems from the light absorption of the skull. As mentioned above, the skull decreases the signals from the CBVs more than 100 times. Thus, in order to maintain a similar signal-to-noise (SNR) in Figure 5.4(d) as in Figure 5.4(b), incident pulses with much higher energy were applied (e.g., 100 times). Thus, although the absorption coefficient of the skull at 1064 nm is very small, the specific optical energy deposition can be high, and so can the PA signals. The distortion and inhomogeneity problems, the last two differences, are both mainly caused by the acoustic heterogeneity of the skull, which affects the local speed of sound, scattering, and absorption. In addition, the interfering signals can also cause inhomogeneity. Figure 5.4(e) shows the acoustic blocker used in our experiments. The acoustic blocker was squeezed tightly against the skull to reduce possible gaps. Figure 5.4(f) shows the reconstructed image after implementing the acoustic blocker. Compared to Figure 5.4(d), the artifacts are significantly reduced.

As shown in Figure 5.4(d), even with only the skull, the image quality is significantly reduced. However, in reality, there are always some SBVs above the skull, which will worsen the already bad situation. To mimic the SBVs, we pasted a latex rubber cross on the skull, as shown in Figure 5.5(a). As expected, we could detect only the SBVs without using an acoustic blocker (Figure 5.5(b)), because of the strong optical and acoustic attenuation of the skull. However, after we added the same acoustic blocker as in the first experiment, the SBVs almost completely disappeared in the image, and the targeted CBVs showed up again. Compared to Figure 5.4(f), although the whole phantom can also be clearly identified in Figure 5.5(c), the image quality is lower in Figure 5.5(c),

and the artifacts are stronger. Our results show that with the presence of both the SBVs and CBVs, PAT can still get a very good image of the CBVs.

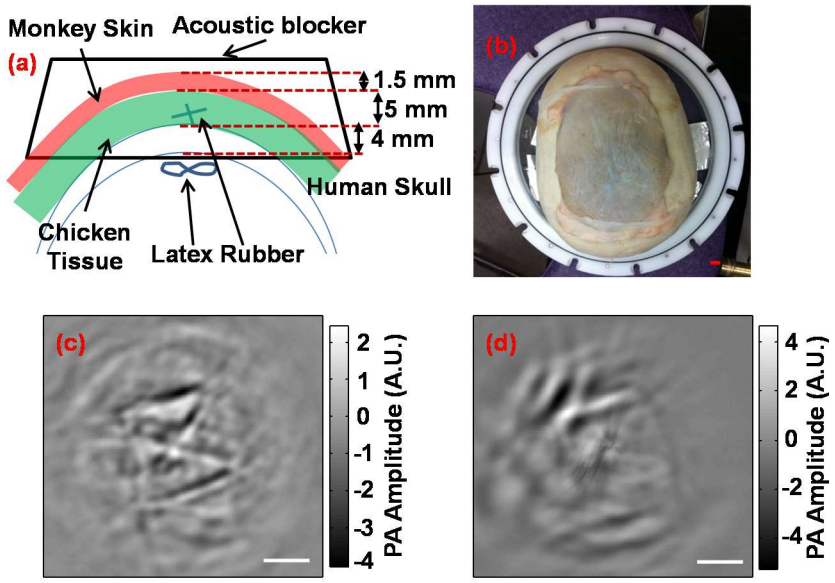

Figure 5.6 Phantom experiment with SBVs, chicken tissue, and monkey skin. (a) Schematic of the complicated phantom. (b) Photograph of the phantom. (c) PACT image of the CBVs with only SBVs and monkey skin. (c) PACT image of the CBVs with SBVs, chicken tissue, and monkey skin. Scale bars: 1 cm.

To further mimic a real human head, we added monkey skin and a piece of chicken breast tissue on top of the skull, as shown in Figure 5.6(a). The SBVs were still there, between the chicken tissue and the skull. The monkey skin was 1.5 mm thick, and the chicken tissue was 5 mm thick, very similar to the thicknesses of the human skin and scalp. The human skull was measured by X-ray CT, and its thickness was about 4 mm at the top. Thus, the total sample thickness above the CBVs was about 10.5 mm. Figure 5.6(b) shows images of the monkey skin, chicken tissue, and the human skull. Step by step, we first imaged the phantoms with only the monkey skin (i.e., without the chicken tissue), as shown in Figure 5.6(c). The whole "CBVs" are still very clearly in the image. As shown Figure 5.6(d), the whole CBVs still can be identified, although the contrast is much lower.

5.3 Conclusions

In this chapter, we successfully imaged a whole mouse brain. Many representative blood vessels could be detected, as well as the deepest portion of the brain. We also built a system for human brain imaging. With an acoustic blocker, the SBVs' signals could be successfully removed in the phantom experiments.

Chapter 6 Photoacoustic Imaging of Melanoma in Patients

In this chapter, we aim to image melanoma and measure melanoma depth in patients. We first developed handheld PAM to detect melanoma and determine tumor depth in nude mice *in vivo*. Compared to our previous PAM system for melanoma imaging, a new light delivery mechanism is introduced to improve light penetration. We show that melanomas with 4.1 mm and 3.7 mm thicknesses can be successfully detected in phantom and in *in vivo* experiments, respectively. To solve the imaging speed problem, we then applied a linear-array-based photoacoustic probe to detect melanin-containing melanoma tumor depth and volume in nude mice *in vivo*. This system can image melanomas at five frames per second (fps), which is much faster than our previous handheld single transducer system (0.1 fps). We first theoretically show that, in addition to the higher frame rate, almost the entire boundary of the melanoma can be detected by the linear-array-based probe, while only the horizontal boundary could be detected by the previous system. Then we demonstrate the ability of this linear-array-based system in measuring both the depth and volume of melanoma through phantom, *ex vivo*, and *in vivo* experiments. The volume detection ability also enables us to accurately calculate the rate of growth of the tumor, which is an important parameter in quantifying the tumor activity. In the end, we applied this linear array probe to image melanoma and quantify melanoma depth in patients. Work in this chapter has been published in Optics Letters and Journal of Biophotonics [108, 109].

6.1 Handheld Photoacoustic Microscopy to Detect Melanoma Depth *in Vivo*

Background Melanoma is a malignant tumor of melanocytes. It is now the fifth most common cancer in the United States [110, 111], where there were about 76,690 men and women diagnosed with melanoma in 2013 alone. Although melanoma accounts for less than 5% of all skin cancers, it causes more than 75% of deaths related to skin cancer. In addition, the incidence of melanoma is increasing faster than that of any other cancer. Consequently, there is an increased demand for accurate diagnosis, prognosis, and treatment of melanoma.

The thickness of a melanoma is a critical parameter for determining definitive treatment and prognosis [112]. Based on its thickness, the tumor (T) classification in the tumor-node-metastasis (TNM) staging system can be further divided into T1 (≤ 1.0 mm), T2 (1.01-2.0 mm), T3 (2.01-4.0 mm), and T4 (>4.0 mm). As the thickness increases, so do the chances for developing metastatic disease, and thus, disease mortality. Current diagnoses are dependent upon clinical suspicion, subsequent biopsy, and histologic examination. It has been shown that clinical examination alone may miss certain tumors, and conversely, many benign lesions may be unnecessarily biopsied [113, 114]. In trained hands, the use of handheld dermoscopy in the clinic has aided in the diagnosis of melanoma by facilitating the evaluation of surface characteristics of pigmented lesions [115]. It does not, however, enable the determination of tumor thickness and vertical growth of the melanoma, which are important tumor characteristics when it comes to determining surgical treatment. In fact, the surgeon is often met with the confounding situation where a pigmented lesion may be partially biopsied and the diagnosis of melanoma is made. Consequently, the true tumor depth may not be determined due to sampling only part of the tumor, leading to an inaccurate measurement. Thus, a wide local excision (WLE) based upon a provisional tumor depth may not be appropriate, and a second surgery

may be required to adequately treat the tumor. Thus, a precise *in vivo* measurement of tumor depth, prior to definitive surgery, would facilitate appropriate patient treatment and help avoid further surgeries.

In the past few years, several noninvasive imaging techniques have been developed for melanoma diagnoses. However, all of them have limitations. Optical methods, such as dermoscopy [115], total-body photography (TBP) [116], optical coherence tomography [117], scanning confocal microscopy [118], and two-photon microscopy [119], do not have sufficient penetration to determine melanoma depth because they can image only in the ballistic regime. High frequency ultrasound can provide deeper penetration than optical methods [120]. However, because there is often no sufficient difference in acoustic impedance between melanoma and normal tissues, the image contrast for melanoma is poor. Magnetic resonance imaging (MRI) and positron emission tomography (PET) have also been used in melanoma diagnoses [121, 122]. However, they are both expensive and have poor resolution in the skin. Meanwhile, PET has to use tracers for sufficient contrast and can only detect tumors as large as ~1 cm in dimension, which encompasses only a tiny set of T4 primary melanomas and misses all T1–T3 ones.

Recently, photoacoustic microscopy (PAM) has shown strong ability in detecting skin vasculatures with high contrast and deep penetration. In PAM, short laser pulses illuminate the object. Following the absorption of photons, ultrasonic waves are induced thermoelastically through the photoacoustic (PA) effect. Because melanin in most melanomas has a very broad and strong absorption spectrum, it can be imaged by PAM with high contrast. Meanwhile, because acoustic scattering is low in the tissue, high resolution can be achieved with deep penetration.

Previously, we reported that cutaneous pigmented lesions, melanoma, and the surrounding vasculature could be successfully detected by using dual-wavelength PAM [123]. In that study, light was transmitted through the whole melanoma, resulting in a high attenuation, with only very few photons reaching the base

of the melanoma (true tumor depth). In the end, PA signals were very strong from the surface of the tumor but very weak from the deepest portion. The experimental results showed that a melanoma phantom with a maximum thickness of 1.27 mm could be imaged, which covered only the T1 classification. Using a similar configuration, other studies on melanoma detection can be found elsewhere. In this report, we describe a new PAM system with more efficient light illumination. By allowing light to bypass the center of the tumor, more photons reach the inferior depth of the melanoma. Equally important, this system is designed to be handheld, facilitating clinical usage.

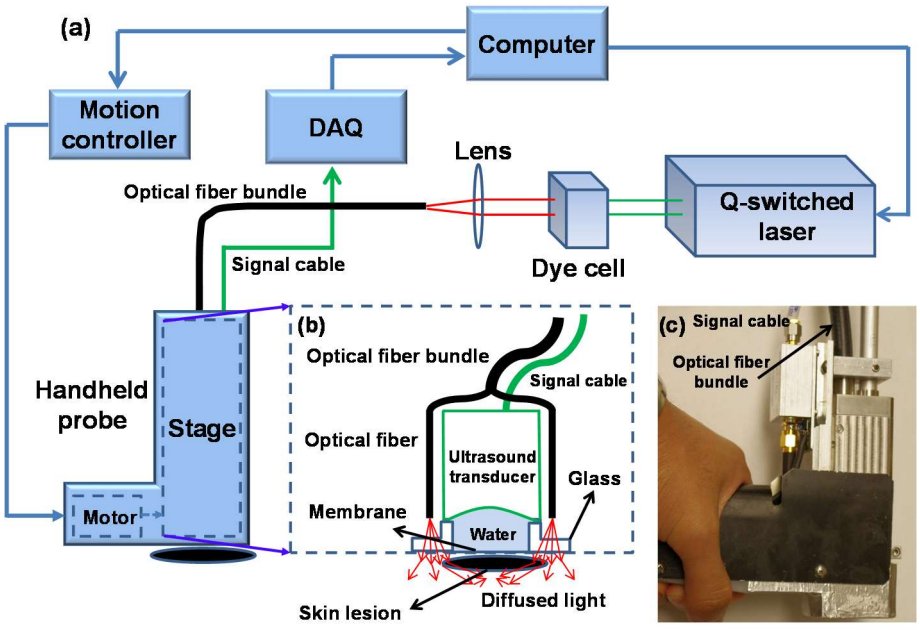

Figure 6.1 Experimental handheld PAM system. (a) Schematic of the handheld PAM system. (b) Components held by the translation stage in the handheld probe. (c) A photograph of the handheld probe.

Methods Figure 6.1(a) shows a schematic of the handheld PAM system. A Q-switched pulsed laser (Brilliant B, Quantel, Les Ulis, France) generates light at 532 nm at 10 Hz as the input for the dye cell. The output light of the dye cell is at 650 nm wavelength, where melanoma has high absorption, but both blood and water have low absorption. A lens couples the free-space light into an optical fiber bundle (LightGuideOptics, Rheinbach, Germany), with output fibers arranged in a circle around a focused

ultrasonic transducer (IS2502HR, CTS Valpey, Elkhart, Indiana). Compared to our previous PAM system, the light is delivered into the tissue normally instead of obliquely. Thus, the light propagates around the melanoma instead of going through it. Since the surrounding tissue has high optical scattering but low absorption, light reaching the bottom boundary of the melanoma is increased. The incident beam has an annular shape with 8 mm inner and 20 mm outer diameters. The optical fluence on the skin surface was estimated to be 15 mJ/cm^2, which was smaller than the American National Standard Institute (ANSI) limit (20 mJ/cm^2). The transducer, with 25 MHz central frequency and 100% nominal bandwidth, detects the PA signals. The focal length and diameter of the detector are 12.7 mm and 6.4 mm, respectively, yielding a numerical aperture (NA) of 0.25. Both the optical fibers and transducer are fixed on a motorized translation stage (Figure 6.1(b)). Each laser pulse generates a one-dimensional depth-resolved image (A-line). A two-dimensional cross sectional image is acquired by linear scanning of the region of interest. As shown in Figures 6.1(a) and (b), the motor, translation stage, ultrasonic transducer, and optical fibers are all incorporated in a handheld probe for easy operation. A photograph of the handheld probe is shown in Figure 6.1(c).

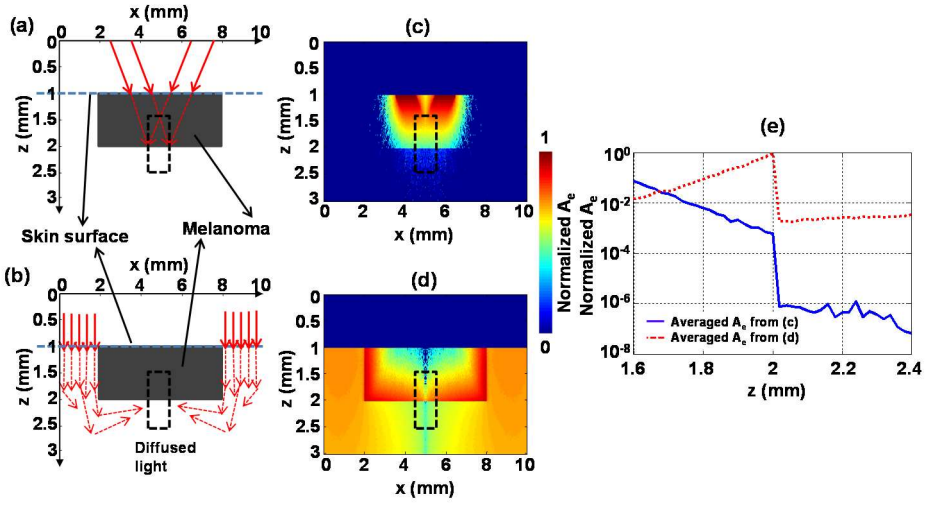

Figure 6.2 Monte Carlo simulations of the old and new PAM systems for melanoma imaging. Melanoma phantom and light illumination methods used in the simulations of the old (a) and new (b) systems. The red arrows show the incident angles and

areas of the light used in the Monte Carlo simulations. Specific heat absorption (A_e) distributions in the old (c) and new (d) PAM systems with the same incident energy. (e) Averaged A_e in the black-dashed-square areas (shown in (a-d)) at the bottom boundary of the melanoma phantoms in (c) (blue line) and (d) (red dotted line) showing that the melanoma is much more strongly illuminated at the bottom boundary using the new PAM system.

Results We use Monte Carlo simulations to show the advantage of the new light illumination mechanism. Figure 6.2(a) represents the old light illumination mechanism (hereinafter referred to as case 1). The incident angle was set to 45°, which was typical in the previous PAM system. Figure 6.2(b) shows the new light illumination mechanism (hereinafter referred to as case 2). In both simulations, the same incident energies were used. The same melanoma phantom, with 1 mm thickness and 6 mm diameter, was used in both simulations. The simulation parameters (absorption coefficient of the melanoma phantom, 70 cm^{-1}; absorption coefficient of the background, 0.1 cm^{-1}; scattering coefficients of the melanoma phantom and background, 100 cm^{-1}; scattering anisotropy of the melanoma phantom and background, 0.9) were selected based on normal tissue optical properties at 650 nm wavelength. As shown in Figure 6.2(c), in case 1, the specific optical absorption (A_e) decreases sharply in the melanoma phantom in the depth direction. However, as shown in Figure 6.2(d), in case 2, A_e actually increases in the melanoma phantom in the depth direction. As shown in Figures 6.2(a-d), the same black-dashed-square area was chosen to calculate an average A_e at the bottom boundary of the melanoma phantoms for comparison between case 1 and case 2. The average A_e is shown in Figure 6.2(e). Although the average A_e at the bottom boundary of the melanoma in the black-dashed-square area was maximized by aligning the light beam in case 1 (shown in Figure 6.2(a)), it is still 1660 times weaker than that in case 2. In both thermal and stress confinements, the PA signal is proportional to A_e. Thus, the PA signal in case 2 is 1660 times stronger than that in case 1. Because the light delivery is the only difference between the systems, their noise levels should be the same. Thus, the corresponding signal-to-noise ratio of the melanoma at the bottom boundary in the black-dashed-square

area in case 2 is 1660 times greater than that in case 1. The results show that, with the new illumination mechanism, the bottom boundary of the melanoma can be much more sensitively detected.

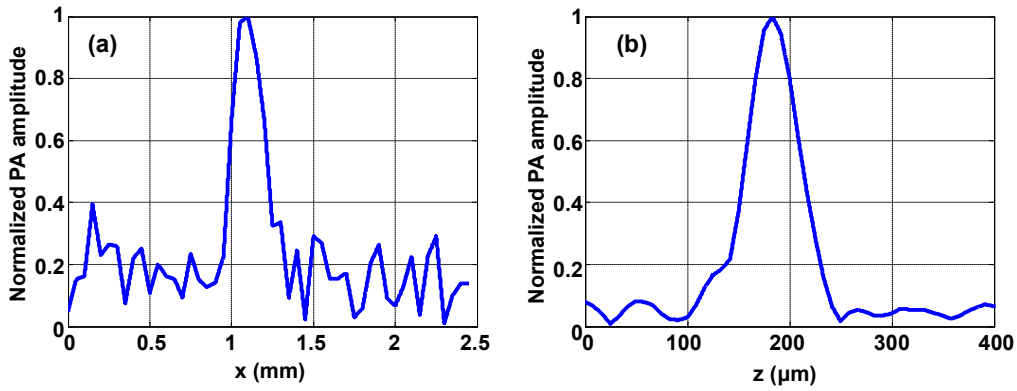

Figure 6.3 Spatial resolutions of the current PAM system. PA amplitudes in the lateral x (a) and axial z (b) directions. The full widths at half maximum are 230 μm in (a) and 59 μm in (b).

We first used a human hair as a line target to measure the lateral resolution of this handheld PAM system. As shown in Figure 6.3(a), the full width at half maximum (FWHM) of the line spread function indicates a lateral resolution of 230 μm. Because of the large thickness of the hair (80 μm), the measured lateral resolution is slightly larger than the theoretical value ($0.72\lambda_0/NA = 173$ μm, where λ_0 is the center acoustic wavelength of the transducer). We next used a thin ink layer to measure the axial resolution. Taking the FWHM of the PA amplitude in the axial direction, we estimated the axial resolution as 59 μm (Fig. 3(b)), which is close to the theoretical value ($0.88v_s/\Delta f = 53$ μm, where v_s is the sound speed in soft tissue, and Δf is the frequency bandwidth of the transducer).

Phantom experiments were conducted to demonstrate the ability of the handheld PAM system to measure deep melanomas. Three different diameters (7 mm, 9.5 mm, and 14 mm) of melanoma phantoms were prepared with varied thicknesses, shown in Figures 6.4(a)-(c). All the phantoms were made from a black ink and gelatin mixture, which had an absorption coefficient of 70 cm^{-1} at 650 nm, close to the real melanoma absorption coefficient. The background was made of a gelatin and intralipid mixture with a high

scattering coefficient to mimic real tissue. As shown in Figures 6.4(a)-(c), our handheld system successfully detected both the top and bottom boundaries of all the melanoma phantoms. The maximum and minimum detected thicknesses of the phantoms were 0.7 mm and 4.1 mm, respectively. Thus, melanoma phantoms with all the T-classifications in the staging system have been measured. Figure 6.4(d) shows that our measured thicknesses agreed well with the preset values. Thus, the handheld PAM system can image deeply seated melanoma phantoms with high accuracy.

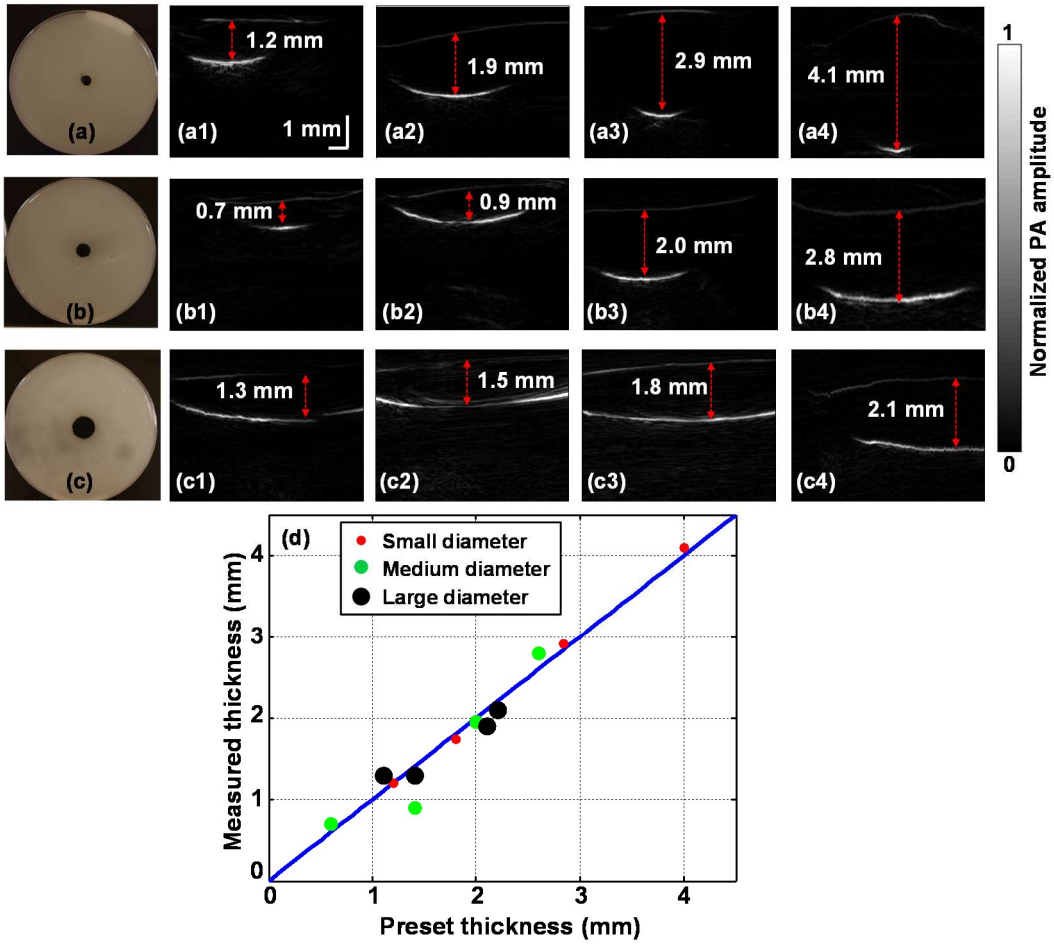

Figure 6.4 Handheld PAM of melanoma phantoms. Photos of melanoma phantoms with different diameters ((a), 7 mm; (b), 9.5 mm; and (c), 14 mm). (a1-a4), (b1-b4), and (c1-c4): PAM images of different thicknesses of melanoma phantoms with the same diameter as in (a), (b), and (c), respectively. (d) Measured thicknesses of melanoma phantoms versus preset thicknesses.

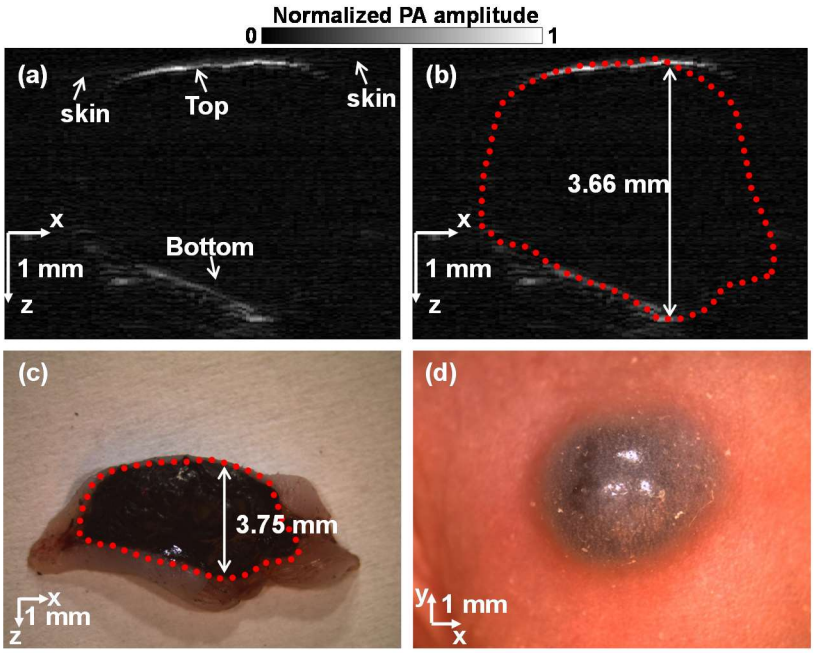

Figure 6.5 Handheld PAM of melanoma in a nude mouse *in vivo*. (a) PAM image of the melanoma clearly showing both the top and bottom boundaries. The red dots outline the melanoma according to the shape of the excised melanoma (red dots) in its photograph (b). Photograph of the melanoma taken *in vivo* (c).

We also imaged mice with melanoma to show the *in vivo* detection ability of the handheld PAM system. Here we focused only on imaging deep melanoma to show the advantage of the new PAM system over our previous system. Melanoma B16 cells were subcutaneously injected into a nude mouse on the dorsal side (Hsd:Athymic Nude-Foxn1NU, Harlan Co.; body weight: 20 g) to grow melanoma in the skin. All experimental animal procedures were carried out in conformity with the laboratory animal protocol approved by the School of Medicine Animal Studies Committee of Washington University in St. Louis. During image acquisition, the animal, warmed by an infrared lamp, was kept motionless using a breathing anesthesia system (E-Z Anesthesia, Euthanex). Figure 6.5(a) shows that a melanoma with 3.66 mm thickness was imaged by our handheld system. Both the top and bottom boundaries of the melanoma and the skin surface can be clearly seen. Shown in Figure 6.5(b), the real thickness of the melanoma was measured to be 3.75 mm after excision, which is very close to our noninvasive measurement. A photograph

of the melanoma *in vivo* is shown in Figure 6.5(c). Therefore, the handheld PAM system can accurately detect the depth of deeply seated melanoma *in vivo*.

Discussion Compared to our previous PAM system for melanoma imaging, the new system can detect the depth of thicker melanomas by bypassing light around the tumor. In addition, a handheld design makes our new PAM system more suitable for clinical application. As shown in the phantom experiment, melanoma as thick as 4.1 mm can be detected, and in the *in vivo* experiment, melanoma with 3.75 mm thickness was imaged. Our measurements also show very high accuracy. As important, the improvement of the handheld system includes increasing the imaging speed. The current system employs a 10 Hz laser, which limits the imaging speed. 10 seconds are needed to scan a 10 mm length along the lateral direction with a step size of 100 μm. For clinical use, a rapid imaging system is always preferred, which can be achieved by using a pump laser with high pulse repetition rate (e.g., 1 kHz) or using a handheld linear array probe. We propose that the use of handheld PAM imaging, to aid in the determination of tumor depth, will facilitate the surgical treatment management of melanoma.

6.2 Handheld Photoacoustic Probe to Detect both Melanoma Depth and Volume at High Speed *in Vivo*

Background In the previous section, we reported that, in a murine xenograft melanoma model, tumor thickness can be accurately determined in vivo using a handheld photoacoustic probe. In that study, a single ultrasonic transducer and a 10 Hz laser were employed, limiting the imaging speed to around one frame per ten seconds. In addition, only the horizontal boundaries of the tumor could be detected due to the limited view angle of the focused transducer. To address these limitations, we next employed an ultrasonic transducer-array-based photoacoustic probe to detect melanoma depth, as described herein. The imaging speed can be increased to five frames per

second by using a 20 Hz laser. Using this probe and employing the large acceptance angle of the transducer array in the imaging plane, nearly the entire perimeter of the melanoma could be assessed. Furthermore, by simply adding a one-dimensional scanning stage, three-dimensional (3D) measurements of the melanoma could be obtained while the small footprint and convenience of the handheld device are maintained. With its ability to detect the margins in 3 axes, the array-based probe can be further used to determine the volume of a melanoma. It has been proposed that, similar to other solid tumors, melanoma volume may prove to be an excellent prognostic indicator — probably superior to Breslow's depth. In this section, we first theoretically demonstrate that the linear-array-based probe can be used to determine and measure nearly the entire melanoma boundary, while the single ultrasonic transducer-based probe can detect only the horizontal boundary. Then we experimentally prove the ability of the linear-array-based probe to measure melanomas in phantoms, *ex vivo*, and *in vivo*.

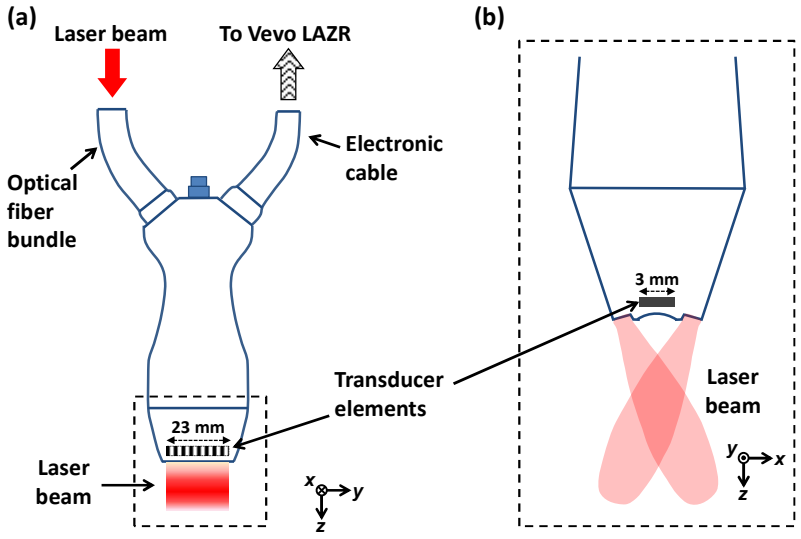

Figure 6.6 Schematic diagram of the LZ250 linear transducer array with optical fiber bundle integrated. (a) View from the elevational direction (*x*). (b) View of the transducer array's head (enclosed by a dashed box in (a)) from the lateral direction (*y*).

Method Figure 6.6 shows a schematic of the linear-array-based photoacoustic probe for melanoma imaging. A linear-array transducer (LZ250, Visualsonics Inc.), with a central frequency of 21 MHz and a 55% bandwidth, detected the photoacoustic signals. The transducer array contained 256 elements, and had a size of 23 mm × 3 mm, as shown in Figure 6.6. Each element of the array was cylindrically focused, and the focal length was 15 mm. A tunable optical parametric oscillator laser with a 20 Hz pulse repetition rate was the light source and was coupled into an optical fiber bundle. In our experiments, for melanoma imaging, the wavelength was set to 680 nm, where melanin absorbs much more strongly than blood. The optical fiber bundle and an ultrasound cable were incorporated into the same package with the linear transducer array. The beam incident angle was 30° with respect to the imaging plane. The optical fluence on the skin surface was estimated to be 10 mJ/cm^2, which was less than the safety limit set by the American National Standard Institute (ANSI) (20 mJ/cm^2) at this wavelength. Each laser pulse generated a two-dimensional image. To get a 3D PA image of the melanoma, the transducer array was scanned linearly along its elevational direction (x axis) by a motorized stage. An imaging station (Vevo LAZR, Visualsonics Inc.) displayed the photoacoustic images at five frames/second. The raw data was then exported to a computer for image reconstruction and analysis.

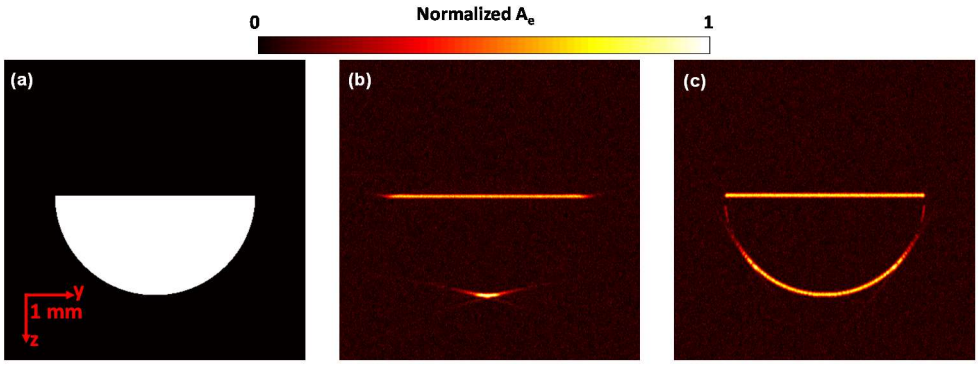

Figure 6.7 Simulation of the single focused ultrasonic transducer and the linear array. (a) Preset energy deposition distribution (A_e). Recovered A_e by the single focused ultrasonic transducer (b) and by the linear array transducer (c).

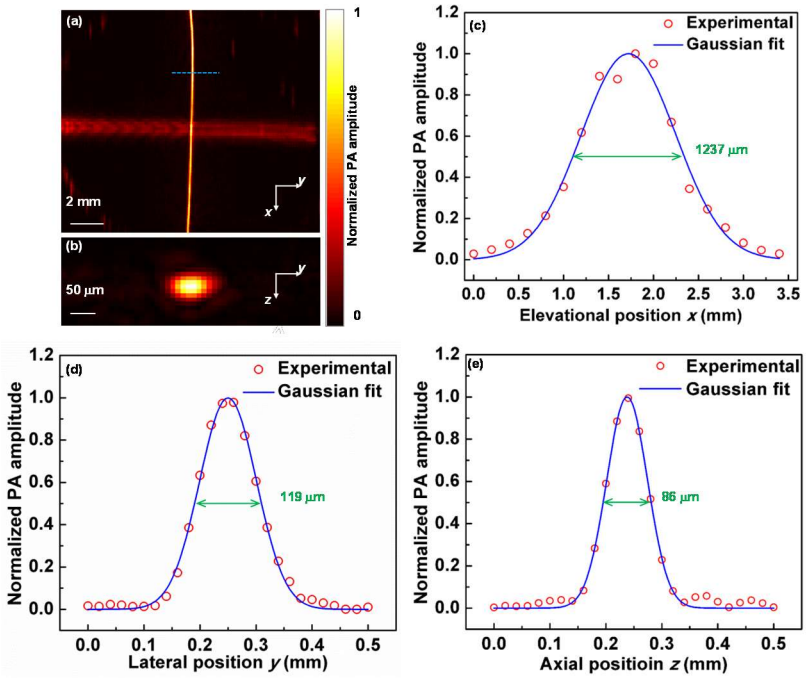

Figure 6.8 Response characteristics of the linear-array probe. (a) Maximum amplitude projection of the two crossed 6-μm-diameter carbon fibers. The diameters differ because of the directional resolution differences. (b) Cross-section image of the vertical carbon fiber along the dashed line in (a). Experimental data and Gaussian fits of the PA amplitude distributions along the (c) *x*, (d) *y*, and (e) *z* directions.

We first simulated and compared the single focused ultrasonic transducer described previously with the array used in this paper. The simulation was conducted with the k-space pseudo-spectral method, in which the acoustic wave equation was modeled and solved in k-space, utilizing the benefits of fast Fourier transformation. For the single focused ultrasonic transducer, the central frequency, bandwidth, focal length, and diameter were 25 MHz, 100%, 12.7 mm, and 6.4 mm, respectively. The parameters of the array have been described above. Figure 6.7(a) shows the melanoma mimicking target, a half disk with a radius of 2 mm. To form the image, we raster scanned the single focused ultrasonic transducer and combined the adjacent A-lines, while a time-reversal reconstruction method was used for the array system. In the time reversal method, the received pressure data were used as boundary conditions and the acoustic waves were propagated

in time-reversed order to find the pressure map at the initial time. Figure 6.7(b) shows that only the horizontal boundaries of the target are recovered by the single transducer based system. In contrast, almost the entire boundary of the target is recovered using the linear array for detection (Figure 6.7c). In addition, because the linear array scan does not need to be performed, the imaging speed can be significantly improved.

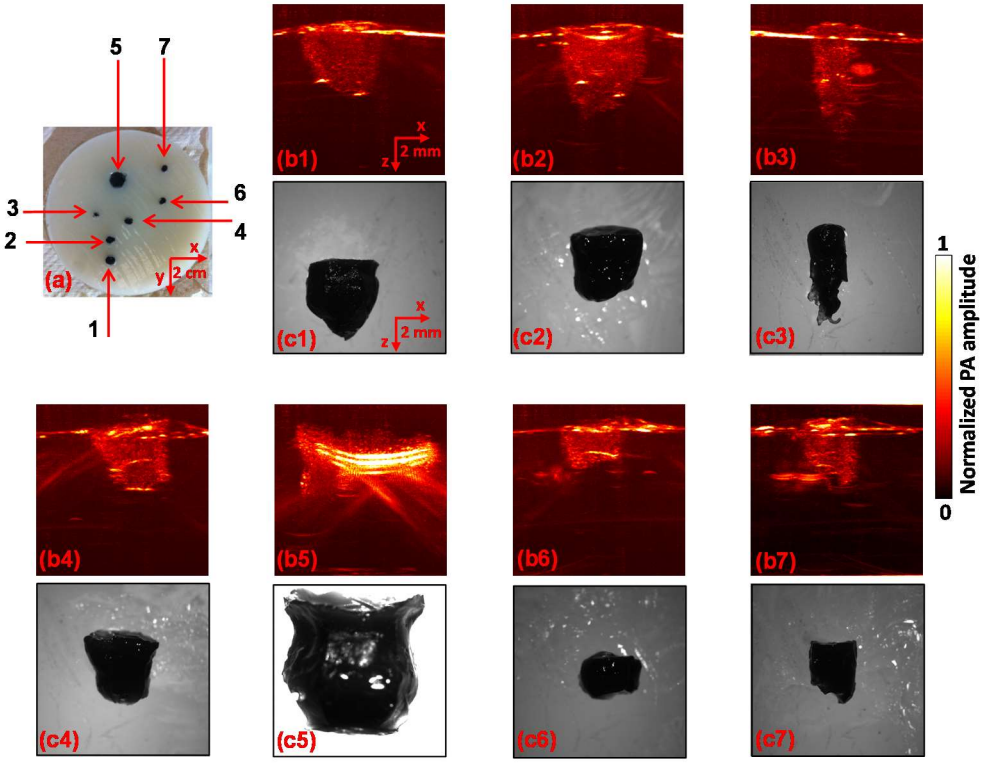

Figure 6.9 Linear-array-based PA images of melanoma phantoms. (a) Photo of the melanoma phantoms. (b1-b7) and (c1-c7) correspond to the melanoma phantoms 1-7 in (a). Melanoma phantom images acquired by PA (b1-b7) and a standard optical microscope (c1-c7).

The spatial resolution of the linear-array based PA probe was then quantified by imaging two crossed 6-μm-diameter carbon fibers, shown in Figures 6.8(a-b). The carbon fibers were placed in the x-y plane at a distance of 9 mm from the surface of the linear transducer array. Figures 6.8(c)-(e) show both the fitting curves and PA amplitude distributions along the elevational (x), lateral

(y), and axial (z) directions. The full width at half maximum (FWHM) values, which are also spatial resolutions, are 1237 μm, 119 μm, and 86 μm in the elevational, lateral, and axial directions, respectively.

Phantom experiments were then conducted to show the ability of the linear-array-based PA probe to measure melanoma thickness (depth) and calculate tumor volume (size). As shown in Figure 6.9(a), melanoma phantoms of varying thicknesses and volumes were prepared. All the phantoms were made from a black ink and agar mixture, which had an absorption coefficient of 70 cm^{-1} at 680 nm, close to the actual typical melanoma absorption coefficient. To mimic human tissue, the background was made of an agar and intralipid mixture with a scattering coefficient around 100 cm^{-1} and a scattering anisotropy of ~0.9. To facilitate optimal comparison of melanoma phantoms,

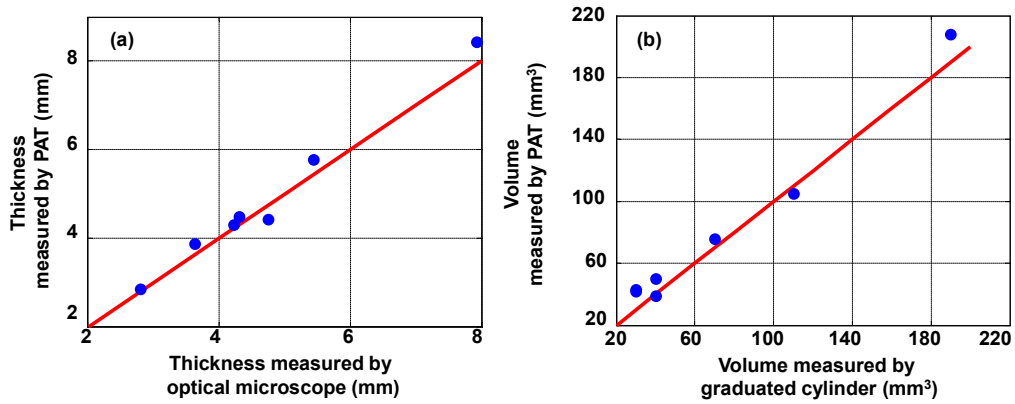

Figure 6.10 Depth (a) and volume (b) quantification of melanoma phantoms. Blue dots: experimental measurements. Red lines: ideal line if the PA measurements are identical to the standard measurements.

we took the maximum-amplitude-projections of the 3D PA images along the elevational direction of the linear array, as shown in Figure 6.9(b1-b7). Immediately following the array-based experiments, melanoma phantoms were carefully removed from the agar/intralipid mixture, and corresponding gross images were taken using a standard microscope (EZ4 Stereo microscope,

Leica), as shown in Figures 6.9(c1-c7). There is an excellent correlation between the PA and gross images, demonstrating the ability of this system to accurately reproduce the phantom *in situ*. To further demonstrate the accuracy of the PA system and thus its potential for *in vivo* imaging, we then calculated both the depth and volume of these melanoma phantoms (Figure 6.10). The thickness and volume of the melanoma phantoms measured by the standard microscope and a graduated cylinder, respectively, served as the gold standards. In the PA measurements, to quantify the depth, the 6 dB threshold was used to separate the melanoma from the background. To quantify the volume, the 3D melanoma images were first downsampled. The downsampled image pixel size was equal to the resolution in each direction. The downsampled images were then thresholded at 6 dB of the noise level to create melanoma boundaries. In the end, the volume was calculated by integrating the voxels inside the melanoma. We show that both the depths and volumes measured by our system agree well with the standard values, indicating that our linear-array-based PA probe can detect both the depth and volume of deeply seated melanoma *in situ* with high accuracy.

We then performed experiments *ex vivo* to determine the accuracy of our system for thickness (depth) measurement, and volume calculation. For these experiments, we used a murine xenograft model where B16 melanoma cells were subcutaneously injected into the dorsal surface of nude mice (Hsd:Athymic Nude-Foxn1NU, Harlan Co.; average body weight: 20 g). All experimental animal procedures were carried out in conformity with the laboratory animal protocol approved by the Animal Studies Committee of Washington University in St. Louis. Tumors were allowed to grow spontaneously for 15 days, and the mice were then sacrificed. Fresh tumors excised from nude mice were embedded in the agar and intralipid mixture, prepared as described earlier (Figure 6.11a). Imaging and processing was then performed as in the phantom experiments. Similarly, the *ex vivo* PA images of the melanomas are representative of the tumors as shown in Figures 6.11(b)

and (c). Again, the thickness and volume values calculated from the images are in accordance with the preset values (shown in Figure 6.12). Thus, we conclude that our system should be able to accurately image deep melanomas *in vivo*.

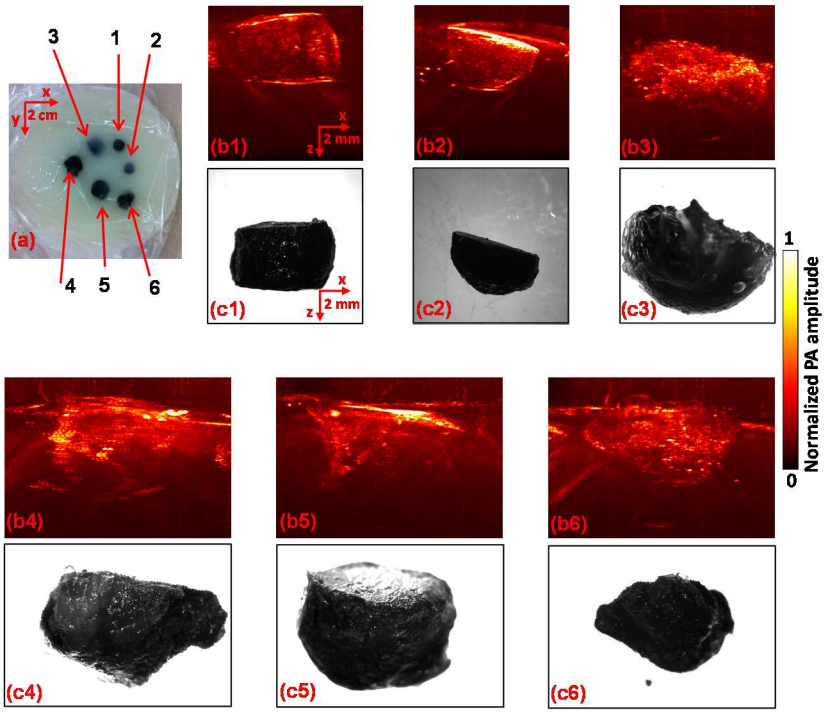

Figure 6.11 Linear-array-based PA images of *ex vivo* melanomas. (a) A photo of the *ex vivo* melanomas. (b1-b6) and (c1-c6) correspond to the melanoma phantoms 1-6 in (a). Melanoma images acquired by PA (b1-b6) and a standard optical microscope (c1-c6).

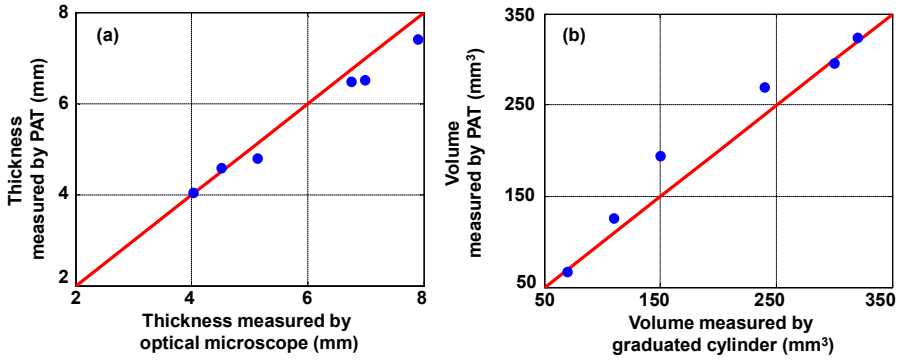

Figure 6.12 Depth (a) and volume (b) quantification of *ex vivo* melanomas. Blue dots: experimental measurements. Red lines: ideal line if the PA measurements are identical to the standard measurements.

Finally, we imaged mice with melanoma *in vivo* to show the detection ability of the linear-array-based PA probe. We again employed the murine xenograft model using B16 melanoma cells in nude mice. For image acquisition, mice were anesthetized and kept motionless using a breathing anesthesia system (E-Z Anesthesia, Euthanex), while body temperature was maintained by an electric heating pad. Each measurement was repeated at day 3 and day 6 following the injection of cells (Figures 6.13a, b), and the rate of growth (ROG) was calculated. Again the detected melanoma can be clearly distinguished from the surrounding soft tissue. The depth and volume of the melanoma at day 3 and day 6 were measured to be 1.32 mm and 22.365 mm^3, and 2.77 mm and 71.931 mm^3, respectively. The depth-based and volume-based ROG were calculated to be 0.48 mm/day and 16.555 mm^3/day, respectively.

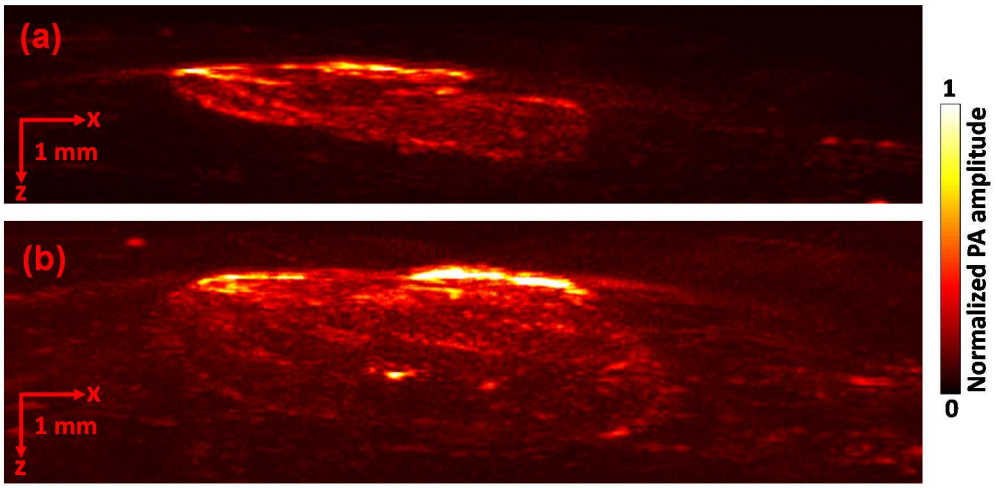

Figure 6.13 Linear-array-based PA images of melanoma acquired *in vivo* on day 3 (a) and day 6 (b).

6.3 Handheld Photoacoustic Probe for Noninvasive Determination of Melanoma Depth in Patients

Method In this section, we applied the linear array probe for melanoma patient imaging. In our study, 10 patients were recruited and a total 13 lesions were imaged. Benefits and risks of our

study were explained to the patients in detail. A written consent was obtained for the procedure. For each patient, we first imaged the melanoma with our PAT probe. Then an excisional biopsy was performed to extract the true melanoma depth. In these 13 lesions, there were 5 cases with a prior incisional biopsy. When analyzing our results, we found that among the 13 lesions, one lesion was not melanoma, and one lesion was very big (>10 mm), which was beyond the maximum imaging depth of this PAT probe for melanoma. Thus, we excluded these two cases in our final data analysis and focused on whether the PAT probe can be used for depth quantification of relatively shadow melanomas (i.e., <10 mm). All methods and experimental procedures were carried out in accordance with the guidelines of The Institutional Review Board of Washington University in St. Louis.

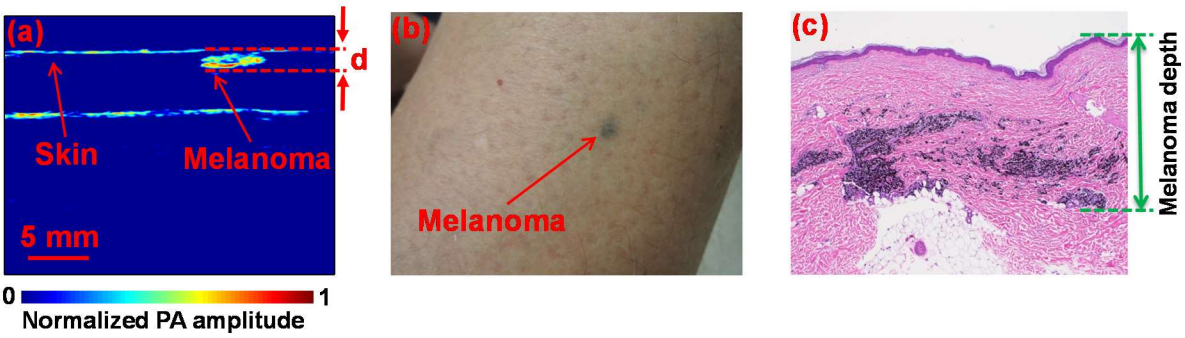

Figure 6.14 PAT of melanoma in patients. (a) Melanoma image acquired with PAT, clearly showing the melanoma and skin surface. (b) Photograph of melanoma in patient. (c) Histologic examination of the melanoma, showing its true depth.

A typical melanoma image acquired by PAT is shown in Figure 6.14(a), where the whole melanoma as well as the skin surface can be clearly seen. Thus, the melanoma depth information can be accurately recovered. In this case, the PAT-measured melanoma depth is 1.9 mm. Figure 6.14(b) shows a photograph of the melanoma in the patient before excision. Immediately after the PAT experiment, an excisional biopsy was performed to determine the true tumor depth, as shown

in Figure 6.14(c). Based on the histology result, the melanoma depth was 1.67 mm. Note that in the process of fixation, the specimen may have shrunk by 30% of its volume, which corresponds to around 12% shrinkage in depth. Taking the shrinkage into account, a melanoma depth *in vivo* (based on PAT) of 1.9 mm actually corresponds to the 1.67 mm depth of melanoma *ex vivo*, which exactly matches the histological measurement. Thus, we demonstrated that PAT can measure melanoma depth noninvasively and accurately in patients.

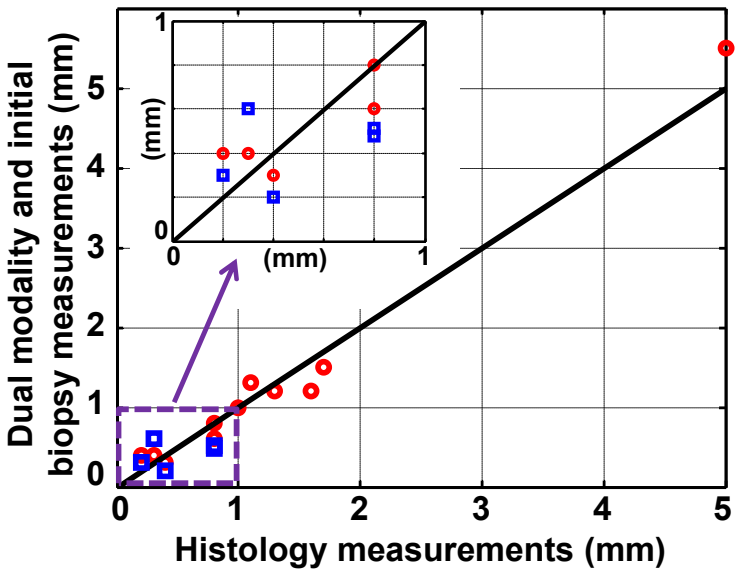

Figure 6.15 PAT-measured depth of all melanomas, showing concordance with the histologic results. In addition, the average PAT-based depth is more accurate than the depth from incisional biopsy. Black line: ideal line if the PAT/incisional measurements are identical to the excisional results. Red circles: PAT measurements. Blue squares: incisional measurements (initial biopsy).

Figure 6.15 shows the results for all 11 melanomas. The maximum and minimum measured melanoma depths are 5 mm and 0.2 mm, respectively. Depth values measured by PAT are in good accord with the excisional biopsy results: For all lesions, the mean absolute error (MAE) was 0.18 mm. We also analyzed the data for melanomas with prior incisional biopsies. In the five patients who underwent diagnostic biopsy prior to PAT followed by wide local excision, PAT yielded more

accurate depths than the initial biopsy. The MAE for the PAT measurements was 0.14 mm, smaller than the MAE of 0.21 mm for the incisional biopsy. Thus, we show that PAT is an effective imaging tool to accurately recover melanoma depth information and guide definitive surgical intervention.

Discussion In this work, melanomas deeper than 10 mm could not be imaged clearly, especially the bottom part. The main reason is the strong light attenuation in the melanoma, leading to very few photons reaching the base of the melanoma and thus very weak signals from the deepest portion. One potential solution would include improving the light illumination efficiency, e.g., allowing light to bypass the center of the tumor.

We recognize that according to our results, PAT did not alter, but rather confirmed, current surgical treatment based upon provisional Breslow depth. However, as shown in our experimental results, PAT yielded greater accuracy than the incisional biopsy in measuring melanoma depth. A larger patient population would be the next step in improving utility of this technology and fine tuning the technique. PAT technology is non-invasive, provides high contrast for deep melanoma imaging, and fit easily in a clinic or surgical suite. Ultimately, PAT technology may be an adjunct to surgical planning for patients with pigmented lesions, allowing more accurate and earlier assessment of melanoma depth to improve treatment of this aggressive and deadly malignancy.

6.4 Conclusions

In this chapter, we first developed a handheld PA probe for melanoma depth measurement in a mouse *in vivo*. With that probe, melanoma as thick as 4.1 mm could be detected, and in the *in vivo* experiment, melanoma with 3.75 mm thickness was imaged. Our measurements also show very high accuracy. To improve the imaging speed, we next applied a handheld linear array probe to

measure both melanoma depth and volume *in vivo*. Compared to the single ultrasonic transducer based system, the linear-array-based system can detect melanoma with an order of magnitude increase in imaging speed. In addition, because of the large acceptance angle of the linear ultrasonic transducer array, nearly the entire melanoma can be detected in 3D, as opposed to only the horizontal boundary. Finally, we applied this array probe for imaging 11 melanomas in patients. As shown in our experimental results, PAT yielded greater accuracy than incisional biopsy in measuring melanoma depth.

Chapter 7 Summary

This dissertation has described the advance of PAT to translational studies and applications. We first improved the resolution and penetration depth of OR-PAM and applied it to count red blood cells and to map bilirubin. We then developed and applied PAT systems to study pain, quantify blood flow, image the brain, and measure melanoma depth in humans.

In chapter 2, we used glycerol as an optical clearing agent in OR-PAM. Our results show that the imaging performance of OR-PAM can be greatly enhanced by optical clearing, both *in vitro* and *in vivo*. We then applied quantitative multi-wavelength PAM to detect bilirubin concentration and distribution simultaneously. By measuring tissue-mimicking phantoms with different bilirubin concentrations, we showed that the root-mean-square error of prediction has was as low as 0.52 and 0.83 mg/dL for pure bilirubin and for blood-mixed bilirubin detection (with 100% oxygen saturation), respectively. We further demonstrated the capability of the PAM system to image bilirubin distribution both with and without blood. Our results show that PAM has potential for noninvasive bilirubin monitoring *in vivo*, as well as for further clinical applications. Finally, we presented a calibration-free method to quantify the absolute particle concentration by statistically analyzing photoacoustic signals. We first derived a theoretical model, then applied it to quantitative measurement of different concentrations of various particles, including red blood cells. Finally, we performed *in vivo* experiments to demonstrate the potential of our method in biological applications. The experimental results agreed well with the predictions from the theoretical model, suggesting that our method can be used for noninvasive measurement of absolute particle concentrations in tissue without fluence calibration.

In chapter 3, we evaluated PAM's use in assisting diagnoses and monitoring the progress and treatment outcome of CRPS. Blood vasculature and sO_2 were imaged by PAM from eight adult patients with CRPS-1. For comparison, patients' hands and cuticles were imaged both before and after stellate ganglion block (SGB). For all patients, both vascular structure and sO_2 could be assessed by PAM. In addition, more vessels and stronger signals were observed after SGB. The results show that PAM can help diagnose and monitor CRPS.

In chapter 4, we developed three flow measurement methods: cross-correlation-based flowmetry, saline-injection-based flowmetry, and cuffing-based flowmetry. Using the cross-correlation-based method, we measured flow velocity without calibration and quantified flow velocities in vessels with different structures in a mouse ear *in vivo*. Using the saline-injection-based method, we successfully measured blood flow velocity in the optical diffusive regime in a mouse tail *in vivo*. Finally, by applying the cuffing-based method, we achieved the first human deep blood flow measurement with PAT.

In chapter 5, we successfully imaged a mouse brain *in vivo*. We first implemented a 5 MHz transducer array for brain imaging and detected representative features in the brain. However, because of the poor resolution of the 5 MHz array system, the image contrast was not high. To solve that problem, we later applied a 21 MHz array system for brain imaging and achieved high contrast brain vasculature images. We then built a 0.5 MHz PACT system for human brain imaging, and achieved good phantom images through a human skull.

In chapter 6, we first developed handheld PAM to detect melanoma and determine tumor depth in nude mice *in vivo*. Compared to our previous PAM system for melanoma imaging, a new light delivery mechanism was introduced to improve light penetration. We showed that melanomas with

4.1 and 3.7 mm thicknesses can be successfully detected in phantom and in *in vivo* experiments, respectively. However, this system was slow. To improve the imaging speed, we applied a linear-array-based photoacoustic probe to detect melanin-containing melanoma tumor depth and volume in nude mice *in vivo*. This system can image melanomas at five frames per second (fps), which is much faster than our previous handheld single transducer system (0.1 fps). We first theoretically showed that, in addition to the higher frame rate, almost the entire boundary of the melanoma can be detected by the linear-array-based probe, while only the horizontal boundary could be detected by the previous system. Then we demonstrated the ability of this linear-array-based system in measuring both the depth and volume of melanoma through phantom, *ex vivo*, and *in vivo* experiments. The volume detection ability also enabled us to accurately calculate the rate of growth of the tumor, which is an important parameter in quantifying its activity. Finally, we applied this array system in imaging melanoma in patients and achieved more accurate melanoma depth information than current incisional biopsy.

References

1. L. V. Wang, S. Hu, Photoacoustic Tomography: In Vivo Imaging from Organelles to Organs. *Science* **335**, 1458 (2012).
2. P. Beard, Biomedical photoacoustic imaging. *Interface Focus* **1**, 602 (2011).
3. L. V. Wang, Prospects of photoacoustic tomography. *Medical Physics* **35**, 5758 (2008).
4. L. V. Wang, Multiscale photoacoustic microscopy and computed tomography. *Nature Photonics* **3**, 503 (2009).
5. L. V. Wang, L. Gao, Photoacoustic microscopy and computed tomography: from bench to bedside. *Annual review of biomedical engineering* **16**, 155 (2014).
6. L. V. Wang, Tutorial on photoacoustic microscopy and computed tomography. *Ieee Journal of Selected Topics in Quantum Electronics* **14**, 171 (2008).
7. J. J. Yao, K. I. Maslov, Y. Zhang, Y. N. Xia, L. V. Wang, Label-free oxygen-metabolic photoacoustic microscopy in vivo. *Journal of Biomedical Optics* **16**, (2011).
8. X. H. Zhu, J. M. Chen, T. W. Tu, W. Chen, S. K. Song, Simultaneous and noninvasive imaging of cerebral oxygen metabolic rate, blood flow and oxygen extraction fraction in stroke mice. *NeuroImage* **64**, 437 (2013).
9. X. D. Wang *et al.*, Noninvasive laser-induced photoacoustic tomography for structural and functional in vivo imaging of the brain. *Nature Biotechnology* **21**, 803 (2003).
10. K. Maslov, H. F. Zhang, S. Hu, L. V. Wang, Optical-resolution photoacoustic microscopy for in vivo imaging of single capillaries. *Optics letters* **33**, 929 (2008).
11. K. Maslov, G. Stoica, L. H. V. Wang, In vivo dark-field reflection-mode photoacoustic microscopy. *Optics letters* **30**, 625 (2005).
12. S. Hu, L. V. Wang, Optical-Resolution Photoacoustic Microscopy: Auscultation of Biological Systems at the Cellular Level. *Biophysical Journal* **105**, 841 (2013).
13. C. Zhang, Y. J. Cheng, J. J. Chen, S. Wickline, L. H. V. Wang, Label-free photoacoustic microscopy of myocardial sheet architecture. *Journal of Biomedical Optics* **17**, (2012).
14. D. K. Yao, R. M. Chen, K. Maslov, Q. F. Zhou, L. V. Wang, Optimal ultraviolet wavelength for in vivo photoacoustic imaging of cell nuclei. *Journal of Biomedical Optics* **17**, (2012).
15. D. K. Yao, K. Maslov, K. K. Shung, Q. F. Zhou, L. V. Wang, In vivo label-free photoacoustic microscopy of cell nuclei by excitation of DNA and RNA. *Optics letters* **35**, 4139 (2010).
16. Z. Xu, Q. I. Zhu, L. H. V. Wang, In vivo photoacoustic tomography of mouse cerebral edema induced by cold injury. *Journal of Biomedical Optics* **16**, (2011).
17. Z. Xu, C. H. Li, L. V. Wang, Photoacoustic tomography of water in phantoms and tissue. *Journal of Biomedical Optics* **15**, (2010).
18. H. W. Wang *et al.*, Label-Free Bond-Selective Imaging by Listening to Vibrationally Excited Molecules. *Physical Review Letters* **106**, (2011).
19. C. Zhang, Y. S. Zhang, D. K. Yao, Y. N. Xia, L. H. V. Wang, Label-free photoacoustic microscopy of cytochromes. *Journal of Biomedical Optics* **18**, (2013).
20. Y. Zhou, C. Zhang, D. K. Yao, L. H. V. Wang, Photoacoustic microscopy of bilirubin in tissue phantoms. *Journal of Biomedical Optics* **17**, (2012).
21. Y. Wang *et al.*, Fiber-laser-based photoacoustic microscopy and melanoma cell detection. *Journal of Biomedical Optics* **16**, (2011).

22. C. Zhang, K. Maslov, L. H. V. Wang, Subwavelength-resolution label-free photoacoustic microscopy of optical absorption in vivo. *Optics letters* **35**, 3195 (2010).
23. A. Danielli *et al.*, Label-free photoacoustic nanoscopy. *Journal of Biomedical Optics* **19**, (2014).
24. S. Hu, K. Maslov, L. V. Wang, Second-generation optical-resolution photoacoustic microscopy with improved sensitivity and speed. *Optics letters* **36**, 1134 (2011).
25. C. P. Favazza, O. Jassim, L. A. Cornelius, L. H. V. Wang, In vivo photoacoustic microscopy of human cutaneous microvasculature and a nevus. *Journal of Biomedical Optics* **16**, (2011).
26. Y. Zhou, J. J. Yao, L. H. V. Wang, Optical clearing-aided photoacoustic microscopy with enhanced resolution and imaging depth. *Optics letters* **38**, 2592 (2013).
27. Y. Zhou, J. Yao, K. I. Maslov, L. V. Wang, Calibration-free absolute quantification of particle concentration by statistical analyses of photoacoustic signals in vivo. *J. Biomed. Opt.* **19**, 37001 (2014).
28. S. L. Chen, Z. X. Xie, P. L. Carson, X. D. Wang, L. J. Guo, In vivo flow speed measurement of capillaries by photoacoustic correlation spectroscopy. *Optics letters* **36**, 4017 (2011).
29. J. Yao, L. V. Wang, Photoacoustic tomography: fundamentals, advances and prospects. *Contrast Media & Molecular Imaging* **6**, 332 (2011).
30. J. J. Yao, K. I. Maslov, Y. F. Shi, L. A. Taber, L. H. V. Wang, In vivo photoacoustic imaging of transverse blood flow by using Doppler broadening of bandwidth. *Optics letters* **35**, 1419 (2010).
31. Y. Zhou, J. Y. Liang, K. I. Maslov, L. H. V. Wang, Calibration-free in vivo transverse blood flowmetry based on cross correlation of slow time profiles from photoacoustic microscopy. *Optics letters* **38**, 3882 (2013).
32. Y. Liu, C. Zhang, L. H. V. Wang, Effects of light scattering on optical-resolution photoacoustic microscopy. *Journal of Biomedical Optics* **17**, (2012).
33. D. Zhu, K. V. Larin, Q. M. Luo, V. V. Tuchin, Recent progress in tissue optical clearing. *Laser & Photonics Reviews* **7**, 732 (2013).
34. M. Kinnunen, R. Myllyla, Effect of glucose on photoacoustic signals at the wavelengths of 1064 and 532 nm in pig blood and intralipid. *Journal of Physics D-Applied Physics* **38**, 2654 (2005).
35. X. Wen, Z. Mao, Z. Han, V. V. Tuchin, D. Zhu, In vivo skin optical clearing by glycerol solutions: mechanism. *Journal of biophotonics* **3**, 44 (2010).
36. G. Vargas, A. Readinger, S. S. Dozier, A. J. Welch, Morphological changes in blood vessels produced by hyperosmotic agents and measured by optical coherence tomography. *Photochemistry and photobiology* **77**, 541 (2003).
37. D. Zhu *et al.*, Short-term and long-term effects of optical clearing agents on blood vessels in chick chorioallantoic membrane. *Journal of biomedical optics* **13**, 021106 (2008).
38. D. Zhu, J. Wang, Z. Zhi, X. Wen, Q. Luo, Imaging dermal blood flow through the intact rat skin with an optical clearing method. *Journal of biomedical optics* **15**, 026008 (2010).
39. J. Wang, R. Shi, D. Zhu, Switchable skin window induced by optical clearing method for dermal blood flow imaging. *Journal of biomedical optics* **18**, 061209 (2013).
40. H. American Academy of Pediatrics Subcommittee on, Management of hyperbilirubinemia in the newborn infant 35 or more weeks of gestation. *Pediatrics* **114**, 297 (2004).
41. S. P. Roche, R. Kobos, Jaundice in the adult patient. *American family physician* **69**, 299 (2004).

42. V. K. Bhutani, L. Johnson, Kernicterus in the 21st century: frequently asked questions. *Journal of perinatology : official journal of the California Perinatal Association* **29 Suppl 1**, S20 (2009).
43. S. N. el-Beshbishi, K. E. Shattuck, A. A. Mohammad, J. R. Petersen, Hyperbilirubinemia and transcutaneous bilirubinometry. *Clinical chemistry* **55**, 1280 (2009).
44. C. E. Ahlfors, Criteria for exchange transfusion in jaundiced newborns. *Pediatrics* **93**, 488 (1994).
45. S. Kosarat, V. Khuwuthyakorn, Accuracy of transcutaneous bilirubin measurement in term newborns. *Journal of the Medical Association of Thailand = Chotmaihet thangphaet* **96**, 172 (2013).
46. F. F. Rubaltelli *et al.*, Transcutaneous bilirubin measurement: a multicenter evaluation of a new device. *Pediatrics* **107**, 1264 (2001).
47. L. L. Randeberg, E. L. Larsen, L. O. Svaasand, Characterization of vascular structures and skin bruises using hyperspectral imaging, image analysis and diffusion theory. *Journal of biophotonics* **3**, 53 (2010).
48. Y. Yamauchi, I. Yamanouchi, Transcutaneous bilirubinometry: bilirubin kinetics of the skin and serum during and after phototherapy. *Biology of the neonate* **56**, 263 (1989).
49. G. Agati, F. Fusi, G. P. Donzelli, R. Pratesi, Quantum yield and skin filtering effects on the formation rate of lumirubin. *Journal of photochemistry and photobiology. B, Biology* **18**, 197 (1993).
50. S. K. Alla *et al.*, Point-of-care device for quantification of bilirubin in skin tissue. *IEEE transactions on bio-medical engineering* **58**, 777 (2011).
51. M. J. Maisels *et al.*, Evaluation of a new transcutaneous bilirubinometer. *Pediatrics* **113**, 1628 (2004).
52. G. Bertini, S. Pratesi, E. Cosenza, C. Dani, Transcutaneous bilirubin measurement: evaluation of Bilitest. *Neonatology* **93**, 101 (2008).
53. G. Payne, N. Langlois, C. Lennard, C. Roux, Applying visible hyperspectral (chemical) imaging to estimate the age of bruises. *Medicine, science, and the law* **47**, 225 (2007).
54. L. D. Wang, K. Maslov, J. J. Yao, B. Rao, L. H. V. Wang, Fast voice-coil scanning optical-resolution photoacoustic microscopy. *Optics letters* **36**, 139 (2011).
55. B. Rao *et al.*, Real-time four-dimensional optical-resolution photoacoustic microscopy with Au nanoparticle-assisted subdiffraction-limit resolution. *Optics letters* **36**, 1137 (2011).
56. C. Zhang *et al.*, Reflection-mode submicron-resolution in vivo photoacoustic microscopy. *Journal of Biomedical Optics* **17**, (2012).
57. C. J. Mullon, R. Langer, Determination of conjugated and total bilirubin in serum of neonates, with use of bilirubin oxidase. *Clinical chemistry* **33**, 1822 (1987).
58. J. R. Rajian, P. L. Carson, X. Wang, Quantitative photoacoustic measurement of tissue optical absorption spectrum aided by an optical contrast agent. *Optics express* **17**, 4879 (2009).
59. J. Laufer, D. Delpy, C. Elwell, P. Beard, Quantitative spatially resolved measurement of tissue chromophore concentrations using photoacoustic spectroscopy: application to the measurement of blood oxygenation and haemoglobin concentration. *Physics in medicine and biology* **52**, 141 (2007).
60. Z. Yuan, H. B. Jiang, Quantitative photoacoustic tomography. *Philosophical Transactions of the Royal Society a-Mathematical Physical and Engineering Sciences* **367**, 3043 (2009).

61. H. Gao, S. Osher, H. K. Zhao, Quantitative Photoacoustic Tomography. *Mathematical Modeling in Biomedical Imaging Ii: Optical, Ultrasound, and Opto-Acoustic Tomographies* **2035**, 131 (2012).
62. B. Cox, J. G. Laufer, S. R. Arridge, P. Beard, Quantitative spectroscopic photoacoustic imaging: a review. *Journal of Biomedical Optics* **17**, (2012).
63. A. Q. Bauer, R. E. Nothdurft, T. N. Erpelding, L. H. V. Wang, J. P. Culver, Quantitative photoacoustic imaging: correcting for heterogeneous light fluence distributions using diffuse optical tomography. *Journal of Biomedical Optics* **16**, (2011).
64. P. D. Kumavor *et al.*, Target detection and quantification using a hybrid hand-held diffuse optical tomography and photoacoustic tomography system. *Journal of Biomedical Optics* **16**, (2011).
65. R. O. Esenaliev *et al.*, Optoacoustic technique for noninvasive monitoring of blood oxygenation: a feasibility study. *Applied Optics* **41**, 4722 (2002).
66. J. Laufer, C. Elwell, D. Delpy, P. Beard, In vitro measurements of absolute blood oxygen saturation using pulsed near-infrared photoacoustic spectroscopy: accuracy and resolution. *Physics in medicine and biology* **50**, 4409 (2005).
67. Y. Y. Petrov, I. Y. Petrova, I. A. Patrikeev, R. O. Esenaliev, D. S. Prough, Multiwavelength optoacoustic system for noninvasive monitoring of cerebral venous oxygenation: a pilot clinical test in the internal jugular vein. *Optics letters* **31**, 1827 (2006).
68. Y. Wang, R. K. Wang, Photoacoustic recovery of an absolute optical absorption coefficient with an exact solution of a wave equation. *Physics in medicine and biology* **53**, 6167 (2008).
69. Z. J. Guo, S. Hu, L. H. V. Wang, Calibration-free absolute quantification of optical absorption coefficients using acoustic spectra in 3D photoacoustic microscopy of biological tissue. *Optics letters* **35**, 2067 (2010).
70. Z. J. Guo, C. Favazza, A. Garcia-Uribe, L. H. V. Wang, Quantitative photoacoustic microscopy of optical absorption coefficients from acoustic spectra in the optical diffusive regime. *Journal of Biomedical Optics* **17**, (2012).
71. Y. Wang, R. K. Wang, Measurement of particle concentration in flow by statistical analyses of optical coherence tomography signals. *Optics letters* **36**, 2143 (2011).
72. H. Baatz, M. Steinbauer, A. G. Harris, F. Krombach, Kinetics of white blood cell staining by intravascular administration of rhodamine 6G. *International journal of microcirculation, clinical and experimental / sponsored by the European Society for Microcirculation* **15**, 85 (1995).
73. S. Bruehl, An update on the pathophysiology of complex regional pain syndrome. *Anesthesiology* **113**, 713 (2010).
74. D. Mrabet *et al.*, [Pathophysiology of complex regional pain syndrome (CRPS) type 1]. *La Tunisie medicale* **90**, 278 (2012).
75. R. J. Schwartzman, G. M. Alexander, J. Grothusen, Pathophysiology of complex regional pain syndrome. *Expert review of neurotherapeutics* **6**, 669 (2006).
76. L. Parkitny *et al.*, Inflammation in complex regional pain syndrome A systematic review and meta-analysis. *Neurology* **80**, 106 (2013).
77. F. van Eijs *et al.*, Predictors of Pain Relieving Response to Sympathetic Blockade in Complex Regional Pain Syndrome Type 1. *Anesthesiology* **116**, 113 (2012).
78. M. Schurmann, J. Zaspel, G. Gradl, A. Wipfel, F. Christ, Assessment of the peripheral microcirculation using computer-assisted venous congestion plethysmography in post-

traumatic complex regional pain syndrome type I. *Journal of Vascular Research* **38**, 453 (2001).
79. M. Dirckx, D. L. Stronks, G. Groeneweg, F. J. P. M. Huygen, Effect of Immunomodulating Medications in Complex Regional Pain Syndrome A Systematic Review. *Clinical Journal of Pain* **28**, 355 (2012).
80. X. Moisset, D. Bouhassira, Brain imaging of neuropathic pain. *NeuroImage* **37 Suppl 1**, S80 (2007).
81. D. G. Owen, Y. Bureau, A. W. Thomas, F. S. Prato, K. S. St Lawrence, Quantification of pain-induced changes in cerebral blood flow by perfusion MRI. *Pain* **136**, 85 (2008).
82. A. Lebel *et al.*, fMRI reveals distinct CNS processing during symptomatic and recovered complex regional pain syndrome in children. *Brain : a journal of neurology* **131**, 1854 (2008).
83. R. C. Coghill, C. N. Sang, K. F. Berman, G. J. Bennett, M. J. Iadarola, Global cerebral blood flow decreases during pain. *Journal of cerebral blood flow and metabolism : official journal of the International Society of Cerebral Blood Flow and Metabolism* **18**, 141 (1998).
84. T. Okano *et al.*, Use of near-infrared spectroscopy to evaluate stellate ganglion block. *Regional Anesthesia and Pain Medicine* **26**, 186 (2001).
85. M. Koban, S. Leis, S. Schultze-Mosgau, F. Birklein, Tissue hypoxia in complex regional pain syndrome. *Pain* **104**, 149 (2003).
86. Y. H. Zhao *et al.*, Phase-resolved optical coherence tomography and optical Doppler tomography for imaging blood flow in human skin with fast scanning speed and high velocity sensitivity. *Optics letters* **25**, 114 (2000).
87. W. E. Ackerman, M. A. Munir, J.-M. Zhang, Assessment of Laser Doppler Imaging for the Diagnosis of Complex Regional Pain Syndrome I. *Journal of Neuropathic Pain & Symptom Palliation* **1**, 13 (2005).
88. Y. Zhou *et al.*, Microcirculatory changes identified by photoacoustic microscopy in patients with complex regional pain syndrome type I after stellate ganglion blocks. *Journal of Biomedical Optics* **19**, (2014).
89. R. N. Harden *et al.*, Validation of proposed diagnostic criteria (the "Budapest Criteria") for Complex Regional Pain Syndrome. *Pain* **150**, 268 (2010).
90. D. R. Bickerstaff, J. A. Kanis, Algodystrophy: an under-recognized complication of minor trauma. *Br J Rheumatol* **33**, 240 (1994).
91. Y. Zhou, J. Liang, L. V. Wang, Cuffing-based photoacoustic flowmetry in humans in the optical diffusive regime. *J Biophotonics* (2015).
92. Y. Zhou, J. Poudel, G. Li, L. V. Wang, In vivo photoacoustic flowmetry at depths of the diffusive regime based on saline injection. *J Biomed Opt* **20**, 87001 (2015).
93. J. Y. Liang, Y. Zhou, K. I. Maslov, L. H. V. Wang, Cross-correlation-based transverse flow measurements using optical resolution photoacoustic microscopy with a digital micromirror device. *Journal of Biomedical Optics* **18**, (2013).
94. A. Al-Khaldi, H. Al-Sabti, J. Galipeau, K. Lachapelle, Therapeutic angiogenesis using autologous bone marrow stromal cells: Improved blood flow in a chronic limb ischemia model. *Ann Thorac Surg* **75**, 204 (2003).
95. B. Fagrell, M. Intaglietta, Microcirculation: Its significance in clinical and molecular medicine. *J Intern Med* **241**, 349 (1997).

96. Z. Y. Shen *et al.*, Transverse flow velocity quantification using optical coherence tomography with correlation. *Laser Phys Lett* **8**, 318 (2011).
97. R. B. Thompson, E. R. McVeigh, Real-time volumetric flow measurements with complex-difference MRI. *Magnet Reson Med* **50**, 1248 (2003).
98. Y. Wang, R. K. Wang, Autocorrelation optical coherence tomography for mapping transverse particle-flow velocity. *Optics letters* **35**, 3538 (2010).
99. A. Y. Shih *et al.*, Two-photon microscopy as a tool to study blood flow and neurovascular coupling in the rodent brain. *J Cerebr Blood F Met* **32**, 1277 (2012).
100. M. J. Yoon *et al.*, Pulpal Blood Flow Measurement with Ultrasound Doppler Imaging. *J Endodont* **36**, 419 (2010).
101. H. Fang, K. Maslov, L. V. Wang, Photoacoustic Doppler flow measurement in optically scattering media. *Applied Physics Letters* **91**, (2007).
102. H. Fang, K. Maslov, L. V. Wang, Photoacoustic doppler effect from flowing small light-absorbing particles. *Physical Review Letters* **99**, (2007).
103. S. L. Chen, T. Ling, S. W. Huang, H. W. Baac, L. J. Guo, Photoacoustic correlation spectroscopy and its application to low-speed flow measurement. *Optics letters* **35**, 1200 (2010).
104. J. J. Yao, L. H. V. Wang, Transverse flow imaging based on photoacoustic Doppler bandwidth broadening. *Journal of Biomedical Optics* **15**, (2010).
105. J. Brunker, P. Beard, Pulsed photoacoustic Doppler flowmetry using time-domain cross-correlation: Accuracy, resolution and scalability. *Journal of the Acoustical Society of America* **132**, 1780 (2012).
106. Z. J. Guo, Z. Xu, L. H. V. Wang, Dependence of photoacoustic speckles on boundary roughness. *Journal of Biomedical Optics* **17**, (2012).
107. L. D. Wang, J. Xia, J. J. Yao, K. I. Maslov, L. H. V. Wang, Ultrasonically Encoded Photoacoustic Flowgraphy in Biological Tissue. *Phys. Rev. Lett.* **111**, (2013).
108. Y. Zhou, W. X. Xing, K. I. Maslov, L. A. Cornelius, L. H. V. Wang, Handheld photoacoustic microscopy to detect melanoma depth in vivo. *Optics letters* **39**, 4731 (2014).
109. Y. Zhou *et al.*, Handheld photoacoustic probe to detect both melanoma depth and volume at high speed in vivo. *J. Biophotonics* **1**, (2015).
110. A. F. Jerant, J. T. Johnson, C. D. Sheridan, T. J. Caffrey, Early detection and treatment of skin cancer. *Am Fam Physician* **62**, 357 (2000).
111. E. M. Dunki-Jacobs, G. G. Callendar, K. M. McMasters, Current management of melanoma. *Current Problems in Surgery* **50**, 351 (2013).
112. L. Smith, S. MacNeil, State of the art in non-invasive imaging of cutaneous melanoma. *Skin Research and Technology* **17**, 257 (2011).
113. P. Guitera, S. W. Menzies, State of the art of diagnostic technology for early-stage melanoma. *Expert Review of Anticancer Therapy* **11**, 715 (2011).
114. I. H. Wolf, J. Smolle, H. P. Soyer, H. Kerl, Sensitivity in the clinical diagnosis of malignant melanoma. *Melanoma Research* **8**, 425 (1998).
115. C. Benvenuto-Andrade *et al.*, Differences between polarized light dermoscopy and immersion contact dermoscopy for the evaluation of skin lesions. *Archives of Dermatology* **143**, 329 (2007).
116. A. C. Halpern, Total body skin imaging as an aid to melanoma detection. *Seminars in Cutaneous Medicine and Surgery* **22**, 2 (2003).

117. T. Gambichler *et al.*, Characterization of benign and malignant melanocytic skin lesions using optical coherence tomography in vivo. *Journal of the American Academy of Dermatology* **57**, 629 (2007).
118. S. Segura, S. Puig, C. Carrera, J. Palou, J. Malvehy, Development of a two-step method for the diagnosis of melanoma by reflectance confocal microscopy. *Journal of the American Academy of Dermatology* **61**, 216 (2009).
119. E. Dimitrow *et al.*, Sensitivity and Specificity of Multiphoton Laser Tomography for In Vivo and Ex Vivo Diagnosis of Malignant Melanoma. *Journal of Investigative Dermatology* **129**, 1752 (2009).
120. W. Dummer *et al.*, Preoperative Characterization of Pigmented Skin-Lesions by Epiluminescence Microscopy and High-Frequency Ultrasound. *Archives of Dermatology* **131**, 279 (1995).
121. J. Bittoun, B. Querleux, L. Darrasse, Advances in MR imaging of the skin. *Nmr in Biomedicine* **19**, 723 (2006).
122. T. Z. Belhocine, A. M. Scott, E. Even-Sapir, J. L. Urbain, R. Essner, Role of nuclear medicine in the management of cutaneous malignant melanoma. *Journal of Nuclear Medicine* **47**, 957 (2006).
123. J. T. Oh *et al.*, Three-dimensional imaging of skin melanoma in vivo by dual-wavelength photoacoustic microscopy. *Journal of Biomedical Optics* **11**, (2006).

Vita

Yong Zhou

Degrees

Ph.D., Biomedical Engineering
Washington University in St. Louis
May 2016

M.S., Physics
Tsinghua University
June 2011

B.S., Electronic Engineering
Tsinghua University
June 2007

Pubications

1. **Y. Zhou**, J. Yao, and L. V. Wang, "Tutorial on photoacoustic tomography," J. Biomed. Opt. (accepted). (Invited review article)
2. C. Yeh, J. Liang, **Y. Zhou**, S. Hu, R. E. Sohn, J. M. Arbeit, and L. V. Wang, "Photoacoustic microscopy of arteriovenous shunts and blood diffusion in early stage tumors," J. Biomed. Opt. 21(2), 020501 (2016).
3. P. Hai†, **Y. Zhou**†, J. Liang, C. Li, and L. V. Wang, "Photoacoustic tomography of vascular compliance in humans," J. Biomed. Opt. 20(12), 126008 (2015).
(† denotes equal contribution.)
4. **Y. Zhou**, J. Liang, and L. V. Wang, "Cuffing-based photoacoustic flowmetry in humans in the optical diffusive regime," J. Biophotonics 1-5 (2015), DOI 10.1002.
5. **Y. Zhou**, J. Poudel, G. Li, and L. V. Wang, "In vivo photoacoustic flowmetry at depths of the diffusive regime based on saline injection," J. Biomed. Opt. 20(8), 087001 (2015).

6. M. Tang†, **Y. Zhou**†, R. Zhang, and L. V. Wang, "Noninvasive photoacoustic microscopy of methemoglobin in vivo," J. Biomed. Opt. 20(3), 036007 (2015).

7. **Y. Zhou** and L. V. Wang, "Translational photoacoustic microscopy," in Frontiers in Biophotonics for Translational Medicine, Springer, (2015).

8. **Y. Zhou** and L. V. Wang, "Photoacoustics in Diagnosis of Melanoma and Melanoma Metastasis," in Imaging and Dermatology, Elsevier, (2015).

9. **Y. Zhou**†, G. Li†, L. Zhu, C. Li, L. A. Cornelius, and L. V. Wang, "Handheld photoacoustic probe to detect both melanoma depth and volume at high speed in vivo," J. Biophotonics 8(11-12), 961-967 (2015).

10. S. N. Hennen, W. Xing, Y. Shui, **Y. Zhou**, J. Kalishman, L. B. Andrews-Kaminsky, M. A. Kass, D. C. Beebe, K. I. Maslov, and L. V. Wang, "Photoacoustic tomography imaging and estimation of oxygen saturation of hemoglobin in ocular tissue of rabbits," Experimental Eye Research., 1-6 (2015).

11. P. Hai, J. Yao, K. I. Maslov, **Y. Zhou**, and L. V. Wang, "Near-infrared Optical-resolution Photoacoustic Microscopy," Opt. Lett. 39 (17), 5192-5195 (2014).

12. **Y. Zhou**, X. Yi, W. Xing, S. Hu , K. I. Maslov, and L. V. Wang, "Microcirculatory changes identified by photoacoustic microscopy in patients with complex regional pain syndrome type I (CRPS-1) after stellate ganglion blocks," J. Biomed. Opt. 19(8), 086017 (2014).

13. **Y. Zhou**, W. Xing, K. I. Maslov, L. A. Cornelius, and L. V. Wang, "Handheld photoacoustic microscopy to detect melanoma depth in vivo, " Opt. Lett. 39(16), 4731-4734 (2014).

14. **Y. Zhou**†, J. Yao†, K. I. Maslov, and L. V. Wang, "Calibration-free absolute quantification of particle concentration by statistical analyses of photoacoustic signals in vivo," J. Biomed. Opt. 19(3), 037001 (2014).

15. **Y. Zhou**†, J. Liang†, K. I. Maslov, and L. V. Wang, "Calibration-free transverse blood flow measurement based on time-domain cross correlation using photoacoustic microscopy in vivo," Opt. Lett. 38(19), 3882-3885 (2013).

16. J. Liang†, **Y. Zhou**†, K. I. Maslov, and L. V. Wang, "Cross-correlation-based transverse flow measurements using optical-resolution photoacoustic microscopy with a digital micromirror device," J. Biomed. Opt. 18(9), 096004 (2013).

17. J. Yao, H. Ke, S. Tai, **Y. Zhou**, and L. V. Wang, "Absolute photoacoustic thermometry in deep tissue," Opt. Lett. 38 (24), 5228-5231 (2013).

18. **Y. Zhou**†, J. Yao†, and L. V. Wang, "Optical clearing-aided photoacoustic microscopy with enhanced resolution and imaging depth," Opt. Lett. 38(14), 2592-2595 (2013).

19. J. Liang, **Y. Zhou**, A. W. Winkler, L. Wang, K. I. Maslov, C. Li, and L. V. Wang, "Random-access optical-resolution photoacoustic microscopy using a digital micromirror device," Opt. Lett. 38(15), 2683-2686 (2013).

20. C. Zhang†, **Y. Zhou**†, C. Li, and L. V. Wang, "Slow-sound photoacoustic microscopy,"Appl. Phys. Lett. 102(16), 163702 (2013).

21. **Y. Zhou**†, C. Zhang†, D. Yao and L. V. Wang, "Photoacoustic microscopy of bilirubin in tissue phantoms," J. Biomed. Opt. 17(12), 126019 (2012).

22. **Y. Zhou**, N. Zeng, Y. Ji, Y. Li, X. Dai, P. Li, L. Duan, H. Ma, and Y. He, "Iris as a reflector for differential absorption low-coherence interferometry to measure glucose level in anterior chamber", J. Biomed. Opt. 16, 015004 (2011).

23. **Y. Zhou**, Y. Hu, N. Zeng, Y. Ji, X. Dai, P. Li, H. Ma, and Y. He, "Noninvasive monitoring of Pirenoxine Sodium concentration in aqueous humor based on dual-wavelength iris imaging technique", Biomed. Opt. Express 2, 231-242 (2011).

24. B. Hu, N. Zeng, Z. Liu, Y. Ji, W. Xie, Q. Peng, **Y. Zhou**, Y. He, H. Ma, “Two-dimensional singlet oxygen imaging with its near-infrared luminescence during photosensitization”, J. Biomed. Opt. 16, 022101 (2011).